LOW-DIMENSIONAL MATERIALS FOR OPTOELECTRONIC AND BIOELECTRONIC APPLICATIONS

By

TU HONG

Dissertation
Submitted to the Faculty of the
Graduate School of Vanderbilt University
in partial fulfillment of the requirements
for the degree of

DOCTOR OF PHILOSOPHY
in

Electrical Engineering
August 11, 2017
Nashville, Tennessee

Approved:

Yaqiong Xu, Ph.D.
Daniel M. Fleetwood, Ph.D.
Deyu Li, Ph.D.
Ronald D. Schrimpf, Ph.D.
Sharon M. Weiss, Ph.D.

To my beloved mom and dad

ACKNOWLEDGEMENTS

First and foremost, I would like to take this opportunity to thank my advisor, Dr. Yaqiong Xu. Her skills in technical writing, critical thinking and creativity always motivate me to improve myself. I am extremely impressed by her insights when we try to understand the experimental results and constantly inspired by her brilliant ideas. She is also very concerned about leading the research group toward the right direction and the career development of the group members. I couldn't have completed my Ph.D. without her. Further, I would like to thank my Ph.D. dissertation committee: Dr. Daniel Fleetwood, Dr. Deyu Li, Dr. Ronald Schrimpf, and Dr. Sharon Weiss for taking time to advise me on improving my dissertation and for their helpful suggestions on my research and career path.

I owe a great debt of gratitude to all the group members of Xu Lab, past and present, who contributed to my experimental work and engaged in helpful scientific discussions. I specifically would like to thank Dr. Yunhao Cao, who was the first graduate student in Xu Lab and introduced me to the world of nanotechnology and scientific research, Dr. Honglian Guo, who taught me the fundamentals of optoelectronics and bioelectronics, Binbin Zhang, who helped me went through the transition period from a college student to a graduate researcher, Rui Wang, who provided me with insights and encouragement when I was seeking employment, Tianjiao Wang, who collaborated with me on several research projects, Roel Flores, Zeynab Jarrahi, Yuchen Zhang, Xuyi Luo, Thayer Walmsley, Nathan Fisher, and Tracy Smith, whose friendship I enjoyed very much. Further I would like to thank Da Ying and Xuanyang Ge, both Vanderbilt undergraduate students and assisted me with my research.

I would also like to thank my collaborators. I owe special thanks to Dr. Zhixian Zhou, Bhim Chamlagain, and Hsun-Jen Chuang from Wayne state University. We collaborated

on several two-dimensional materials related research projects and their device fabrication techniques deeply impressed me. Also, I am thankful for Dr. Sharon Weiss and Shuren Hu, who worked with me and other members of my group on the integration of silicon waveguide with 2D materials. Dr. Qi Zhang, Kristina Kitko, Dr. Donna Webb, and Dr. Mingjian Shi helped me on the biological related research. I also would like to thank Dr. Deyu Li, Dr. Yang Yang, Dr. Qian Zhang, and Lin Yang for sharing their wire-bonding machine.

In addition, I would like to express my gratitude to the staff members of Vanderbilt Institute of Nanoscale Science and Engineering (VINSE): Dr. Bo Choi, Dr. Ben Schmidt, Dr. Dmitry Koktysh, and Dr. Anthony Hmelo for supporting my use of VINSE facilities. Also, I would like to thank the staff members of the Center for Nanophase Materials Sciences (CNMS) at Oak Ridge National Laboratory as well as at the Cornell NanoScale Science & Technology Facility, who helped me with my fabrication techniques. I especially would like to thank Dr. Ivan Kravchenko, who was my host staff at CNMS and taught me many fabrication skills.

Finally, special thanks to my family and friends. Mom and dad are always supportive of my decisions and always encourage me to pursue my dreams. I cannot be who I am without them. My roommates during graduate school at different times: Shen Hui, Wei Li, Lin Yang, and Xin Zhang. They were very supportive of my graduate studies and kept me company in difficult times. Mengya Li, I value the time she spent with me and her effort to make me a better person. I wish her the best in her future endeavor. Also, I thank my many other friends at Vanderbilt, from college, and met in other occasions who offered great suggestions on my life and career. I am very grateful for that.

TABLE OF CONTENTS

Page

LIST OF TABLES

Page

LIST OF FIGURES

Page

LIST OF PUBLICATIONS

Portions of this dissertation have been drawn from the following publications and manuscripts:

1. **Tu Hong**, Roman Lazarenko, Daniel C. Colvin, Roel L. Flores, Qi Zhang, and Ya-Qiong Xu, "The Effect of Competitive Surface Functionalization on Dual-Modality Fluorescence and Magnetic Resonance Imaging of Single-Walled Carbon Nanotubes," ***The Journal of Physical Chemistry C*** 116, 16319 (2012).

2. Zeynab Jarrahi†, Yunhao Cao†, **Tu Hong**†, Yevgeniy S. Puzyrev, Bin Wang, Junhao Lin, Alex H. Huffstutter, Sokrates T. Pantelides, and Ya-Qiong Xu. "Enhanced Photoresponse in Curled Graphene Ribbons," ***Nanoscale*** 5, 12206 (2013). † Equal contribution

3. **Tu Hong**, Yunhao Cao, Da Ying, and Ya-Qiong Xu, "Thermal and Optical Properties of Freestanding Flat and Stacked Single-Layer Graphene in Aqueous Media," ***Applied Physics Letters*** 104, 223102 (2014).

4. **Tu Hong**, Bhim Chamlagain, Wenzhi Lin, Hsun-Jen Chuang, Minghu Pan, Zhixian Zhou, and Ya-Qiong Xu, "Polarized Photocurrent Response in Black Phosphorus Field-Effect Transistors," ***Nanoscale*** 6, 8978 (2014).

5. **Tu Hong**, Bhim Chamlagain, Shuren Hu, Sharon M. Weiss, Zhixian Zhou, and Ya-Qiong Xu, "Plasmonic Hot Electron Induced Photocurrent Response at MoS_2-Metal Junction," ***ACS Nano*** 9, 5357 (2015).

6. **Tu Hong**, Bhim Chamlagain, Tianjiao Wang, Hsun-Jen Chuang, Zhixian Zhou, and Ya-Qiong Xu, "Anisotropic Photocurrent Response at Black Phosphorous-MoS_2 p-n Heterojunctions," ***Nanoscale*** 7, 18537 (2015).

7. Kristina E. Kitko†, **Tu Hong**†, Roman M. Lazarenko†, Da Ying, Ya-Qiong Xu, Qi Zhang, "Membrane cholesterol mediates the cellular effects of monolayer graphene substrates," submitted. †Equal contribution

8. **Tu Hong**, Tianjiao Wang, and Ya-Qiong Xu, "Direct measurement of π coupling at the single molecule level using a carbon nanotube force sensor," submitted.

Chapter 1 Introduction to low-dimensional materials

1.1 Background

The field of nanotechnology has witnessed amazing development in the past decade. In particular, studies of carbon nanotubes (CNTs), graphene, and other two-dimensional (2D) materials have evolved into a vast field with more than ten thousand papers published every year.[1] The research focus has shifted from simply exploring the properties of materials themselves to applying them in practical applications.[2] However, the fundamental understanding of such materials is still far from exhausted.

Carbon-based nanomaterials play a major role in low-dimensional materials. Unlike many other bulk materials, carbon atoms can be very versatile in their arrangement. As shown in Figure 1.1, graphene, a 2D material, can be considered as the building block of other carbon allotropes. It can be wrapped into 0D buckyballs, rolled into 1D CNTs, or stacked into 3D graphite. In recent years, research on emerging 2D materials beyond graphene has developed into a thriving field. These 2D materials share some structural similarities with graphene, but possess unique electronic and optoelectronic properties that may enable them to become potential building blocks for the Si dominated semiconductor industry. In this chapter, we start by introducing CNTs, a 1D material, followed by graphene, a 2D material. The basic structure and properties of 2D materials beyond graphene will also be discussed.

1.1.1 Carbon nanotubes (CNTs)

A CNT is a honeycomb lattice rolled into a cylinder, which possesses outstanding

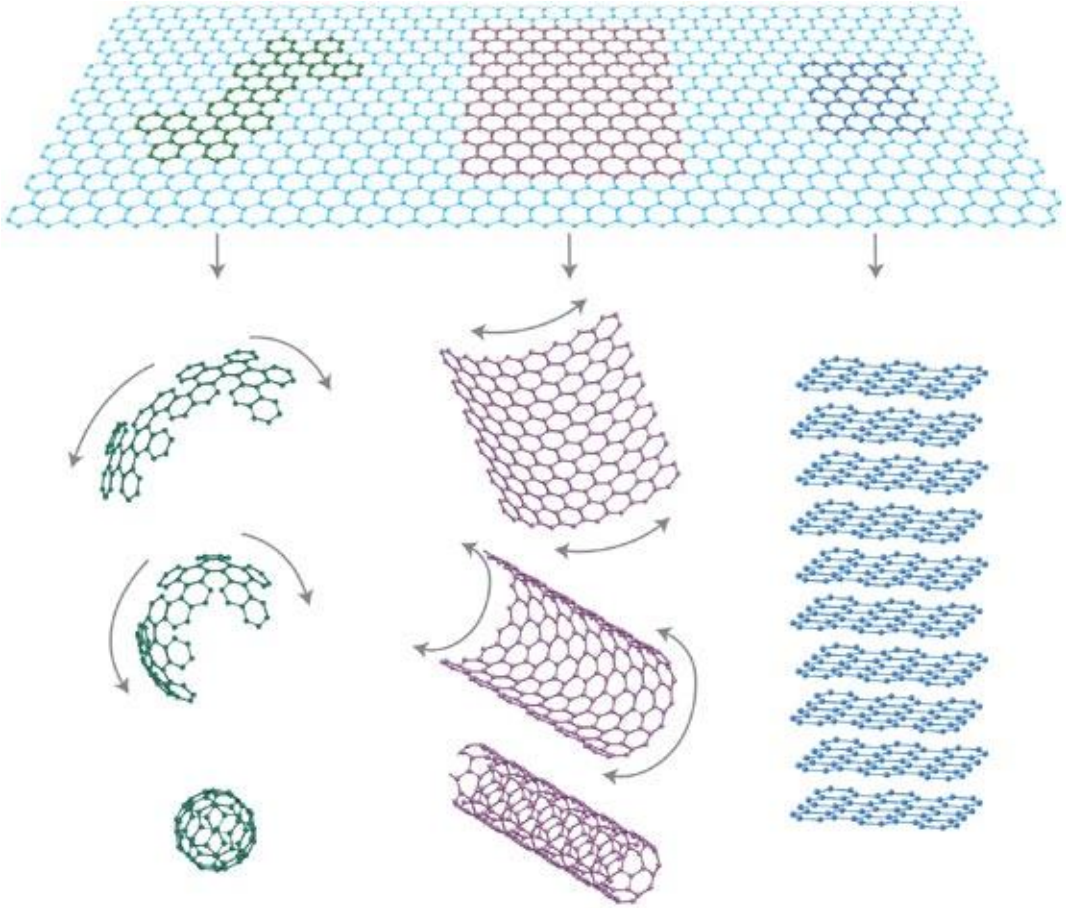

Figure 1.1 Mother of all graphitic forms. Graphene is a 2D building material for carbon materials of all other dimensionalities. It can be wrapped up into 0D buckyballs, rolled into 1D nanotubes, or stacked into 3D graphite. Image reproduced from ref. [3] with permission from Nature Publication Group.

electrical and thermal conductivities and enormous tensile strength.[4, 5] Depending on its orientation, nanotubes can either behave as semiconductors or metals.[4, 5] Semiconducting nanotubes are direct bandgap materials that can be used to both generate and detect light. In fact, it is possible to create a CNT device that can operate either as a transistor, a light emitter or a light detector simply by changing the applied voltage.[6]

The band structure and density of states of a (19, 0) semiconducting CNT is shown in Figure 1.2a and b, respectively. Photoexcitation produces high-energy E_{22} excitons that have

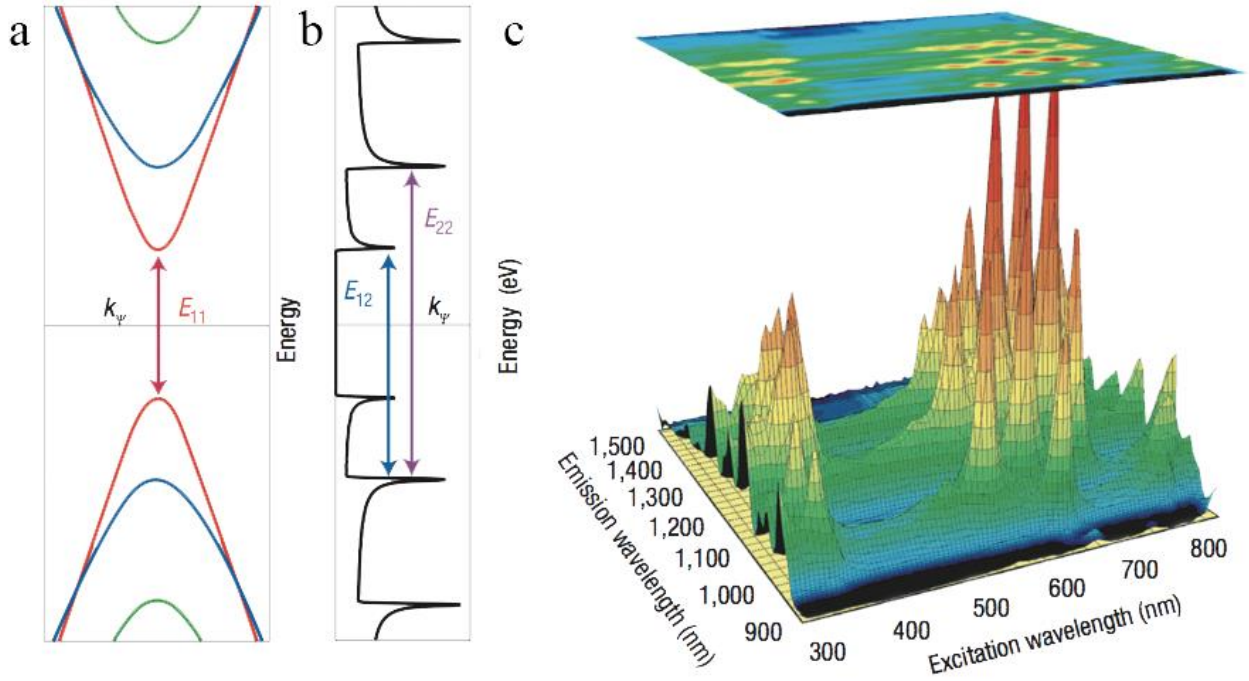

Figure 1.2 Spectroscopy of CNT excitons. a. Valence (bottom) and conduction (top) bands for a (19, 0) semiconducting CNT. red: $k = \pm k_{min}$; blue: $k = \pm 2\ k_{min}$; green: $k = \pm 4\ k_{min}$. k_ψ is the wave vector along the CNT axis. b. Single-particle density of states. c. Three-dimensional plot of exciton photoluminescence from a mixture of surfactant-coated CNTs. Image reproduced from ref. [6] with permission from Nature Publication Group.

zero momentum, and can relax by means of phonons to lower-energy E_{11} states for which the momentum is finite.[6, 7] Recombination of the electron and hole in response to incident light gives rise to photoluminescence (Figure 1.2c).[8] Photoluminescence generation in CNTs has enabled them to become contrast agents for imaging purposed.

1.1.2 Graphene

Graphene is composed of a single layer of carbon atoms arranged in a 2D honeycomb lattice. Electrons propagating through the 2D structure of graphene have a linear relation between energy and momentum, and thus behave as massless Dirac fermions.[3, 9, 10] Therefore, graphene exhibits a variety of transport phenomena that are characteristic of 2D Dirac fermions[11, 12]. Figure 1.3 shows the AFM image of graphene, as well as its TEM images. The structure of graphene can easily be visualized. Graphene becomes visible in an optical microscope if placed on top of a Si wafer with a carefully chosen thickness of SiO_2.[3]

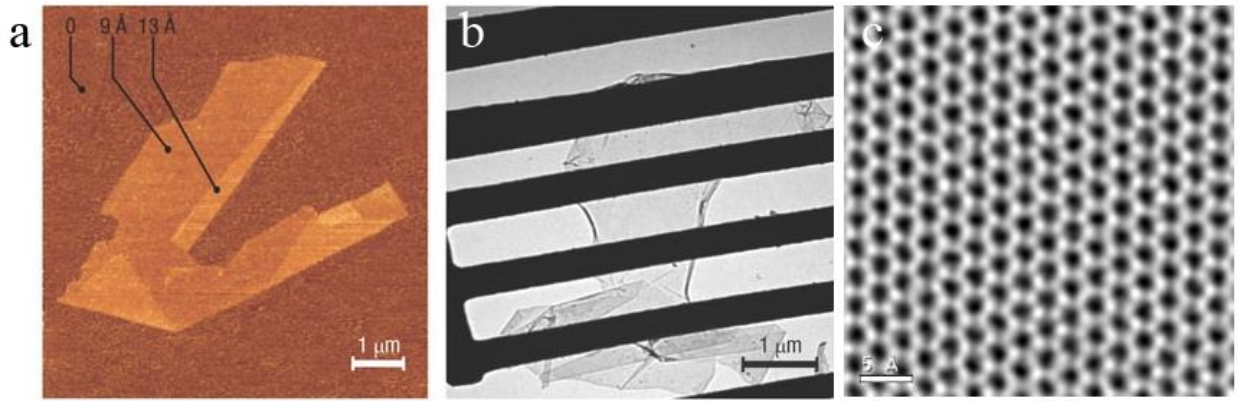

Figure 1.3 Structure of graphene. a. Graphene visualized by atomic force microscopy. b. A graphene sheet freely suspended on a micrometer-size metallic scaffold. c. TEM image of graphene. a, Image reproduced from ref. [13] with permission from United States National Academy of Sciences; b, Image reproduced from ref. [3] with permission from Nature Publication Group; c, X.Xu. group website, University of Washington.

The electronic structure of single-layer graphene can be described using a tight-binding Hamiltonian.[9, 10] The dispersion relations $E^{\pm}(k_x, k_y)$ restricted to first-nearest-neighbor interactions only can be described as

$$E^{\pm}(k_x, k_y) = \pm\gamma_0\sqrt{1 + 4\cos\frac{\sqrt{3}k_x a}{2}\cos\frac{\sqrt{3}k_y a}{2} + 4\cos^2\frac{k_y a}{2}} \qquad (1)$$

where $a = \sqrt{3}\ a_{cc}$ (with a_{cc} = 1.42 Å being the carbon–carbon distance) and γ_0 is the transfer integral between first-neighbor π-orbitals (typical values for γ_0 are 2.9–3.1 eV).[14] Expanding equation (1) at **K**(**K**′) yields the linear π- and π^*-bands for Dirac fermions:

$$E^{\pm}(\kappa) = \pm\hbar v_F|\kappa|$$

Figure 1.4 plots the band structure of graphene.

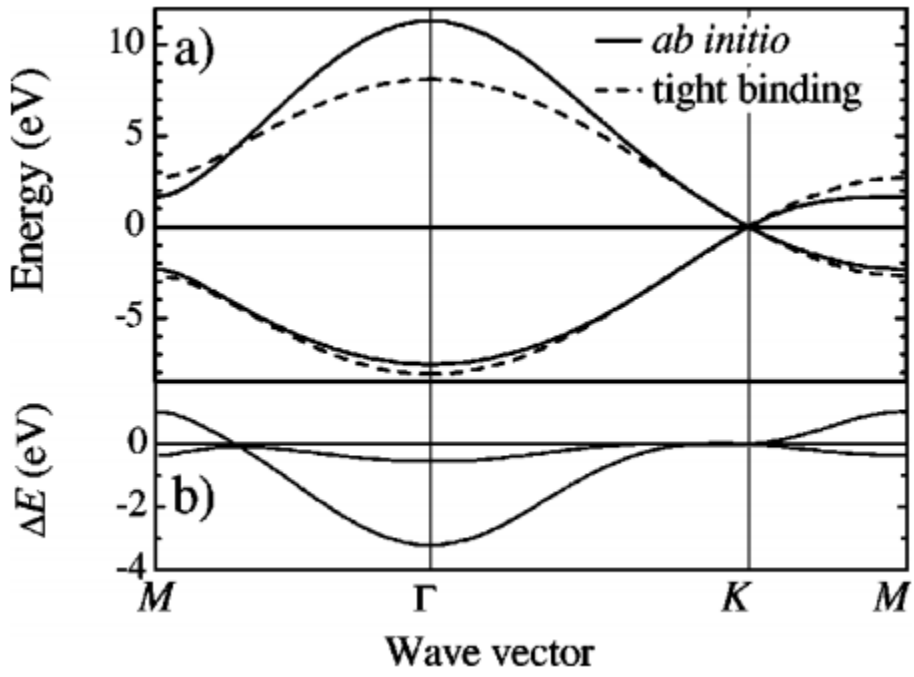

Figure 1.4 Band structure of graphene. a. The converged ab initio calculation of the graphene p and p* electronic bands is shown by the full lines. The dashed lines represent the tight-binding dispersion. b. Difference between the ab initio and tight-binding band structures. Image reproduced from ref. [15] with permission from American Physical Society.

1.1.3 2D materials beyond graphene

Although graphene has attracted enormous amount of interest in the research field due to its remarkable properties, it has also shown many limitations. For example, graphene has a zero

bandgap (E_g), which results in a small current on/off ratio in graphene field-effect transistors (FETs).[16] In addition, the fine control of the thickness of graphene sheets over an entire substrate remains a major challenge.[17] Although many efforts have been made to improve the quality of graphene, such as chemical vapor deposition (CVD),[18, 19] mechanical exfoliation,[13] surface segregation,[20] and liquid-phase exfoliation,[21] it is still very difficult to achieve the graphene quality required for mass production.

Since the discovery of the exotic properties of graphene, 2D layered materials such as transition metal chalcogenides (TMDCs), transition metal oxides, and hexagonal boron nitride (hBN) have gained renewed interest. Because of their distinct properties and high specific surface areas, these 2D materials are important in various applications such as optoelectronics, spintronics, catalysts, chemical and biological sensors, supercapacitors, solar cells, and lithium ion batteries.[22] TMDCs consist of hexagonal layers of metal atoms (M) sandwiched between two layers of chalcogen atoms (X) with a MX_2 stoichiometry. Depending on the combination of chalcogen (typically S, Se, or Te) and transition metal (typically Mo, W, Nb, Re, Ni, or V), [23] TMDCs occur in more than 40 different categories. Together with layered transition oxides,[24, 25] insulator hBN,[26] the common feature of these layered materials is that the bulk 3D crystals are stacked structures from individual layers, as shown in Figure 1.5a. An optical image of monolayer MoS_2 is shown in Figure 1.5b. They involve van der Waals interactions between adjacent sheets with strong covalent bonding within each sheet.[1]

The 2D exfoliated versions of TMDCs offer properties that are complementary to yet distinct from those in graphene. TMDCs typically possess sizable bandgaps around 1–2 eV,[23] ideal for new FETs and optoelectronic devices. For MoS_2, the bulk indirect bandgap of 1.2 eV increases to a direct bandgap of 1.8 eV in single-layer form.[27] The direct bandgap also results

in photoluminescence from monolayer MoS_2, which opens the possibility of many optoelectronic applications. The electronic structure of MoS_2 also enables valley polarization, which is not seen

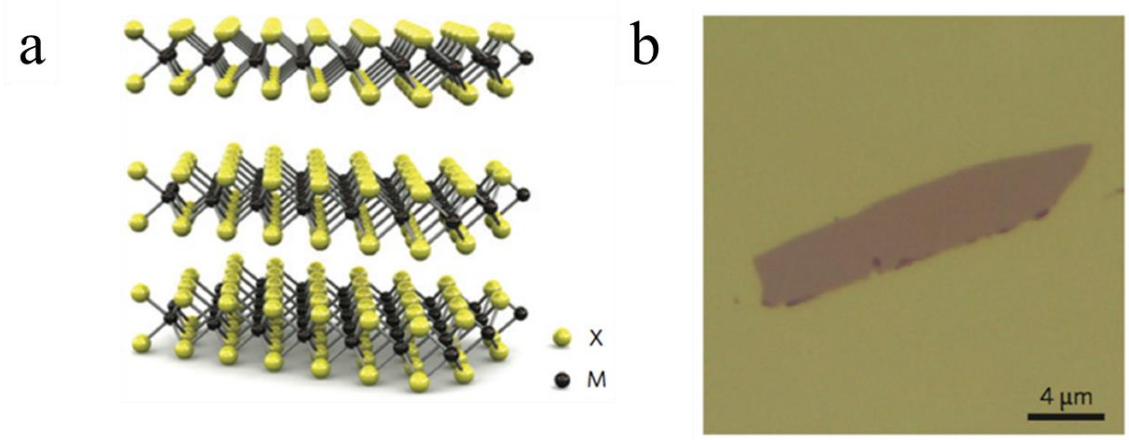

Figure 1.5 Structures of layered 2D materials. a. Three-dimensional schematic representation of a typical MX2 TMDC structure, with the chalcogen atoms (X) in yellow and the metal atoms (M) in grey. b. Monolayer flake of MoS_2 optical microscopy image. a, Image reproduced from ref. [28] with permission from Nature Publishing Group; b, Image reproduced from ref. [28] with permission from IOP Publishing.

Table 1.1 Summary of TMDC materials and properties

	-S_2	**-Se_2**	**-Te_2**
Nb	Metal; Superconducting; CDW	Metal; Superconducting; CDW	Metal
Ta	Metal; Superconducting; CDW	Metal; Superconducting; CDW	Metal
Mo	Semiconducting 1L: 1.8 eV Bulk: 1.2 eV	Semiconducting 1L: 1.5 eV Bulk: 1.1 eV	Semiconducting 1L: 1.1eV Bulk: 1.0 eV
W	Semiconducting 1L: 2.1eV/1.9 eV Bulk: 1.4 eV	Semiconducting 1L: 1.7 eV Bulk: 1.2 eV	Semiconducting 1L: 1.1eV

* The electronic characteristic of each material is listed as metallic, superconducting, semiconducting or charge density wave (CDW). For the semiconducting materials, the bandgap energies for monolayer (1L) and bulk forms are listed. Table reproduced from ref.[27] with permission from Nature Publishing Group.

in bilayer MoS_2.[29-31] In general, there are many interesting layer-dependent properties in 2D materials, including graphene and TMDCs, which differ greatly from the properties of the bulk materials. Table 1.1 summarizes the basic properties of TMDCs.

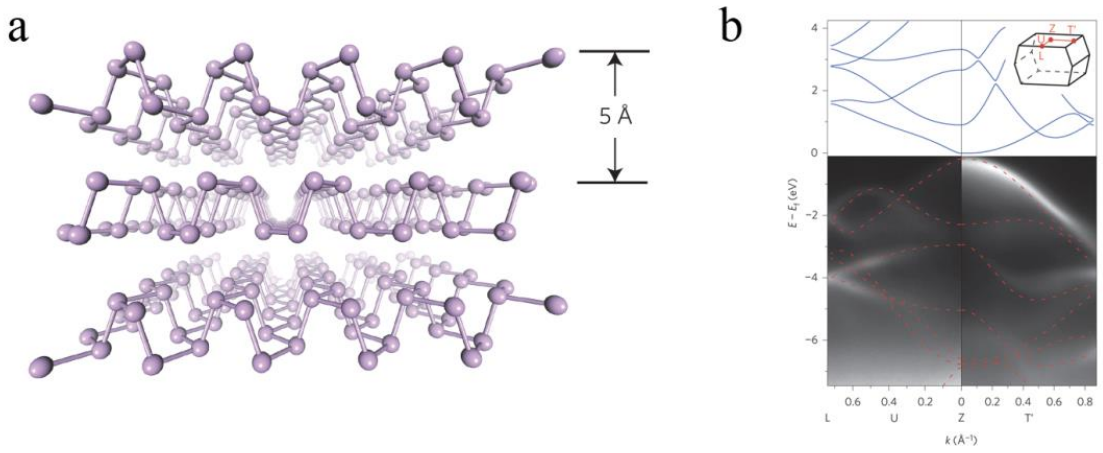

Figure 1.6 Crystal and electronic structure of bulk black phosphorus. a. Atomic structure of black phosphorus. b. Band structure of bulk black phosphorus mapped out by ARPES measurements. Image reproduced from ref. [32] with permission from Nature Publishing Group.

Black phosphorous (BP) is another emerging 2D material that starts to gain increasing interests. Just as in graphene, phosphorene atoms are arranged hexagonally, but in phosphorene the surface is slightly puckered. It is, besides graphene, the only elemental 2D material that can be mechanically exfoliated.[33] With its bandgap, phosphorene provides high on/off ratio as well as a relatively high mobility that is important to electrical engineers.[34] The crystal and electronic structure of BP is shown in Figure 1.6. It has been demonstrated that reliable transistor performance is achieved at room temperature in black phosphorus samples thinner than 7.5 nm, with drain current modulation on the order of 10^5 and well-developed current saturation in the *I*–*V* characteristics. The charge-carrier mobility is found to be thickness-dependent, with the highest values up to ~1,000 $cm^2\ V^{-1}\ s^{-1}$ obtained for a thickness of ~10 nm.[32]

1.2 Electrical properties

For electronic applications, we first need to define some figures of merits that play key roles in electrical device applications.

A transistor performs as a switch for digital applications. In a circuit, a voltage can be applied to source, drain, or gate. The maximum voltage can be applied is called supply voltage V_{DD}. We define I_{DS} as drain-source current, V_{DS} as drain-source voltage, and V_{GS} as gate-source voltage. If $V_{DS} = V_{DD}$ and $V_{GS} = 0$, the I_{DS} we obtained is called "off" current I_{off}. If $V_{DS} = V_{GS} = V_{DD}$, the I_{DS} we obtained is called "on" current I_{on}. A low I_{off} can help reduce power consumption, while a high I_{on} is beneficial to high-speed applications. When a gate voltage larger than the threshold voltage V_T is applied, the source-drain state will change from open-circuit to short-circuit. The rate at which I_{DS} increases with gate voltage V_{GS} is characterized by subthreshold swing (SS), which is expressed in the unit of mV dec^{-1}, or mV of gate voltage required to change I_{DS} by a decade.

Device speed and power consumption are important properties of CMOS integrated circuits. The time required to switch a logic gate is defined as $\tau = CV_{DD}/I_{ON}$, and the energy consumption per operation is defined by dynamic power indicator DPI = CV_{DD}^2, where C is transistor gate capacitance. Therefore, the most efficient way to reduce power consumption is to use a low supply voltage. For analog applications, two important figure of merits are cut-off frequency f_T and maximum oscillation frequency f_{max}, where the former characterizes current gain of the device and the latter characterizes power gain.

Mobility μ is an intrinsic material property that limits device applications. A high carrier mobility not only helps increase I_{ON}, but is also favorable to high-speed applications. For silicon,

μ decreases significantly with doping or thickness reduction.[35] The highest mobility of graphene is reported to be 200,000 cm^2 V^{-1} s^{-1},[36] which favorable in the development of semiconductor technology, especially in radio frequency applications where fast switching and high I_{on} is preferred.[16] However, the zero bandgap of graphene significantly limits its on/off ratio in graphene transistors.

Figure 1.7 shows the mobility versus bandgap for different materials. As mentioned in the previous section, 2D materials beyond graphene, such as TMDCs, have bandgaps mostly ranging from 1-2 eV, which result in a low I_{OFF} and thus a high on/off ratio. For example, a single-layer MoS_2 transistor has demonstrated an on/off ratio larger than 10^4 and an SS smaller than 80 mV dec^{-1}.[28] However, as a tradeoff, the mobilities of TMDCs are relatively low, which is only comparable to silicon. On the other hand, due to the extreme thinness of 2D materials, device scaling is able to bring down the channel length of FETs aggressively. 8 nm channel length has been demonstrated in a MoS_2 FET with a delay time of 60 fs.[37] In such device geometry, μ is hardly an issue since transport in these transistors is considered ballistic.[35]

For radio frequency applications, graphene has shown an intrinsic f_T comparable to III-V transistors thanks to its high mobility and saturation velocity.[38] However, f_{max} of graphene transistors are yet to surpass the performance of III-V and silicon-based devices, which has already achieved 1.2 THz.[39] TMDCs provide pronounced current saturation at the cost of low mobility,[40] making operations at high frequencies difficult to achieve.

1.3 Optoelectronic properties

The optoelectronic properties of CNTs are highly tunable. CNTs can be semiconductors or metals depending on chirality. In this dissertation, we focus on the photoconductivity of CNTs.

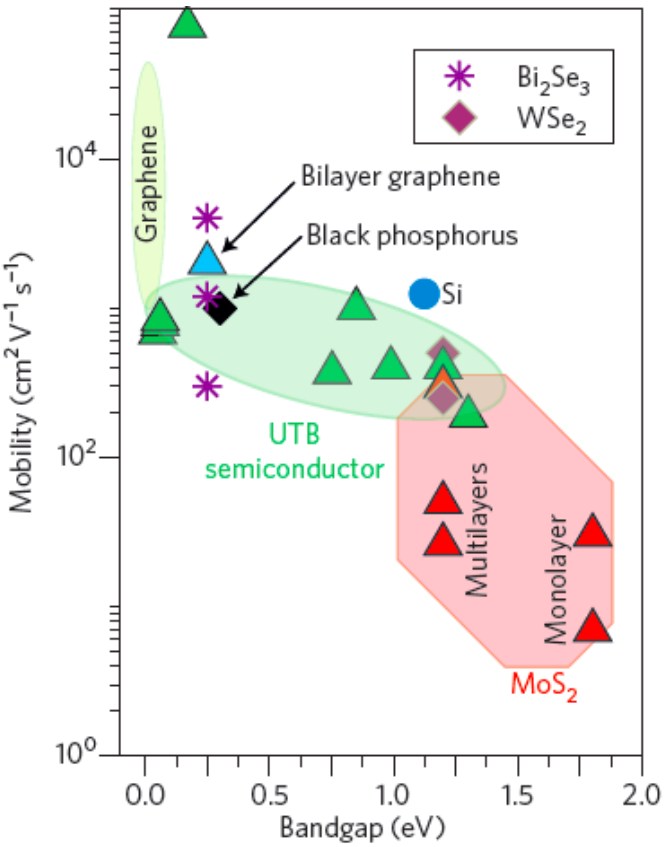

Figure 1.7 Mobility versus bandgap for different materials. Image reproduced from Ref. [35] with permission from Nature Publishing Group.

A semiconducting CNT can act as a nanoscale photodetector that converts light into current or voltage. The principle of operation is that, above-bandgap photons generate excitons in the CNT, which can decay into free electrons and holes. These electrons and holes are either separated by an externally applied bias,[41] by internal fields at the Schottky barriers,[42, 43] at p–n junctions[44] or at defects[45, 46]. When an externally applied bias is used, a change in current (photoconductivity) can be detected, whereas in the other cases a photovoltage is also generated. Focusing and scanning the light along the CNT can identify the active CNT regions generating the photovoltage. Under the assumption that the photocurrent is proportional to the local

potential gradient, the functional form of the band-bending can be extracted by integrating the photocurrent along the length of the CNT.[42, 47, 48] As shown in Figure 1.8, the integrated photocurrent plot shows clearly that the defects in this CNT are associated with potential maxima.

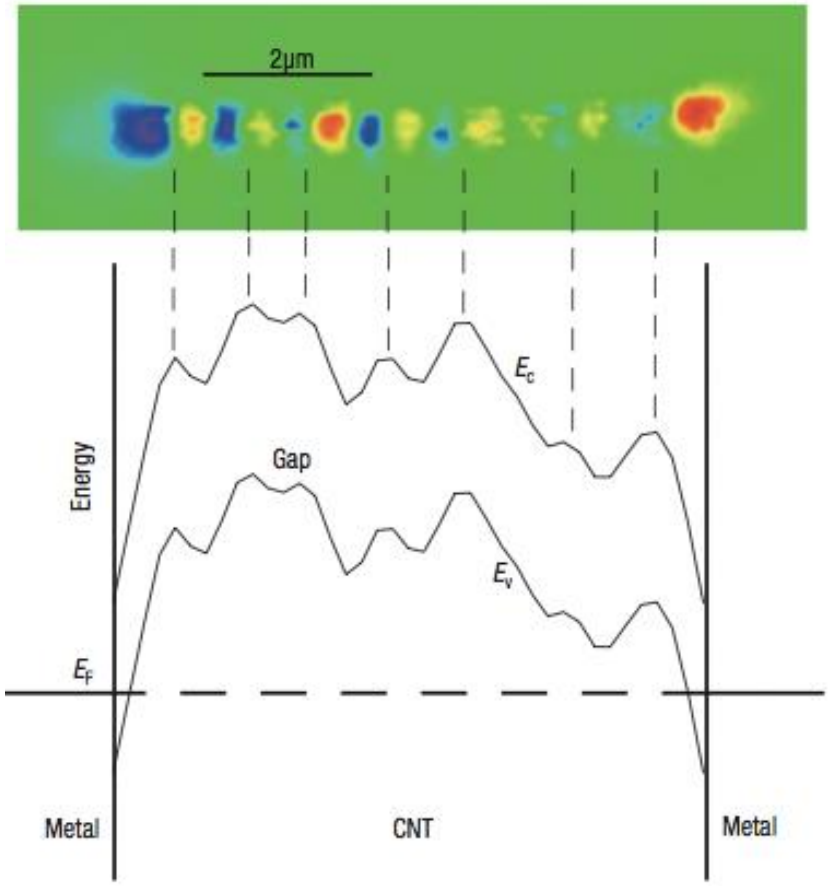

Figure 1.8 Photocurrent microscopy. Photocurrent image of a CNT (top) with many defects. Bottom: band-bending inferred by integrating the photocurrent along the CNT. E_F is the Fermi energy, E_C is the conduction-band energy, E_V is the valence-band energy and "gap" indicates the bandgap between the two bands. Image reproduced from ref. [46] with permission from American Institute of Physics.

Graphene shows remarkable optoelectronic properties which are different from conventional bulk materials. For example, it is optically visible despite being a single layer of

atoms.[49] The linear dispersion of Dirac electrons enables ultra-wide band tunability possible.[14] It is believed that the true potential of graphene lies in its applications in optoelectronics, such as photovoltaic devices,[50, 51] photodetectors,[52, 53] light emitting devices,[54, 55] and optical modulators.[56]

In contrast to graphene, 2D TMDCs have bandgaps in the near-infrared to visible range. Particularly, the single-layer forms of TMDCs possess direct bandgaps, especially suitable for optoelectronic applications. Table 1.2 compares the performance of graphene and 2D material photodetectors. 2D membranes of TMDCs have also been stacked to form van der Waals heterostructures, significantly improving its light absorption.[1, 57] Chapter 2 to Chapter 4 of this dissertation will discuss more on the application of 2D materials, such as photodetectors and photovoltaic devices.

Table 1.2 Comparison of performances of graphene and 2D TMDC photodetectors.

	Device type	Responsivity	Bandwidth	Quantum efficiency
Graphene • Zero bandgap • Broadband • High dark current	Bolometric Photoconduction Heterojunction	~0.2 mA W^{-1} (RT) ~10^5 V W^{-1} (LT) ~0.1 mA W^{-1} ~10 mA W^{-1} ~100 mA W^{-1} (waveguide)	>1 GHz - - >40 GHz >20 GHz	- - - ~1–10% (E) ~10–30% (I)
2D TMDCs • Near-infrared to visible gap • Strong exciton binding • Low dark current	Photoconduction In-plane Out-of-plane Heterojunction In-plane Out-of-plane	 ~1–10^3 A W^{-1} ~0.1 A W^{-1} ~1 mA W^{-1} (zero bias) ~100 mA W^{-1} (zero bias)	 0.1 Hz to >10 kHz ≤200 GHz - -	 ~50% (E) - ~2% (I) (zero bias) ~10–30% (E) (zero bias)

* I and E are internal and external quantum efficiencies, respectively. LT, low temperature; RT, room temperature. Table reproduced from Ref. [58] with permission from Nature Publishing Group.

Chapter 2 Morphology-induced modifications in graphene nanostructures

A large number of theoretical and experimental studies have focused on modifying the mechanical structure of pristine graphene to alter its electrical and optical properties.[59-61] Molecular dynamics (MD) simulations indicate that twisting a graphene nanoribbon leads to a tunable modification of the electrical structure of graphene.[62-65] The ability to change the physical properties of graphene simply by varying its morphology is an attractive option that makes the move to graphene-based photovoltaic technology more viable. It is therefore desirable to investigate the effects of morphology change on graphene properties. Here, we explore the optical and thermal properties of curled graphene ribbons (CGRs).

2.1 Enhanced photocurrent response in CGRs

The fabrication of CGRs is described as follows. Single-layer graphene was grown on copper foil at 950 ^{o}C in the presence of 35 sccm of methane and 8 sccm of hydrogen via chemical vapor deposition. Then a poly-methyl methacrylate (PMMA) layer was spin-coated on top of the graphene film that was grown on the copper foil to hold the graphene film. The copper foil was later removed through wet etching in iron chloride solution, and then the PMMA–graphene film was transferred onto the pre-patterned chip, where 5 mm-wide and 5 mm-deep trenches were etched on 170 mm-thick transparent fused silica substrates via an Oxford 80 RIE and source and drain electrodes were deposited with 5 nm of Ti and 40 nm of Pt via an e-beam evaporator. After the device was dried in air, the sample was heated up to 420 ^{o}C within 1 min and held for 30 min in a furnace in the presence of 200 sccm argon at one atmosphere, which led to a complete evaporation of PMMA.[66] During the evaporation, the non-suspended graphene

adhered to the substrate due to the van der Waals interaction with the substrate, while the suspended part became wrinkled and crumpled and then shrank and curled into a CGR (Figure 2.1). The edges of the graphene structure still remain single-layer as denoted by the white arrows. We then separated each device by physically scratching between the electrodes with sharp needles.

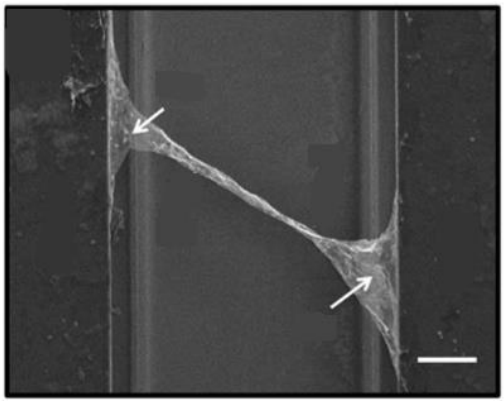

Figure 2.1 Structures of CGRs. SEM image of a CGR device after annealing. Arrows are the regions on the edge that is still single layer. Scale bar is 1 μm.

To evaluate the photon-to-electron conversion efficiency of CGRs, we performed spatially resolved scanning photocurrent measurements on a suspended CGR via scanning photocurrent measurement in comparison with a flat graphene ribbon. Figure 2.2a presents a schematic diagram of a CGR device used in this study. When a diffraction-limited continuous-wave laser spot (1.2 mW, 785 nm) scanned over a CGR transistor suspended on the top of a 170 mm-thick transparent fused silica substrate, the photocurrent signals were collected via a preamplifier and the refection image was recorded through a photodetector. As shown in Figure 2.2e, the photocurrent generated along a CGR is in the range of tens of nanoampere, about two

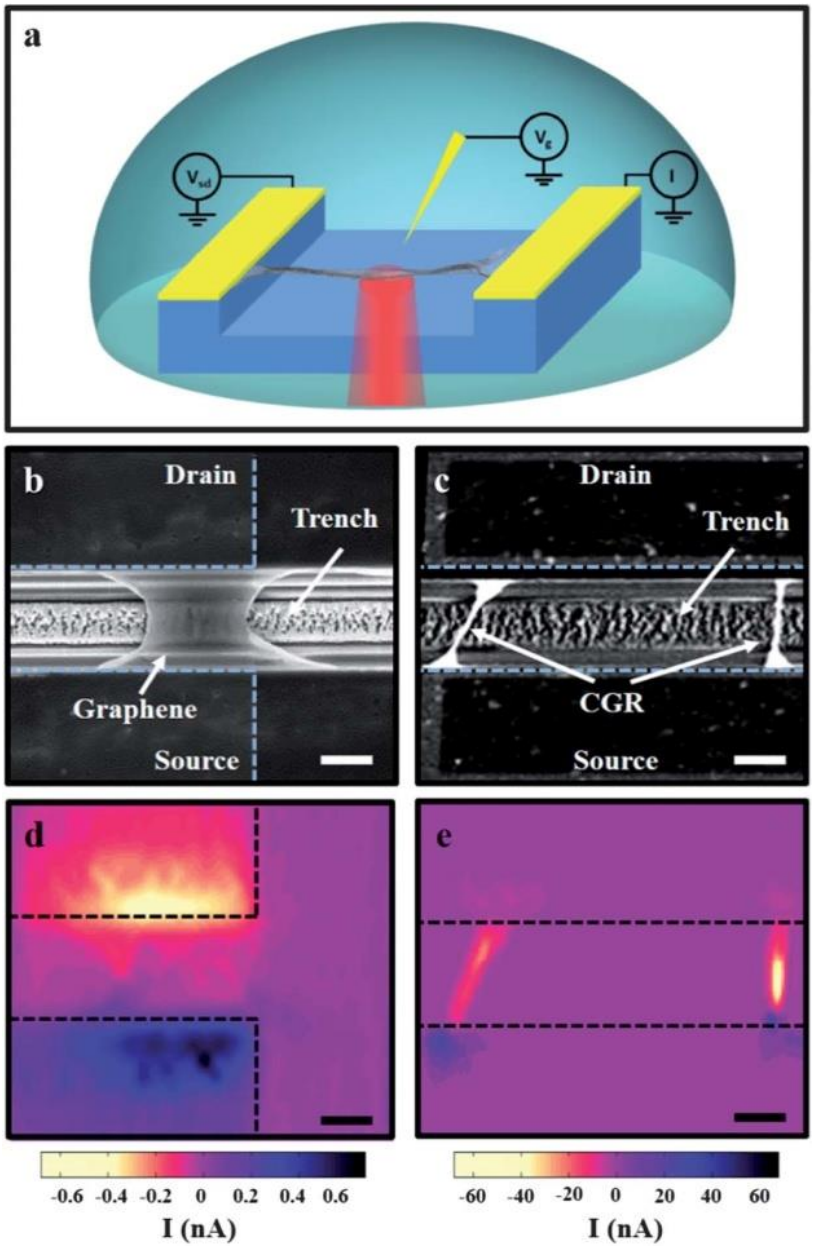

Figure 2.2 Optoelectronic response comparisons between a CGR and a flat graphene ribbon. a. Schematic diagram of the device geometry. Source and drain electrodes are used to apply a voltage across the CGR and the third electrode is used as an electrolyte gate. SEM images of a suspended single-layer graphene device b and a suspended CGR device c, respectively. The laser power measured at the output of the objective was 1.2 mW for both images. The corresponding photocurrent images at $V_g = 0$ V and a zero source–drain bias of the suspended single-layer graphene device d and the suspended CGR device e, respectively. The scale bars represent 5 μm. Blue and black dashed lines are the edges of the electrodes. Image reproduced from Ref. [67] with permission from The Royal Society of Chemistry.

orders of magnitude greater than that generated at graphene–metal contacts in a suspended flat graphene ribbon transistor (Figure 2.2d) and in non-suspended flat graphene ribbon transistors reported previously.

2.2 Laser-induced emission from CGRs

Photoexcited electron–hole pair relaxation occurs mainly in two pathways: photocurrent and photo-induced emission. We investigated the simultaneous photocurrent response and emission of CGRs (Figure 2.3a) and explored their relationships to the incident laser power. As shown in the insets of Figure 2.3b and 2.3c CGR has not only an enhanced photocurrent response, but also strong infrared emission. When the laser power increases from 0.8 mW to 1.9 mW, the photocurrent intensities of a CGR show a linear relationship with the incident laser power (Figure 2.3b). A higher incident laser power generates more hot carriers; the photocurrent intensity is thus proportional to the laser power until saturation.

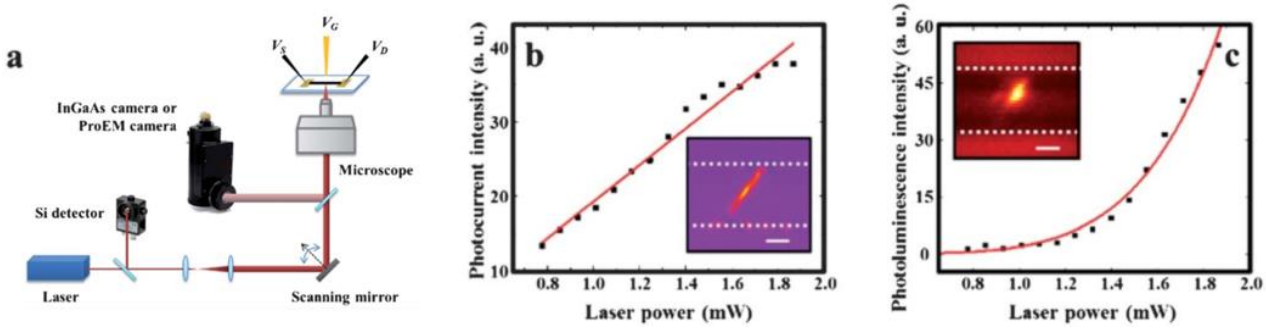

Figure 2.3 Photocurrent and infrared emission intensities of a CGR. a. Schematic diagram of scanning photocurrent and photo- luminescence microscopy (SPPM). b. Photocurrent intensities increase linearly with incident laser power. Inset: the photocurrent image of a p-doped CGR. c. Infrared emission intensities show a non-linear relationship with incident laser power. Inset: the emission image of the corresponding CGR. White dashed lines correspond to the edges of the trench. The scale bars represent 2 μm. Image reproduced from Ref. [67] with permission from The Royal Society of Chemistry.

Figure 2.3c shows that the infrared emission intensity increases nonlinearly when the incident power rises, which is likely due to thermal radiation. When hot carriers relax in CGRs, electronic energy is transformed into Joule heat. Since the CGRs are suspended above the trench, a small fraction of heat can dissipate into the substrate.[68] Therefore, the majority of the heat either dissipates into the metal contacts[69, 70] or radiates into free space as a grey body[71, 72]. At an elevated laser power, Umklapp scattering reduces the thermal conductivity of CGRs and decreases the heat transfer to metal contacts.[73] Thus, the thermal emission into free space plays an important role in heat dissipation of the CGRs. The total amount of infrared emission is modeled by the Stefan–Boltzmann law $I \sim T^{n+1}$, where T is the temperature and n is the dimension of the material. Fitting of the power dependence reveals that the emission intensity I is proportional to $P_L^{5.1}$, where P_L is the incident laser power (Figure 2.3c). On the other hand, $T \sim P_L^{2.1}$ for suspended graphene membranes in air as shown in the previous literature.[74] We find that n is about 1.4, which indicates that CGRs are quasi-1D materials.

We further look into the emission spectrum from the CGRs. Figure 2.4a shows the corrected infrared spectra of the stacked graphene structure, which further confirms that the detected emission is thermal radiation. The thermal radiation spectra can be fitted to Planck's law for grey body to extract the temperature,

$$u(\nu, T) = \varepsilon \frac{8\pi}{h^2 c^3} \frac{(h\nu)^3}{exp(h\nu/k_B T - 1)}$$

In this equation, u is the spectrum energy density, h is Plank's constant, c is the speed of light in vacuum, and T is the temperature. Assuming the emissivity of graphene ε is a constant over the studied energy range, the corresponding temperatures are calculated as shown in Figure 2.4c

(blue squares). A temperature as high as ~800 K is achieved before the graphene structure break down. This calculation is based on the energy distribution of charge carriers. In other words, the temperature we obtained here from thermal emission is the electron temperature.

Raman spectroscopy was also applied to extract the local temperature of freestanding stacked graphene. Compared to Raman G-mode, 2D-mode shows weaker gate voltage dependence near the Dirac point as well as a larger first-order temperature coefficient. [75] Therefore, we scale the Raman 2D-mode downshift with temperature. Since the stacked graphene is not a uniform structure, we first determine on a specific region the Raman 2D peak shift with temperature. We picked a part of the structure that displays the highest thermal emission intensity. The stacked graphene was then placed in a microscopy cryostat (Janis) operating above room temperature with the sample temperature controlled by a heating stage. At moderate temperatures, the temperature dependence of the optical excitation can be approximated as a linear function. We obtain the Raman 2D-mode temperature-scaling coefficient of -0.066 cm^{-1} K^{-1} for the specific region in stacked graphene (Figure 2.4c inset). In our experiment, the temperature of the whole structure was raised in a vacuum chamber. Raman measurements thus indicate the temperature of phonons to which 2D mode anharmonically couples.[68] A series of Raman 2D peaks were then obtained at the same region as the stacked graphene structure at different excitation laser powers as shown in Figure 2.4b. At low laser powers, thermal emission from the structure was too weak to be detected. At higher laser powers (above 1.785 mW), thermal emission and Raman 2D modes were obtained in the same spectrum. Based on the Raman-temperature scaling coefficient, the phonon temperatures of stacked graphene under various laser excitation powers were obtained (Figure 2.4c red triangles). We noticed that the electron temperature from thermal emission was higher than the phonon

temperature. Previous reports suggest that no significant non-equilibrium exist between electrons and phonons in electrically heated single-layer graphene[68, 71]. However, in the case of stacked graphene structure, electrons are not fully equilibrated with phonons modes. We recently reported that such stacked graphene structure exhibits a two-order magnitude enhancement in photocurrent response[67]. Compared to flat graphene ribbon, the much larger amount of charge carriers generated in the stacked graphene structure may slow down the electron-lattice relaxation, resulting in a higher temperature.

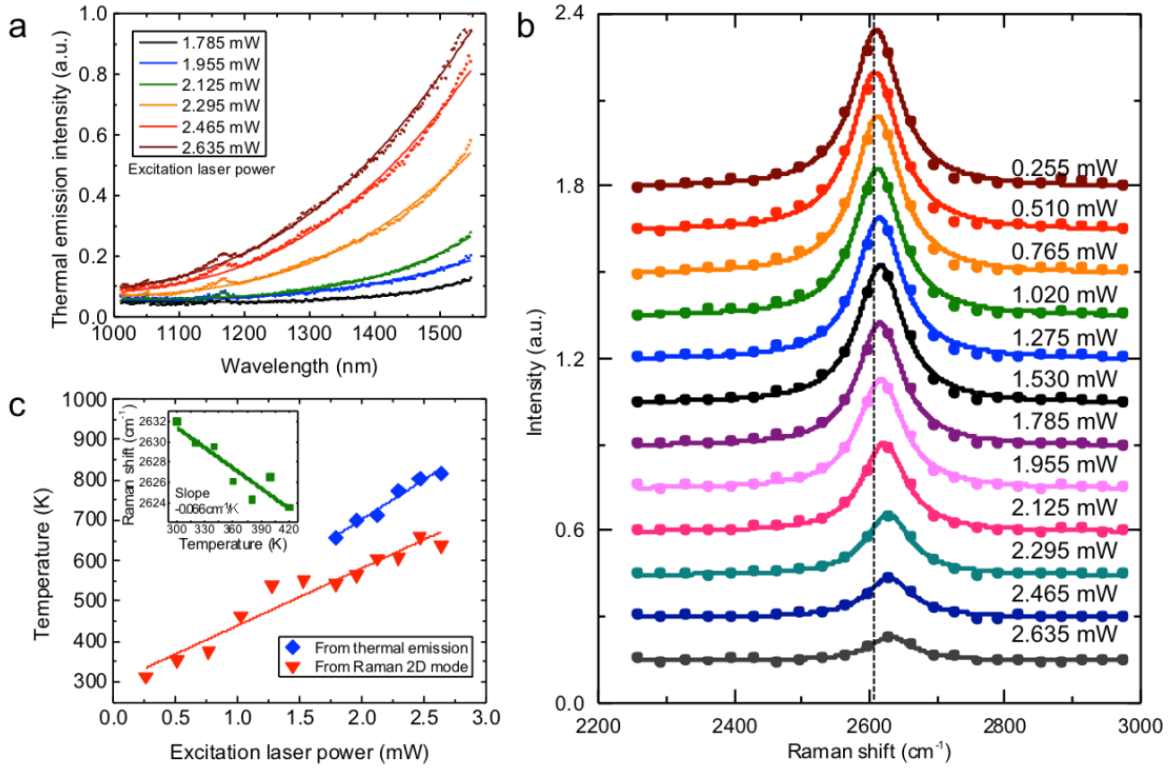

Figure 2.4 Electron and phonon temperatures of CGRs. a. Near-infrared emission spectra of stacked graphene ribbons under different laser. Solid lines are fits of grey body radiation. b. Raman 2D peaks of stacked graphene ribbons under different laser powers. The experimental data is fitted by Lorentzian function. c. Comparison of stacked graphene temperatures. Blue dots are temperatures extracted from thermal emission. Red dots are temperatures extracted from Raman 2D peak shift. Inset: temperature dependence of Raman 2D peak for stacked graphene. The solid lines are linear fittings of the data. Image reproduced from Ref. [76] with permission from American Institute of Physics.

Chapter 3 Light-matter interactions at metal-semiconductor interface

3.1 Metal-semiconductor interface

We first briefly review the interface between metal and semiconductor.

The junction between metal and semiconductor can be either Schottky battier or ohmic contact, depending on the characteristics of the interface. Figure 3.1 shows a band diagram of metal-semiconductor junction after it comes to equilibrium. For this n-type semiconductor, a Schottky barrier is formed at the junction, the barrier height is defined as

$$\phi_B = \Phi_M - \chi$$

where Φ_M is the work function of the metal and χ is the electron affinity. Table 3.1 summaries the work function and measured Schottky barrier of different metals.

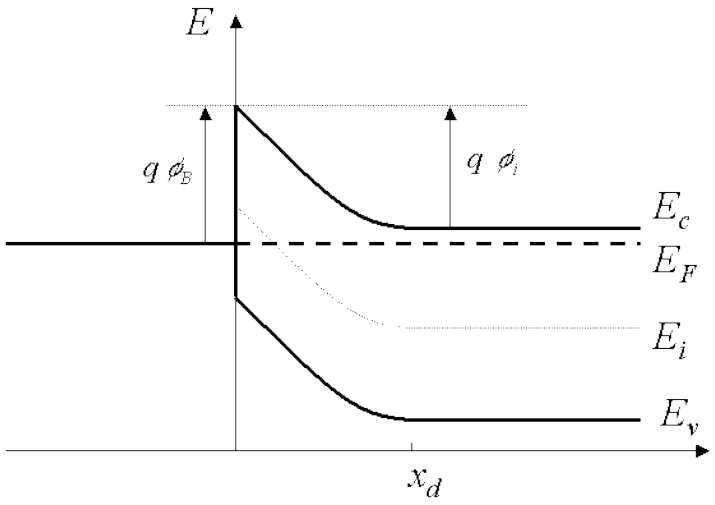

Figure 3.1 Band diagram of metal-semiconductor interface in thermal equilibrium. For this n-type semiconductor, a Schottky barrier is formed. Image reproduced from Ref.[77] .

Table 3.1 Measured Schottky barrier heights for electrons on N-type silicon (φ_{Bn}) and for holes on P-type silicon (φ_{Bp})

Metal	**Mg**	**Ti**	**Cr**	**W**	**Mo**	**Pd**	**Au**	**Pt**
φ_{Bn} (V)	0.4	0.5	0.61	0.67	0.68	0.77	0.8	0.9
φ_{Bp} (V)		0.61	0.50		0.42		0.3	
Work function ψ_M (V)	3.7	4.3	4.5	4.6	4.6	5.1	5.1	5.7

* Table reproduced from Ref. [78].

If the contact resistance between metal and semiconductor is small, an ohmic contact is formed. Quantum mechanical tunneling plays an important role in the operation of ohmic contact. As shown in Figure 3.2, electron with energy E encounters an energy barrier V_H. If V_H >E, the electron wave becomes a decaying function. Part of the electron wave can go through the barrier with reduced amplitude. We define R_C as specific contact resistance,[79]

$$R_c \propto exp\left(H\varphi_{Bn}/\sqrt{N_d}\right)$$

where $H = \frac{4\pi}{h}\sqrt{\varepsilon_s m_n/q}$. Therefore, the semiconductor needs to be heavily doped and φ_{Bn} needs to be small to obtain a small contact resistance.

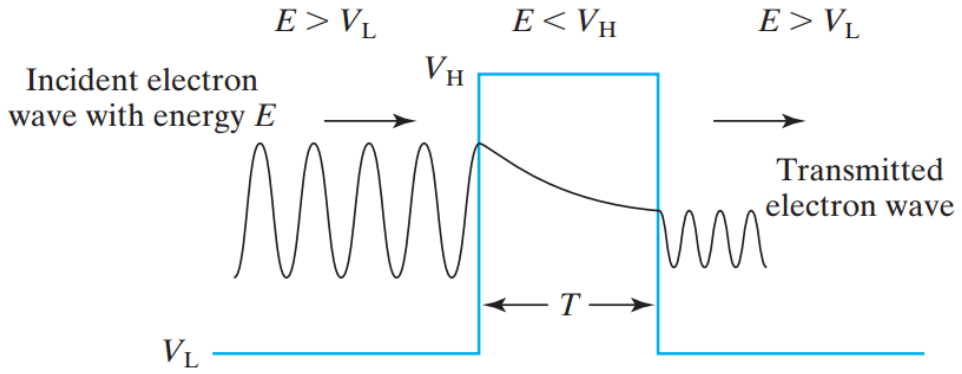

Figure 3.2 Quantum mechanical tunneling. Image reproduced from Ref. [79].

3.2 Polarized photocurrent response in black phosphorous FETs

2D layered crystals have become one of the most attractive materials for future electronics and optoelectronics due to their unique properties. Graphene has a zero bandgap and ultrafast recombination of the photoexcited electron–hole pairs which limit graphene's potential in FET applications and photovoltaic generation.[79, 80] In contrast, FETs made from 2D transition metal dichalcogenides (TMDCs) show very high on/off current ratios and sizeable bandgaps (>1 eV), but their relatively low carrier mobility limit their applications in both electronics and optoelectronics.[28, 81-83] Recently, few-layer black phosphorus (BP) has shown excellent performances for transistors.[32-34, 84] Their drain current modulation is comparable to TMDC FETs and the carrier mobility of BP is typically higher than that of TMDCs. While the bandgap of bulk BP is 0.3 eV, its few-layer structures have a thickness-dependent direct bandgap ranging from 0.3 eV to 2 eV, opening up new opportunities for optoelectronic applications. More interestingly, the electrical and optical conductivities of BP are anisotropic, which is different from other 2D materials that have isotropic in-plane properties.

We fabricated few-layer BP transistors and characterized their electrical transport properties. Ultrathin BP crystals were obtained by repeatedly exfoliating of a bulk BP crystal. This few-layer BP flake was subsequently transferred to a degenerately doped Si substrate with a 290 nm SiO_2 layer. The electrodes were defined by e-beam lithography and evaporated with 5 nm Ti and 50 nm Au. All the experiments were performed in a vacuum condition to avoid surface oxidation of BP. The inset of Figure 3.3 shows an optical image of the BP transistor. The scale bar is 10 μm. The thickness of BP is 8 nm as determined by AFM. Four electrodes were defined to measure the conductance of the BP flake. At room temperature, the BP flake shows a

predominantly p-type behavior with an on/off ratio of 10^4 at V_{ds} = −50 mV (Figure 3.3). The field-effect mobility of the BP flake is estimated by

$$\mu = \frac{L}{W}\frac{dI_{ds}}{dV_{bg}}\frac{1}{C_{bg}V_{ds}}$$

where L=17.3 μm is the channel length, W=5.9 μm is the channel width, C_{bg}=1.2×10^{-8} F cm^{-2} is the capacitance of the Si back gate. From the slope of the gate-dependent conductivity measurement, we estimate the mobility of the BP is 52 cm^{-2} V^{-1} s^{-1}. This value is lower than the mobility of bulk BP due to the ultra-thinness of the BP flake.

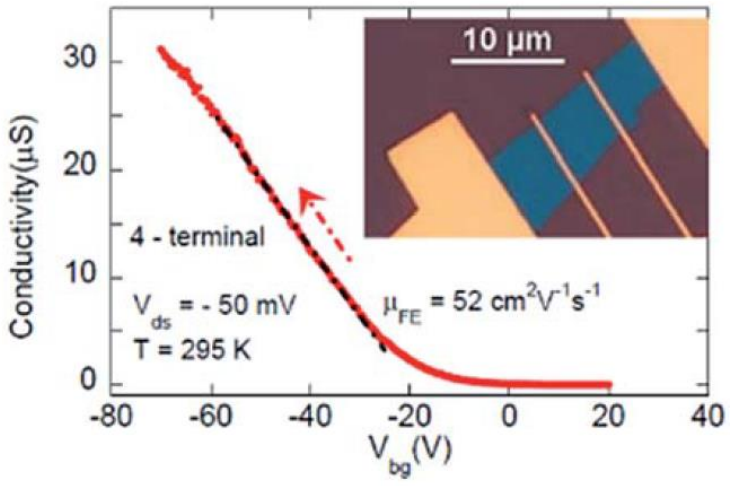

Figure 3.3 Electrical transport properties of BP FET. The conductivity is measured by four-terminal method. Inset: optical image of the BP FET. Image reproduced from Ref. [85] with permission from The Royal Society of Chemistry.

To explore the anisotropic nature of BP FETs, we performed spatially resolved polarization-dependent scanning photocurrent measurements on the BP in a Janis ST-500 Microscopy Cryostat under high vacuum (~1×10^{-6} Torr). A diffraction-limited laser spot (λ = 785 nm, 1.58eV) was scanned over the BP FET by a two-axis scanning mirror with nanometer

spatial resolution and photocurrent signals were recorded as a function of position, resulting in a spatially resolved photocurrent map of the device. The reflection of the incident laser beam was simultaneously recorded by a Si photodetector to locate the position of the sample. Figure 3.4a shows a series of photocurrent images recorded at different laser polarizations, where the polarization angle θ = 0° is indicated in the reflection image in Figure 3.4b. In the reflection image, four gold electrodes are shown as light gray areas. The corresponding photocurrent images were recorded at a zero drain-source bias and V_{bg} = –10 V, where red/blue color corresponds to positive/negative current. The majority of photocurrent responses are observed in the four electrode regions where gold electrodes and the BP sample contact. At a zero drain-

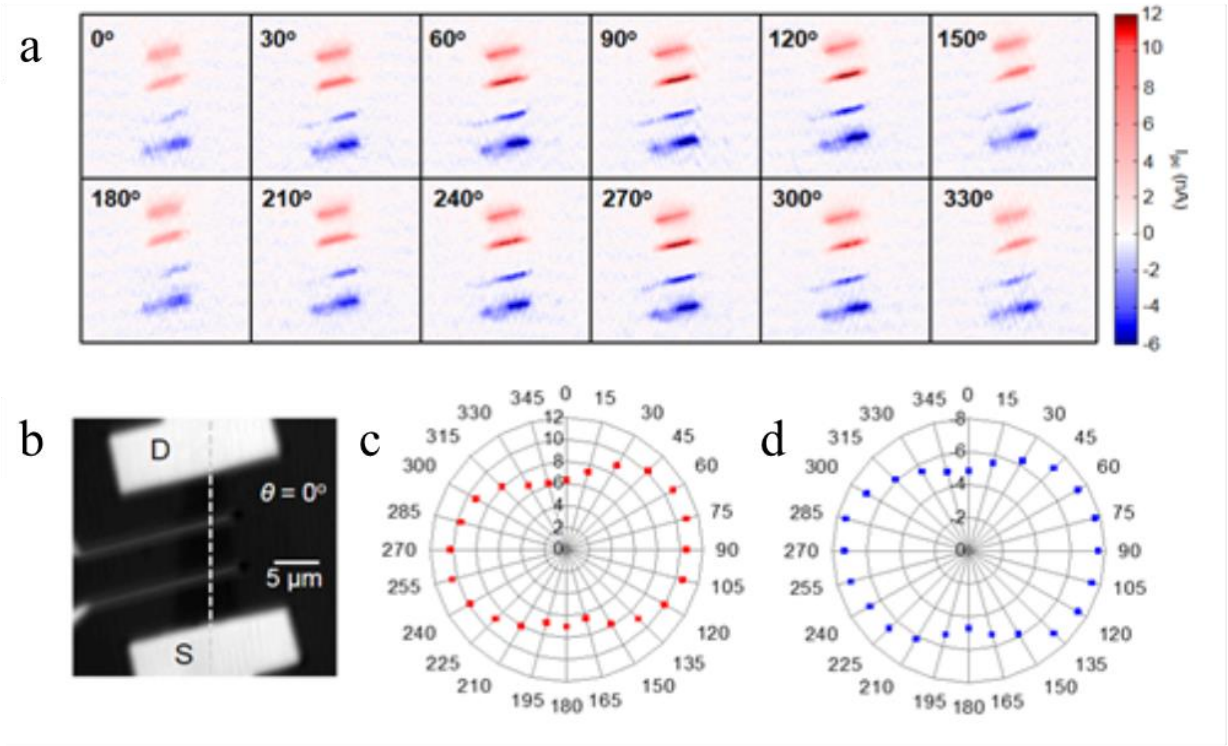

Figure 3.4 Polarized photoresponse of BP. a. Photocurrent image of the BP FET at different laser polarizations. b. Corresponding gray-scale reflection image showing laser polarization direction at θ = 0°. The polarization dependence of strongest positive (red)/negative (blue) photocurrent response at the drain/source contact region is shown in c and d, respectively. Image reproduced from Ref. [85] with permission from The Royal Society of Chemistry.

source bias, the strongest positive/negative photocurrent responses in the drain/source contact region for each map are shown in the polar plots in Figure 3.4c and 3.4d, respectively. The BP device shows a polarization-dependent photocurrent response, with the maximum signal intensity observed at θ around $90^o/270^o$ or along the x-axis, and the minimum intensity at θ around $0^o/180^o$ or along the y-axis.

To further investigate the photocurrent generation mechanisms in BP FETs, we performed gate-dependent scanning photocurrent measurements on BP transistors at 77 K, where the hysteresis behavior in the transfer characteristics is negligible as the charge trapping is suppressed at low temperatures.[86, 87] Figure 3.5a and 3.5b display the reflection and photocurrent images of a BP FET at a zero drain-source bias with a gate voltage V_g = –30 V, respectively. Only the middle two electrodes were connected. By sweeping the gate voltage from –60 V to 60 V while recording the photocurrent along the channel direction of the BP FET (dashed line in Figure 3.5a), we obtained the gate-dependent scanning photocurrent map (Figure 3.5c).

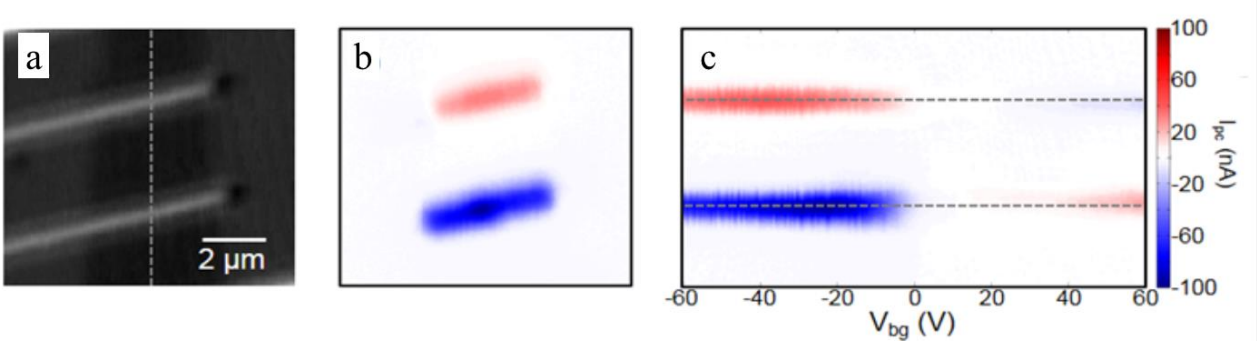

Figure 3.5 Gate-dependent photocurrent measurements of BP transistors. a. Reflection and b. photocurrent images of a BP FET at V_{bg} = –30 V and a zero drain-source bias, respectively. c. The gate-dependent scanning photocurrent images at a zero drain-source bias as V_{bg} varying from -60 V to 60 V. The laser scanning position is indicated by the white dotted line in a. Image reproduced from Ref. [85] with permission from The Royal Society of Chemistry.

From the scanning photocurrent map, we are able to extract the gate-dependency of photocurrent at the two electrodes. Figure 3.6a plots the gate dependency of the photocurrent intensities at the two electrodes along with the electrical transport properties of the BP flake measured between the two electrodes. The electrical transport measurements suggest that the BP is turned to "off" state when the applied gate voltage is between –12 V to 52 V, where the Fermi level lies inside the bandgap of BP. At V_g =14 V, photocurrent signals on both electrodes were zero, indicating a flat band situation (Figure 3.6b middle) where the band structure at BP-metal junction is flat and no built-in electrical field will separate the electron-hole pairs generated by the laser. The gate-dependent band structure modulation can be modeled by

$$\Delta E_b = e\alpha V_g$$

where E_b is the energy from the Fermi level to the nearest of the conduction and valence bands, and α is a numerical constant that measure how efficiently the gate modulates the band energies. The bandgap of BP is 0.3 eV from previous literature.[88] Thus, α is calculated α=0.0047. The Schottky barrier height is obtained to be $\Phi_B = \Phi_M - \chi = 0.2$ V.

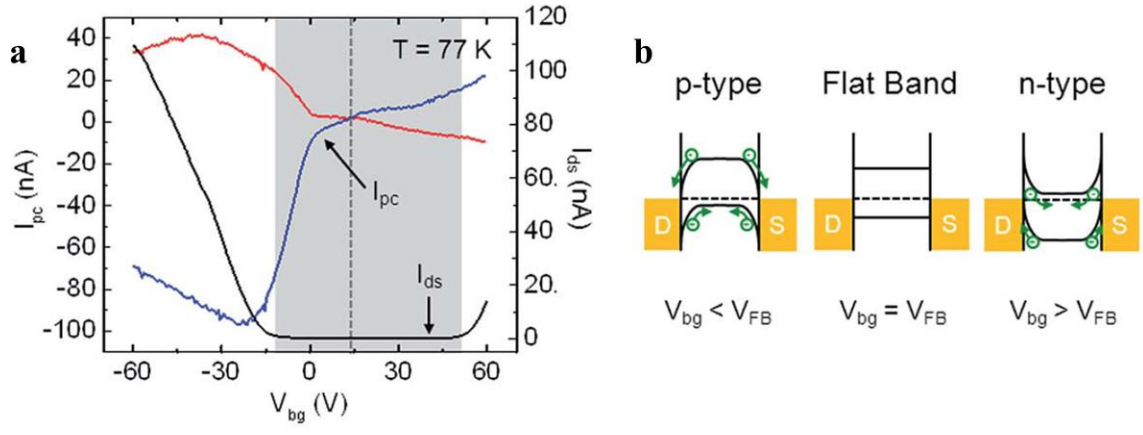

Figure 3.6 Estimating BP-metal Schottky barrier height. a. Gate-dependent photocurrent and electrical transport measurement of BP FET. b. Band structure of BP at different gate bias. Image reproduced from Ref. [85] with permission from The Royal Society of Chemistry.

The photocurrent signal exhibits monotonic gate voltage dependence in the off-state (V_{bg} between –12 V and 52 V), indicating that the photovoltaic effect (PVE) plays an important role in its photocurrent generation. Interestingly, the photocurrent signals show strong non-monotonic gate dependence when V_{bg} is lower than –10 V, which contradicts the prediction of the photovoltaic mechanisms. Therefore, photothermoelectric effect (PTE) may be the main photocurrent generation mechanism in this region. The photovoltage due to PTE, V_{PTE}, can be expressed as

$$V_{PTE} = (S_1 - S_2)\Delta T$$

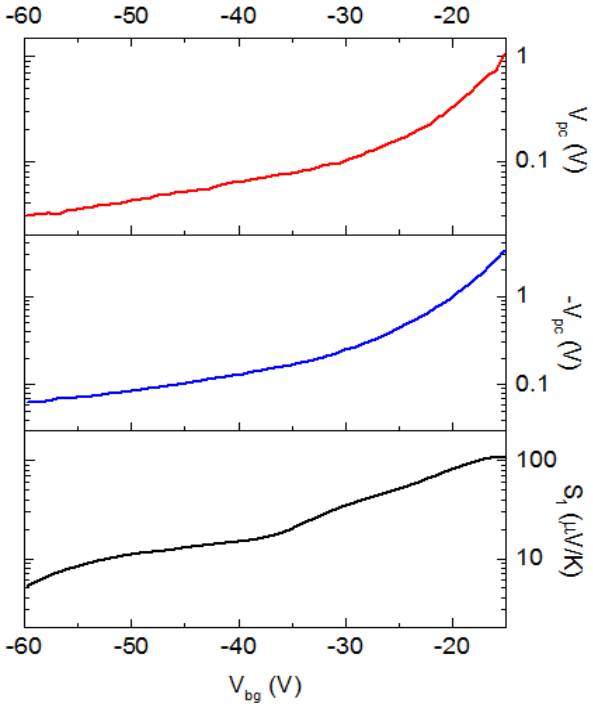

Figure 3.7 Photovoltage signals and calculated Seebeck coefficient at different V_{bg}. Photovoltage is defined as $V_{pc} = I_{pc}R$ (red and blue curves), and Seebeck coefficient is the black curve. Image reproduced from Ref. [85] with permission from The Royal Society of Chemistry.

The Seebeck coefficient, *S*, can be derived from the Mott relation,[89-91]

$$S = -\frac{\pi^2 k_b^2 T}{3e}\frac{1}{G}\frac{dG}{dV_g}\frac{dV_g}{dE}\bigg|_{E=E_F}$$

where k_b is the Boltzmann constant, e is the electron charge, and E_F is the Fermi energy. The calculated Seebeck coefficient of BP S_1 is shown in Figure 3.7, along with the photovoltage ($V_{pc} = I_{pc}R$, where I_{pc} is the photocurrent intensity and R is the resistance) generated in the junction area. The photovoltage signals have similar gate dependence to the calculated thermoelectric power (S_1). Thus, PTE is also likely to have contributed to the photocurrent generation at BP-electrode junctions.

Finally, we estimate the electrostatic potential along the BP flake by bias-dependent photocurrent microscopy. First, a series of photocurrent images were recorded at different V_{ds} as shown in Figure 3.8b. The bias applied are from 0.2 V to –0.2 V in 0.1 V steps. Note that little photocurrent features are observed in the middle of the BP flake, and strong photocurrent were observed in the metal-BP contact region. We plot photocurrent cuts along the BP flake at different biases in Figure 3.8a. When strong positive bias was applies, the photocurrent signals in the drain contact regions were enhanced. Similarly, when negative biases are applied, photocurrent signals at source electrodes become stronger.

The local electrical field is roughly proportional to the local photocurrent signals in the BP flake. Therefore, we are able to deduct the electrostatic potential along the BP FET by integrating the photocurrent signals. Figure 3.8c shows the calculated electrostatic potential at different biases. The large potential drop along the BP-electrode interface indicates relatively large contact resistance due to Schottky barrier.

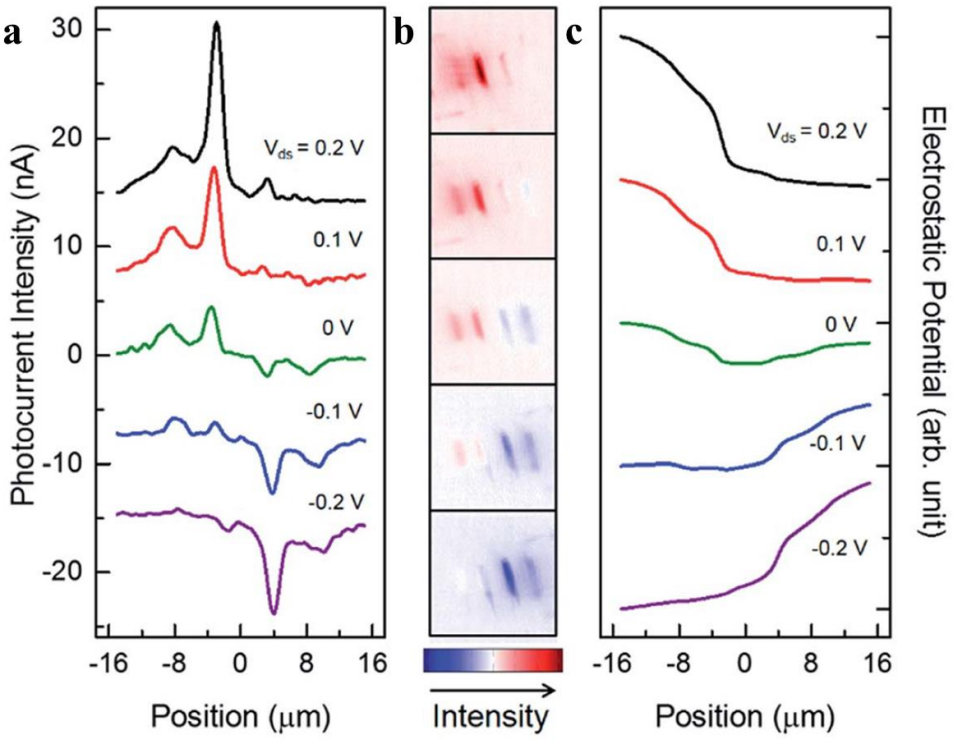

Figure 3.8 Bias-dependent photocurrent of BP FET. a. Photocurrent signals along the BP flake in b, where photocurrent images are recorded in different V_{ds} as marked. c. Electrostatic potential calculated from bias-dependent photocurrent microscopy. Image reproduced from Ref. [85] with permission from The Royal Society of Chemistry.

3.3 Photocurrent response at MoS_2-metal junction

We further investigate the photocurrent generation mechanisms at few-layer MoS_2-metal junction. Few-layer MoS_2 crystals (6 nm - 10 nm) were produced by repeated splitting of bulk crystals using a mechanical cleavage method, and subsequently transferred to a degenerately doped Si substrate with 290 nm SiO_2. MoS_2 field effect transistors (FETs) were subsequently fabricated using standard electron beam lithography and electron beam deposition of 5 nm Ti and 40 nm Au, where the Si substrate is used as the back gate. The inset of Figure 3.9a shows an AFM image of a typical MoS_2 device. The length of metal electrodes is 10 μm and the widths of

the wide and narrow electrodes are 2 μm and 200 nm, respectively. We measure the properties of the devices using a Keithley 4200 semiconductor parameter analyzer in a Lakeshore cryogenic probe station under high vacuum (1×10^{-6} Torr). Figure 3.9 shows the electrical characteristics of a 9 nm thick MoS_2 FET (as determined by AFM). When the gate voltage was swept from 0 to 60 V, the I_{ds}-V_{ds} curves are close to linear, exhibiting ohmic characteristics (Figure 3.9a). This result is in agreement with a previous report that a negligible Schottky barrier between the Au electrodes and MoS_2 (~50 meV) is formed.[92] The device displays a predominately n-type behavior, with the estimated room-temperature field-effect mobility $\mu \sim 50$ cm^2 V^{-1} s^{-1} as extracted from the gate dependence of four-terminal conductivity σ (Figure 3.9b).[93] As temperature decreases, the mobility increases following a $\mu \sim T^{-2.0}$ dependence, consistent with the recent results on high quality MoS_2 encapsulated by boron nitride (Figure 3.9b inset).[94]

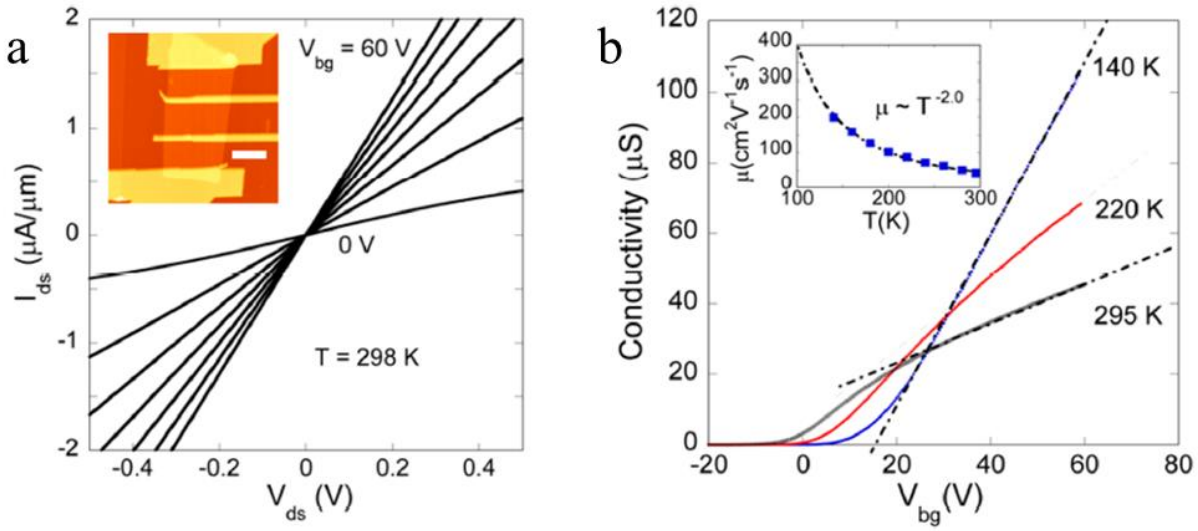

Figure 3.9 Electrical transport characterization of a MoS_2 FET. a. I_{ds} as a function of V_{ds} at different gate biases. Inset: an AFM image of the MoS_2 transistor. b. Gate-dependent conductivity measurement of the MoS_2 transistor at different temperatures. Inset: Mobility as a function of temperature. Image reproduced from Ref. [95] with permission from American Chemical Society.

Similar to BP FET, we performed spatially resolved scanning photocurrent microscopy on the same setup (Figure 3.10a) to investigate the local photoresponse at MoS_2-metal junctions in high vacuum (1×10^{-6} Torr). Figure 3.10b shows a scanning photocurrent image of a MoS_2 device at zero bias, and Figure 3.10c shows its corresponding reflection image that was recorded simultaneously. The outer two electrodes of the MoS_2 FET were used as source and drain and the middle two electrodes were floating during the measurement. We compare the photocurrent signals $\Delta I_{pc} = I_{ds,illumination} - I_{ds,dark}$ under laser illumination of different wavelengths (532, 785, and 1550 nm). Here, the source-drain bias is10 mV. Under 532 nm (2.33 eV) illumination, the photocurrent response is much stronger than under 785 nm (1.58 eV) and 1550 nm (0.8 eV) illumination of the same power (Figure 3.10d). The difference in photocurrent intensity can be explained by considering the bandgap structure of few-layer MoS_2. Under 532 nm laser illumination, electrons that are efficiently excited through a direct bandgap close to 1.9 eV at K(-K) points (Figure 3.10e), which cannot happen for 785 nm laser illumination that has a smaller energy than the direct bandgap. The indirect bandgap optical transition between Brillouin zone Γ point and K point in few-layer MoS_2 (1.2 eV) requires a phonon to preserve the momentum, Therefore, the quantum efficiency is relatively low, resulting in a significant reduction of PVE-induced photocurrent response for 785 nm laser. Upon 1550 nm (0.8 eV) illumination, a non-negligible photocurrent response was observed despite the laser energy cannot excite and electrons from the valence band to the conduction band. Therefore, PTE or other new mechanisms are required to explain the photocurrent generation when the photon energies below the direct bandgap of MoS_2.

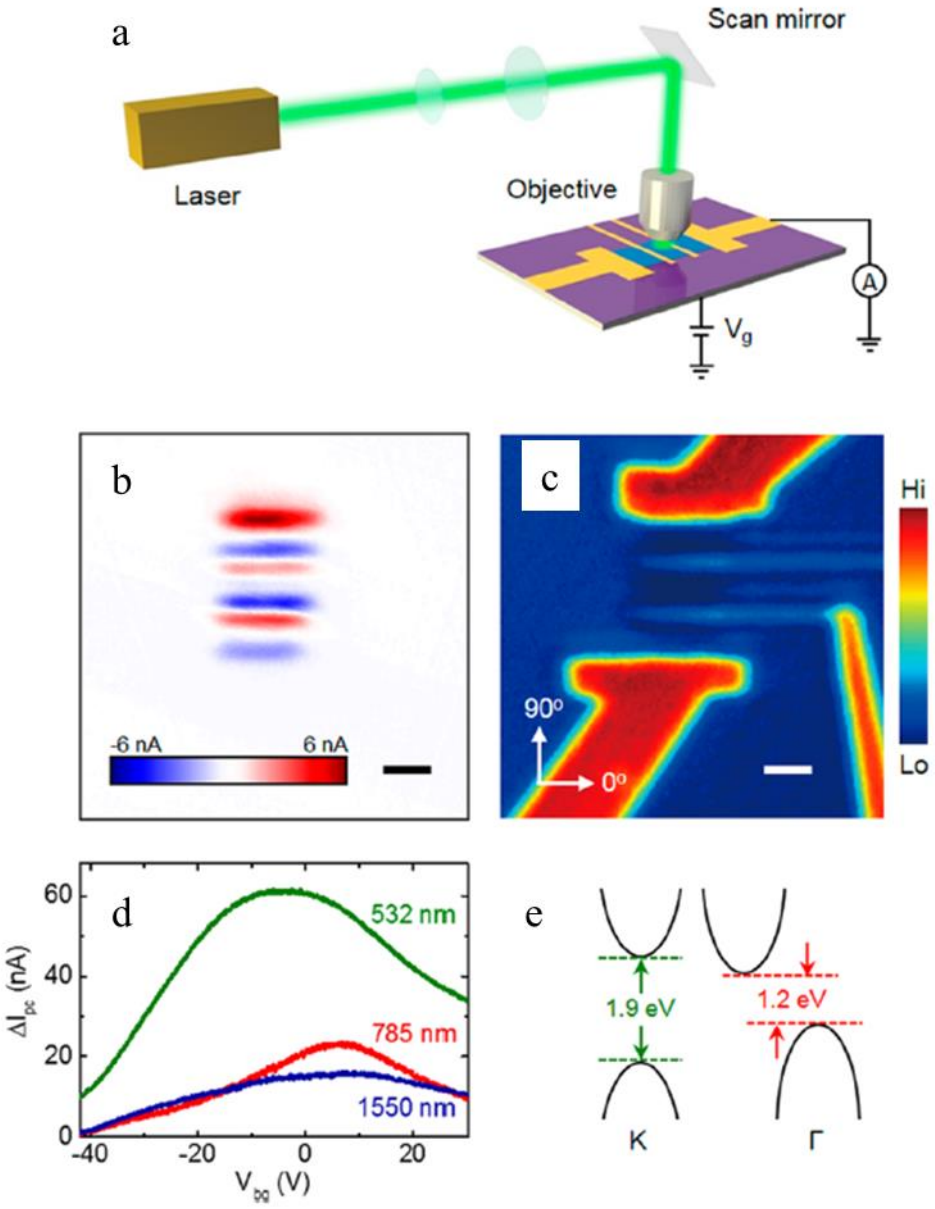

Figure 3.10 Photocurrent responses at MoS_2-metal junction. a. Schematic illustration of the MoS_2 device and the optical setup. b. Scanning photocurrent image and c reflection image of the MoS_2 device illuminated by 785nm laser. The scale bars are 2 μm. d. Photocurrent response of the MoS_2 FET as a function of gate voltage with illumination of 532 nm (green curve), 785 nm (red curve), and 1550 nm (blue curve) laser, respectively. The lasers were defocused to form a spot large enough to cover the entire MoS_2 flake. e. Band structure of few-layer MoS_2, an indirect bandgap semiconductor with a direct bandgap at K (-K) points. The valence band splitting is not shown. Image reproduced from Ref. [95] with permission from American Chemical Society.

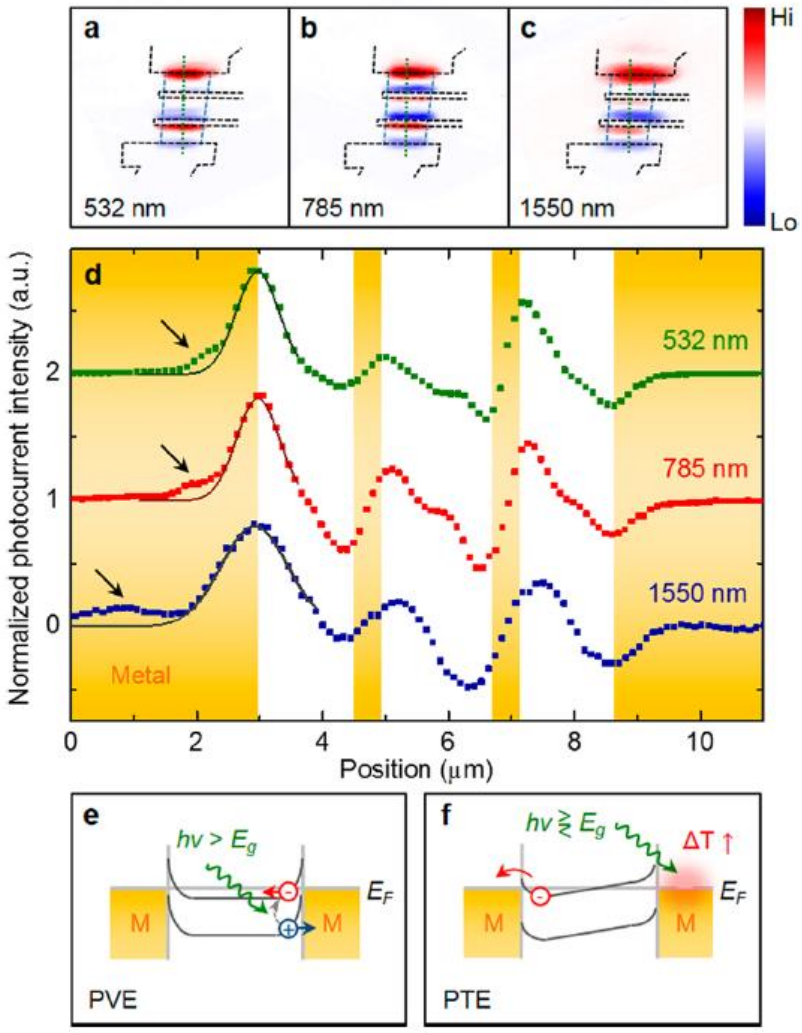

Figure 3.11 Different photocurrent generation mechanisms at MoS_2-metal junction. a. Scanning photocurrent image of MoS_2 FET by 532 nm laser, b. 785 nm laser, and c. 1550 nm laser. d. Line profiles of the photocurrent response along the dashed green lines in a-c. e. Schematic illustration of PVE and f. PTE mechanisms. Image reproduced from Ref. [95] with permission from American Chemical Society.

We further look into the spatially resolved scanning photocurrent images of the MoS_2 FET illuminated by 532, 785, and 1550 nm laser to investigate the photocurrent generation mechanisms. As shown in Figure 3.11, the edges of the metal electrodes are marked by black dashed lines, and the edges of the MoS_2 are marked by blue dashed lines. We extract a line profile of photocurrent intensities in each image along the green dashed line and present them in

Figure 3.11d. The photocurrent intensities were normalized for clarity. Gaussian fittings of the photocurrent are also presented at the junction region by solid curves. The strongest photocurrent responses are observed at the MoS_2-metal junction for all illumination wavelengths, indicating PVE contributes to the photocurrent generation. Potential barriers formed at MoS_2-metal junctions due to Fermi level alignment results in a built-in electric field. When incident photon energies are larger than the bandgap of MoS_2, this electric field will separate the photoexcited charge carriers.

When photon energy is below the bandgap, PVE induced photocurrent response is absent due to the lack of interband transitions. By comparing the photocurrent profiles and the Gaussian fittings, we notice strong photocurrent "tails" in the metal region (pointed by the black arrows), indicating the contribution of PTE (Figure 3.11f). A temperature difference (ΔT) between MoS_2 and metal electrodes leads to a photothermal voltage (V_{PTE}) across the junction, similar to the case in BP FET. We estimated the Seebeck coefficient of our MoS_2 device at different Fermi levels and obtained $S \sim 40\ \mu V/K$ at $V_g = 0$ V.

Polarization dependent photocurrent measurements were further performed to differentiate the relative contributions of different photocurrent generation mechanisms. As defined in Figure 3.10c, 0^o denotes the polarization direction along metal-MoS_2 contact edge. Laser wavelengths from 500 nm (2.48 eV) to 1050 nm (1.18 eV) were applied to investigate the photocurrent response systematically. As shown in Figure 3.12, the maximum photocurrent response was observed at 90^o light polarization when lasers with photon energies below the direct bandgap of MoS_2 (with wavelength of 750 nm or longer). Meanwhile, for excitation photon energy is above the direct bandgap of MoS_2 (with laser wavelength of 650 nm or shorter), maximum photocurrent is generated by photons polarized at around 0^o.

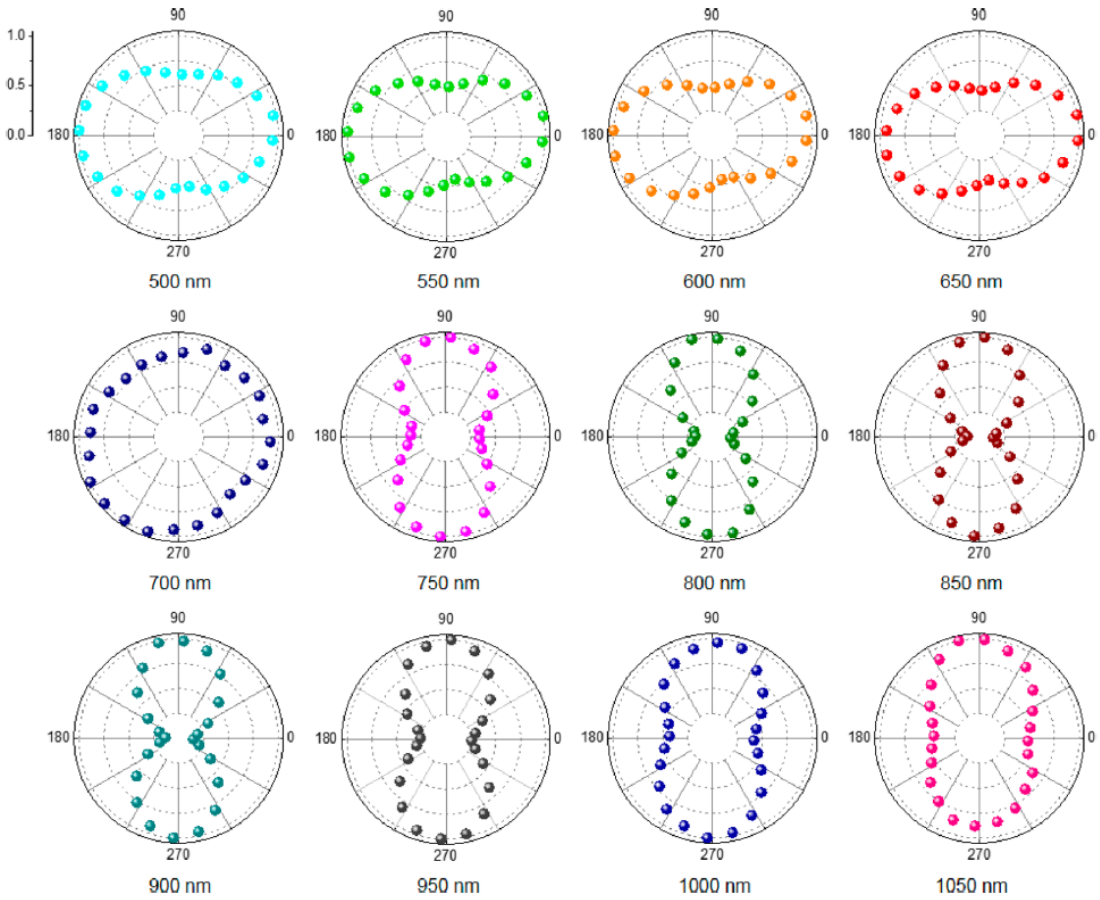

Figure 3.12 Polarization-dependent photocurrent responses at MoS_2-metal junction. Image reproduced from Ref. [95] with permission from American Chemical Society.

When the laser energy is above the direct bandgap of MoS_2, the polarization dependency is similar to the case in graphene. The built-in electrical field at MoS_2-metal junction separate electron-hole pairs generated in this region due to PVE. Previous reports of photocurrent measurements at graphene-metal junction suggested that the electrons in 2D material valence band preferably absorb photons with the polarization direction perpendicular to the momentum of electrons.[96] Therefore, at 0^o polarization direction, the photocurrent intensity is maximized due to increased number of charge carriers compared to 90^o laser polarization.

When the laser energy is below the direct bandgap of MoS_2, PVE is no longer a dominating factor, and PTE is independent of laser polarization. A new mechanism is needed to explain the photocurrent generation. As we mentioned before, the Schottky barrier between Au electrodes and few-layer MoS_2 is very small (~50 meV, Figure 3.9a). This barrier is well below the excitation photon energies in our experiments. Photoexcited hot electrons in metal electrodes can cross over the Schottky barrier and be injected into the conduction band of semiconductors (Figure 3.13a). The injection yield of hot electrons Y follows the Fowler equation,

$$Y \sim \frac{1}{8E_F}\frac{(\hbar\omega-\varphi_B)}{\hbar\omega} \qquad (3)$$

where φ_B is the Schottky barrier, and E_F is the Fermi energy. We take a look at the anisotropy ratio of the photocurrent under illumination of different wavelength (Figure 3.13b). When the illumination wavelength is close to 850 nm, the anisotropic ratio of the photocurrent response ($I_{PC}^{90^o}/I_{PC}^{0^o}$) achieves its maximum (~8). This ratio is significantly reduced when the metal electrode increase from 200 nm to 2 μm, indicating the photocurrent generation is related to electrode metal absorption I_{ab},

$$I_{pc} \sim I_{ab} \sim \langle S \rangle_{time} \sim |E|^2$$

where S is the time averaging Poynting vector. $|E|^2$ is calculated by finite difference time domain (FDTD) simulations (Figure 3.13c), showing a peak at ~850 nm. This peak is in good agreement with experimental data. Also, the electrode of 200 nm width shows higher resonance intensity compared to the 2 μm width electrode, consistent with the observations. Both PVE (650 nm) and surface plasmon (850 nm) induced photocurrent signals have a linear dependence with incident power (Figure 3.13d).

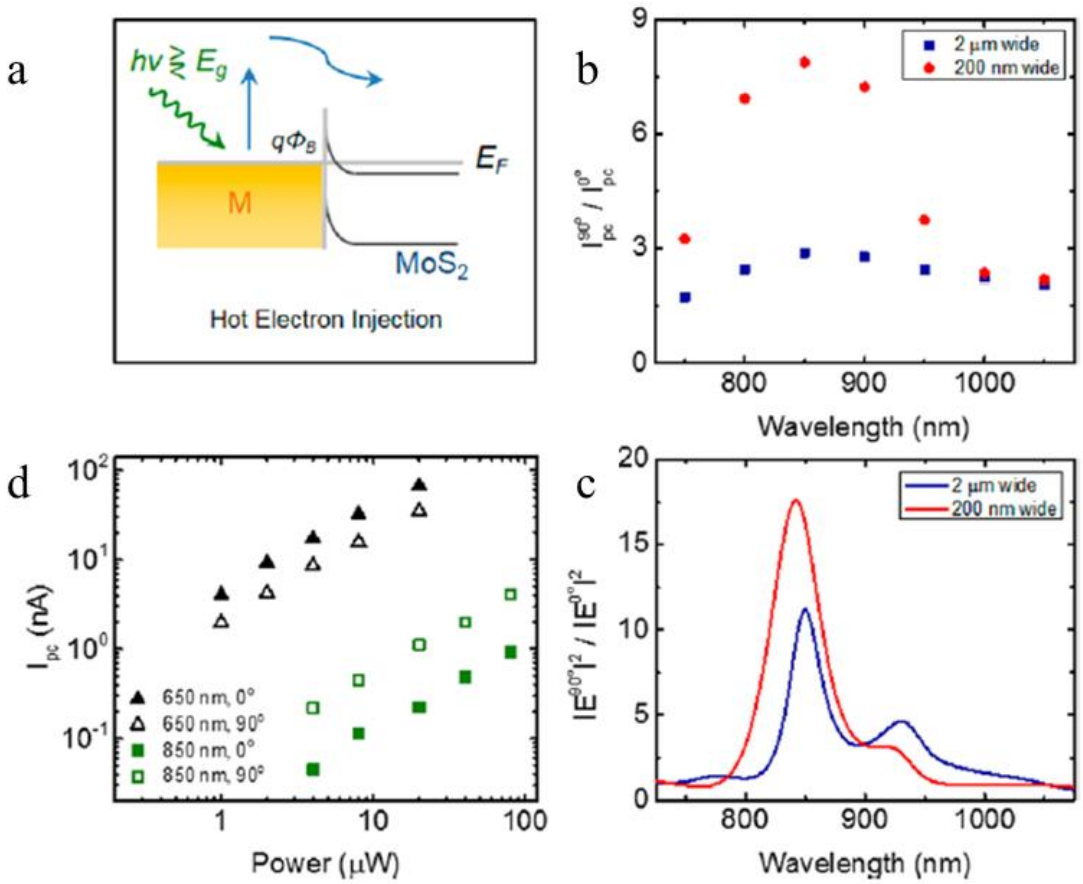

Figure 3.13 Hot electron injection. a. Schematic of hot electron injection from a metal electrode to MoS_2. b. The wavelength dependence of measured photocurrent response at MoS_2-metal junctions. c. FDTD simulation of absorption by metal electrodes. d. Photocurrent power dependence with 650 nm (1.91 eV, black triangles) and 850 nm (1.46 eV, green squares) laser polarized in 0^o (solid) and 90^o (hollow). Image reproduced from Ref. [95] with permission from American Chemical Society.

Chapter 4 Van der Waals heterostructures

4.1 Introduction to van der Waals heterostructures

With the rapid development of research on 2D materials, researchers have been paying more attention to van der Waals heterostructures. This structure is obtained by stacking 2D materials on top of each other in an arbitrary order, just like building with Lego. As shown in Figure 4.1, the result is an artificial material that follows a chosen order. In the 2D material plane, the stability is preserved by strong covalent bonds, whereas the interlayer force is van-der-Waals like and relatively weak.

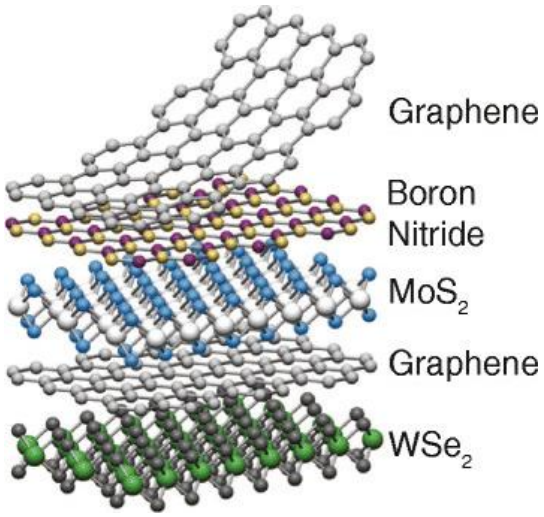

Figure 4.1 Structure of van der Waals heterostructures. Image reproduced from Ref. [1] with permission from Nature Publishing Group.

The heterostructures built by 2D materials is fundamentally different from conventional covalently bonded materials. The surface of 2D material lacks dangling bonds, allowing the creation of heterointerface with high quality. [97] Moreover, the strong light-matter interactions

and unique optoelectronic properties of TMDCs enable many new possibilities in the heterostructure optoelectronic devices, such as photodetectors, light-emitting diodes, and photovoltaics.[98-101] A series of 2D materials, with different bandgaps and work functions, provide numerous opportunities to design functional van der Waals heterostructures by engineering band alignment and electrostatically tune the charge carrier densities.[57] Table 4.1 summaries the common 2D materials that might be used to construct van der Waals heterostructures.

Table 4.1 2D Material Library

<table>
<tr><td>Graphene family</td><td>Graphene</td><td colspan="2">hBN
'white graphene'</td><td>BCN</td><td>Fluorographene</td><td>Graphene oxide</td></tr>
<tr><td rowspan="2">2D chalcogenIdes</td><td colspan="2" rowspan="2">MoS_2, WS_2, $MoSe_2$, WSe_2</td><td colspan="2" rowspan="2">Semiconducting dichalcogenides:
$MoTe_2$, WTe_2,
ZrS_2, $ZrSe_2$ and so on</td><td colspan="2">Metallic dichalcogenides:
$NbSe_2$, NbS_2, TaS_2, TiS_2, $NiSe_2$ and so on</td></tr>
<tr><td colspan="2">Layered semiconductors:
GaSe, GaTe, InSe, Bi_2Se_3 and so on</td></tr>
<tr><td rowspan="2">2D oxides</td><td>Micas, BSCCO</td><td colspan="2">MoO_3, WO_3</td><td colspan="2" rowspan="2">Perovskite-type:
$LaNb_2O_7$, $(Ca,Sr)_2Nb_3O_{10}$,
$Bi_4Ti_3O_{12}$, $Ca_2Ta_2TiO_{10}$ and so on</td><td>Hydroxides:
$Ni(OH)_2$, $Eu(OH)_2$ and so on</td></tr>
<tr><td>Layered Cu oxides</td><td colspan="2">TiO_2, MnO_2, V_2O_5,
TaO_3, RuO_2 and so on</td><td>Others</td></tr>
</table>

* Monolayers stable in air at room temperature are shaded blue. Those likely to be stable in air are shaded green. Those unstable in air but stable in inert atmosphere are shaded pink. Those shaded gray are available in monolayer form, but need further investigation. Table reproduced from Ref. [1] with permission from Nature Publishing Group.

4.2 Electrical properties of BP-MoS_2 p-n heterojunction

Black phosphorous (BP), as mentioned in the previous chapter, is an emerging candidate for novel electronic and optoelectronic applications. With a bandgap of 0.3 eV in bulk form and a thickness dependent direct bandgap ranging from 0.3 eV to 2 eV,[102] BP is especially suitable

for near-infrared applications. By stacking few-layered BP and MoS_2, a vertical p–n junction can be built to achieve a maximum photocurrent response of 418 mA W^{-1},[98] much larger than the photoresponsivity of photodetectors based on only BP or MoS_2.[103, 104]

We first fabricate BP-MoS_2 heterostructures. Both MoS_2 thin flakes and BP flakes were mechanically exfoliated from the bulk material. MoS_2 crystal was first exfoliated onto a degenerately doped 290 nm SiO_2/Si substrate, while BP crystal was exfoliated onto a PDMS stamp. Next, a selected BP thin flake on the PDMS stamp was placed on top of a selected MoS_2 flake on the SiO2/Si substrate, forming a BP–MoS_2 heterojunction. Finally, the metal electrodes were defined by electron beam lithography and the subsequent deposition of 5 nm Ti and 40 nm Au. Figure 4.2a shows the schematic illustration of a BP–MoS_2 junction device and its optical image in the inset. The thickness of the MoS_2 and BP layers are 4.8 nm and 10.0 nm, respectively, as determined by atomic force microscopy. The structure of MoS_2 and puckered BP layers are shown in Figure 4.2b. We measure the electrical properties of the heterojunction in high vacuum ($\sim 10^{-6}$ Torr). A gate voltage V_g was applied to the Si substrate to electrostatically adjust the carrier concentration in both materials. Figure 4.2c presents the gate-dependent transport characteristics of the MoS_2 and BP layer, respectively. The semilog plot is presented in the inset. MoS_2 and BP flakes display n-type and p-type characteristics at zero gate bias, creating a p–n junction in the overlap region. The mobility of MoS_2 and BP are estimated to be $\sim$43 cm^2 V^{-1} s^{-1} and $\sim$38 cm^2 V^{-1} s^{-1}, respectively. Figure 4.2d displays the I–V characteristics of the BP–MoS_2 junction measured between electrodes E2 and E3. The unintentional doping at zero gate bias allows for strong rectification of drain current, consistent with the gate-tunable transport curves. When the carrier concentrations in the junction region are electrostatically modified by applying a gate voltage, this rectification ratio reduces. The electronic tunability of

vertical p–n heterostructures is likely to be attributed to tunneling-assisted interlayer recombination due to the absence of a depletion region.[57]

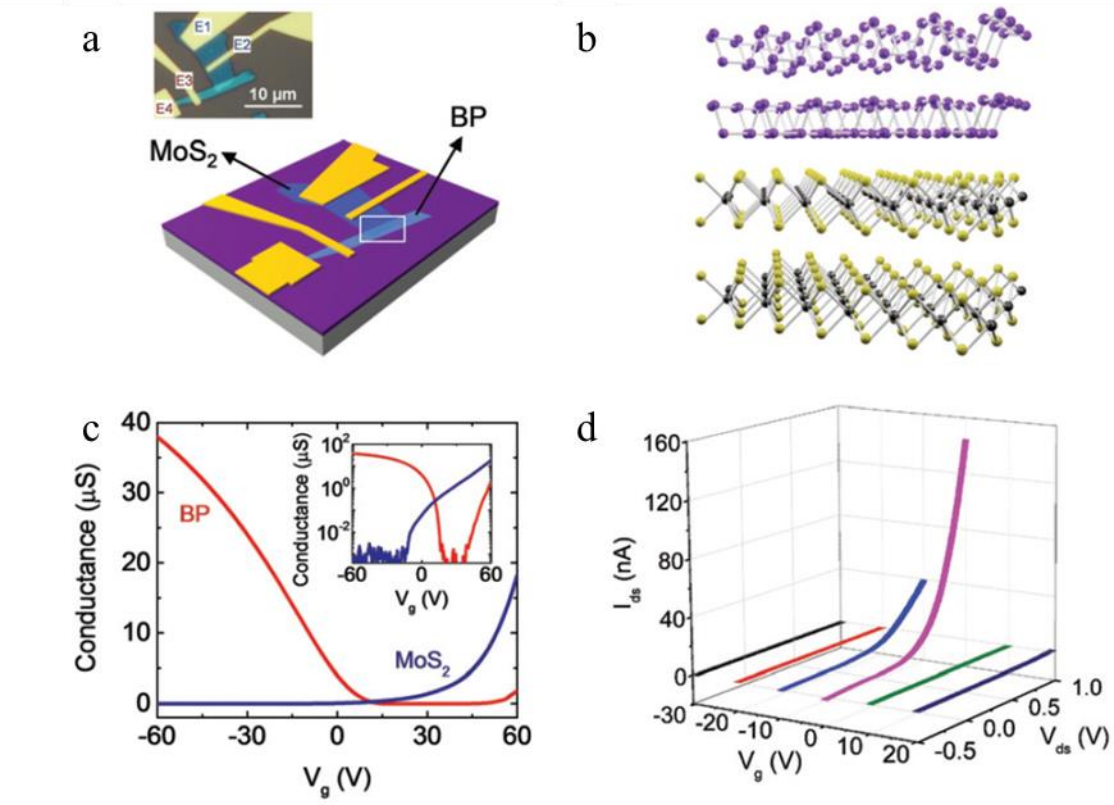

Figure 4.2 Electrical property of BP-MoS_2 p-n heterojunction. a. Schematic of BP-MoS_2 p-n heterojunction with its optical image in the inset. b. Structure of the heterojunction area. c. Gate-dependent transport characteristics for BP (red curve, measured between E3 and E4) and MoS_2 (blue curve, measured between E1 and E2). d. I–V curves at various gate voltages measured between E2 and E3. Image reproduced from Ref. [101] with permission from The Royal Society of Chemistry.

4.3 Optoelectronic properties of BP-MoS_2 p-n heterojunction

To evaluate the performance of the BP-MoS_2 p-n heterojunction as a photodetector, a diffraction-limited 532 nm (2.33 eV) laser spot was focused onto the p–n junction area under a drain bias. The size of the laser spot is around 1 μm, much smaller than the BP–MoS_2 junction.

The photon energy of the 532 nm laser is above the direct bandgap of both few-layered MoS_2 (~1.9 eV) and BP (0.3 eV), which can offer high efficiency of photocurrent generation.[95, 105] Figure 4.3a shows the I–V characteristics of the p–n junction in the dark state (black curve) and under various laser illumination powers in the reverse bias region at $V_g = 0$ V. The photocurrent I_{pc} is defined as $I_{illumination} - I_{dark}$. The photocurrent at the p–n junction strongly depends on both drain bias and incident laser power. The highest photoresponsivity is ~170 mA W^{-1} at $V_{ds} = -2$ V and 30 μW incident laser power, comparable to the photoresponsivity in a previous report at a BP–MoS_2 p–n junction using monolayer MoS_2.[98] This photoresponsivity is nearly 40 times higher than the reported BP phototransistors.[106] At a reverse drain bias, I_{pc} has a superlinear relationship with increasing laser power, possibly due to the nonequilibrium occupancy of intragap recombination centers at low laser powers.[107]

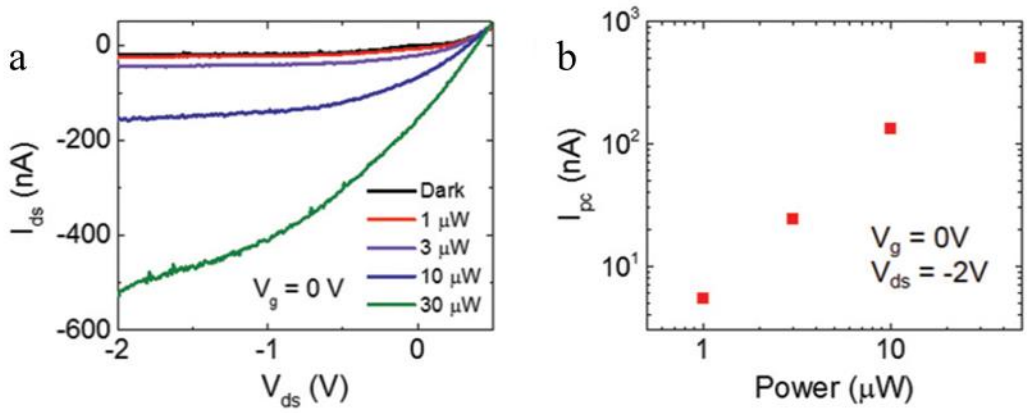

Figure 4.3 Performance of BP-MoS_2 p-n heterojunction as a photodetector. a. I–V characteristics of the BP–MoS_2 p–n junction in the dark state and under 532 nm laser illumination. b. Power dependence of photocurrent intensities in the junction region. Image reproduced from Ref. [101] with permission from The Royal Society of Chemistry.

To investigate the photocurrent generation mechanism, scanning photocurrent microscopy was applied to obtain spatially-resolved photocurrent mapping of the BP–MoS_2 device. As shown in the reflection image (Figure 4.4a), the edges of the electrodes are marked by grey dashed lines while the BP and MoS_2 crystals are marked by blue and purple dashed lines. At zero gate bias, a p–n junction is formed at the BP–MoS_2 heterostructure, leading to strong electron–hole pair separation and remarkable photocurrent at the junction (Figure 4.4b). This strong photocurrent can be suppressed by modulating the electrostatic gating in either the positive or negative direction (Figure 4.4c). When gate voltage is applied, the interlayer recombination rate will increase due to the accumulation of one type of majority carriers,[108] resulting in a reduction of photocurrent signals. Also, electrostatic gating can modulate the built-in electric field at the MoS_2–BP interface, thus changing the photocurrent intensities.

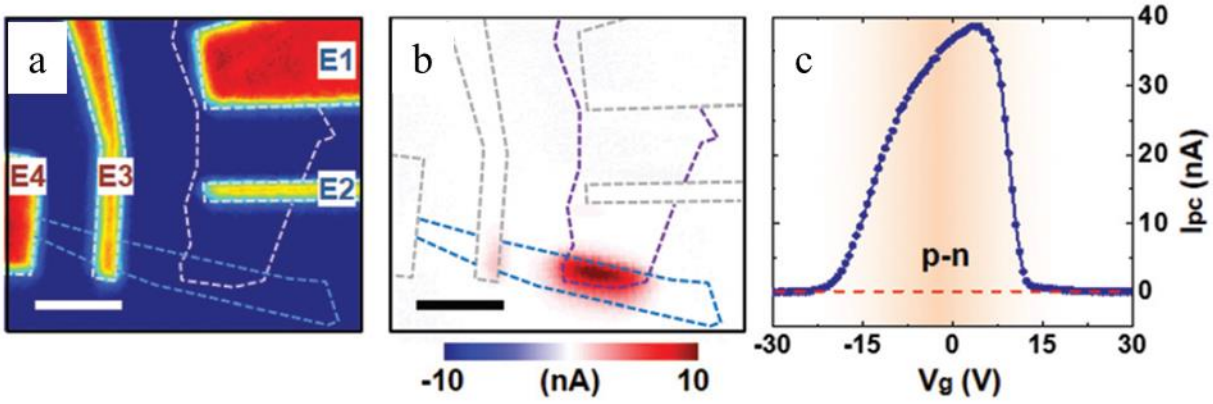

Figure 4.4 Scanning photocurrent microscopy of the BP–MoS_2 heterostructure. a. Reflection image and b photocurrent image. c. Photocurrent intensity as a function of gate voltage. Image reproduced from Ref. [101] with permission from The Royal Society of Chemistry.

The relative contributions of different photocurrent generation mechanisms are further investigated by polarization-dependent photocurrent measurements at the BP–MoS_2 p–n

junction. We used linearly-polarized laser with different wavelengths. The polarization direction of the laser is defined as shown in Figure 4.5a, where 0° and 90° denote the directions parallel to the edge of metal electrodes at the MoS_2 and BP sides, respectively. Figure 4.5b shows the photocurrent polarization dependence of BP–MoS_2 p–n heterojunction when excited by 532 nm laser. The maximum photocurrent signals are obtained when the laser polarization direction is perpendicular to the MoS_2 channel or nearly along the edge of electrodes on the MoS_2 side (−30°). Compared to the photocurrent signals at the junction region, the photocurrent response at the metal contacts can hardly be identified. In contrast, with 1550 nm laser illumination, the photocurrent response shows an altered signature. The photocurrent signals maximize when the laser polarization direction is perpendicular to the electrode edges on the MoS_2 side (90°) or parallel to the electrode edges on the BP side (Figure 4.5c and d). We perform Raman spectroscopy to determine the intrinsic orientation of the BP flake.[109] The x direction of the BP flake is at about 30°, suggesting that the anisotropy of BP flake absorption is not a dominating factor to the polarization-dependent photocurrent generation at the junction.

We attribute the photocurrent response at the junction upon 532nm and 1550 nm laser illumination to different photocurrent generation mechanisms. Figure 4.5g illustrates the band diagram of the BP–MoS_2 junction when excited by a 532 nm (2.33 eV) laser. The electrons in the valence bands of both MoS_2 and BP are excited to their conduction bands, respectively. Due to Fermi level alignment, a type-II heterostructure is formed [57] where the valence band maximum of MoS_2 much lower than that of BP. The valence band offset between BP and MoS_2 is much larger than the conduction band offset at $V_g = 0$. Both photogenerated electron–hole pair dissociation and tunneling mediated interlayer recombination between majority carriers at the bottom (top) of the conduction (valence) band of MoS_2 (BP) are expected to contribute to the

photocurrent generation at the BP–MoS_2 junction. We realize that the recombination induced photocurrent response has an opposite photocurrent polarity in the junction region compared to the measured photocurrent signals. Therefore, photogenerated electron–hole pair dissociation is dominant. Photogenerated electron–hole pair can be separated by two pathways at the BP–MoS_2 junction: (1) photogenerated holes in MoS_2 drift to BP because the valence band maximum of MoS_2 is much lower than that of BP, and (2) photogenerated electrons flow either from BP to MoS_2 or from MoS_2 to BP depending on the structure of the conduction band offset.

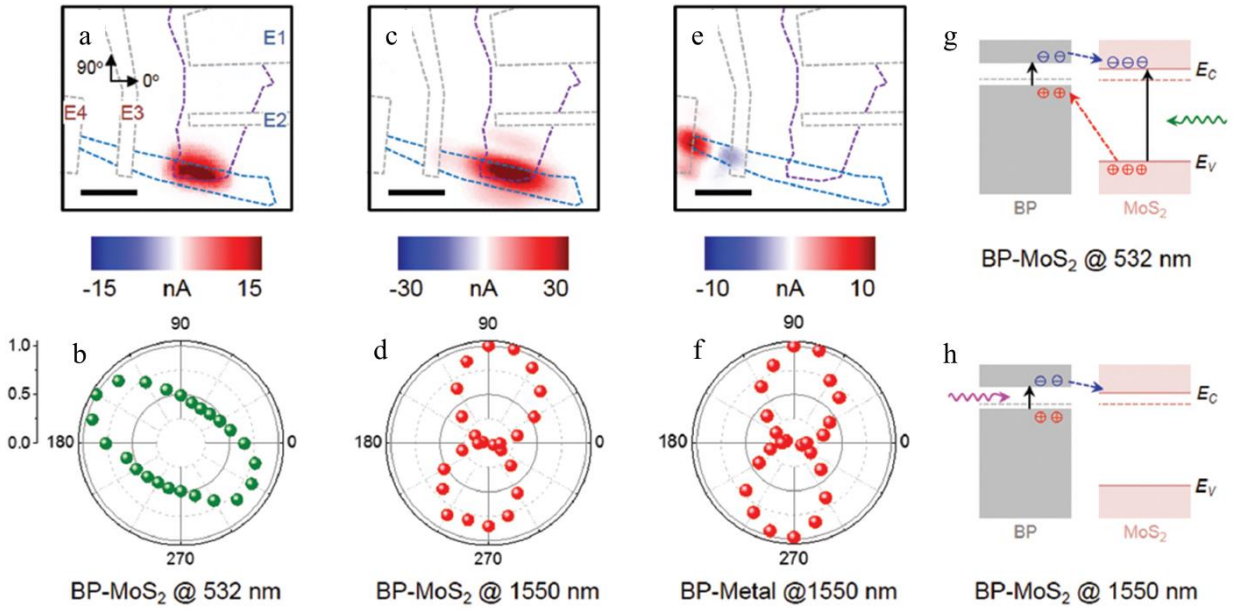

Figure 4.5 Polarization-dependent photocurrent microscopy of the BP–MoS_2 heterostructure. a. Photocurrent images at the junction illuminated by 532 nm laser and c 1550 nm laser. The directions of 0° and 90° are defined as marked in the image. b. Normalized photocurrent intensities in the BP–MoS_2 p–n junction area when illuminated with linearly-polarized 532 nm and d 1550 nm laser. e. Photocurrent image and f normalized photocurrent intensity at the BP–metal junction. g. Schematic diagrams show photocurrent generation mechanisms when the junction is excited by 532 nm laser and h. 1550 nm laser, respectively. The scale bars are 4 μm. Image reproduced from Ref. [101] with permission from The Royal Society of Chemistry.

The photocurrent generation at the junction area is a competitive effect between these two pathways. In this particular device, the first pathway is dominant under the illumination of 532 nm laser. Photogenerated holes in MoS_2 valence band can flow into BP due to a large band offset across the sharp vertical interface, resulting in a strong photocurrent response. This expectation is confirmed by the polarization-dependent photocurrent measurements, where the photocurrent response at the MoS_2–BP junction is polarized to the direction perpendicular to the MoS_2 channel, which is similar to the photocurrent response at MoS_2–metal junctions as we discussed in the previous chapter. The maximum photocurrent signals were observed when light is polarized perpendicularly to the MoS_2 channel at 532 nm illumination due to the photovoltaic effect.[95]

When illuminated by 1550 nm (0.8 eV) laser, the photon energy is insufficient to excite electrons in MoS_2 from its valence band to conduction band. Therefore, photocurrent signals primarily result from the direct bandgap transitions in BP. Thus, the second pathway becomes important (Figure 4.5h). The maximum photocurrent response occurs when the incident light is polarized along the direction of electrode edges at the BP side (90°). This result follows the polarization dependence of photocurrent response at the BP–metal junctions (Figure 4.5e and f), further confirming that the photocurrent response at the BP–MoS_2 junction primarily results from the photogenerated electrons in BP. All the devices we tested display the same polarization dependency in the junction area under 1550 nm illumination. Note that photothermoelectric effect may also contribute to the photocurrent generation, but is only expected to play a negligible role.[57] The direction-dependent absorption of BP is another issue to consider.[109] However, in our experiments, the polarization directions that generate the maximum photocurrent signals in the junction region are different under 532 nm and 1550 nm illumination,

whereas the BP crystal axis orientation remains the same, suggesting the intrinsic absorption of BP is not likely a dominant factor that determines the photocurrent polarization dependence at the MoS_2–BP heterojunction.

Chapter 5 CNTs for image-guided drug delivery

In the first half of this dissertation, we discussed the optoelectronic properties and applications of low-dimensional materials. In the second half, we will discuss the bioelectronics of these materials.

Various nanomaterials have been demonstrated to effectively delivery bioactive drugs or cargo into living systems for diagnosis or therapy.[110, 111] Among them, CNTs have attracted particular attention due to its unique physical, chemical, electrical, and optical properties[4, 5] as well as its high efficiency in transporting a wide range of molecules across membranes into living cells.[112, 113] CNTs not only serve as drug delivery vehicles, but also as contrast agents for a variety of imaging methods. CNTs have been successfully applied in MRI, a medical imaging technique that provides great spatial resolution anatomical images with the ability to extract additional functional information, both *in vitro* and *in vivo*.[114-116] Due to its intrinsic near-infrared fluorescence (NIRF),[8, 117-120] CNTs themselves can be utilized for fluorescence imaging. In addition, CNTs can absorb near infrared light, which make them idea candidates for OCT, an optical imaging technique that provides structural information at high resolution (~1-10 μm) with deep optical image penetration (1–3 mm). [121] It is, therefore, desirable to develop a CNT based drug delivery system, whose treatment effect can be simultaneously monitored by various types of medical imaging tools.

5.1 Functionalization of CNTs

CNTs are hydrophobic materials. For biomedical applications, it is necessary to functionalize CNTs so that they can be suspended in an aqueous media. Various ionic surfactants

and nonionic polymers were used to suspend as-grown CNTs via a method adapted from a previous report.[122] The various surfactants and polymers used for functionalization can be sorted into two categories. The first is ionic small molecules, such as sodium cholate, sodium dodecylbenzenesulfonate (SDBS), and sodium dodecyl sulfate (SDS), which cover CNTs with a micelle structure that prevents nanotube aggregation by charge repulsion (Figure 5.1a top).[123] The second is nonionic polymers, including PL-PEG, PEG-PPG-PEG Pluronic F-108 (PF108), and PEG-PPG-PEG Pluronic F-68 (PF68), which suspend nanotubes by stacking and wrapping around CNT sidewalls (Figure 5.1a bottom).

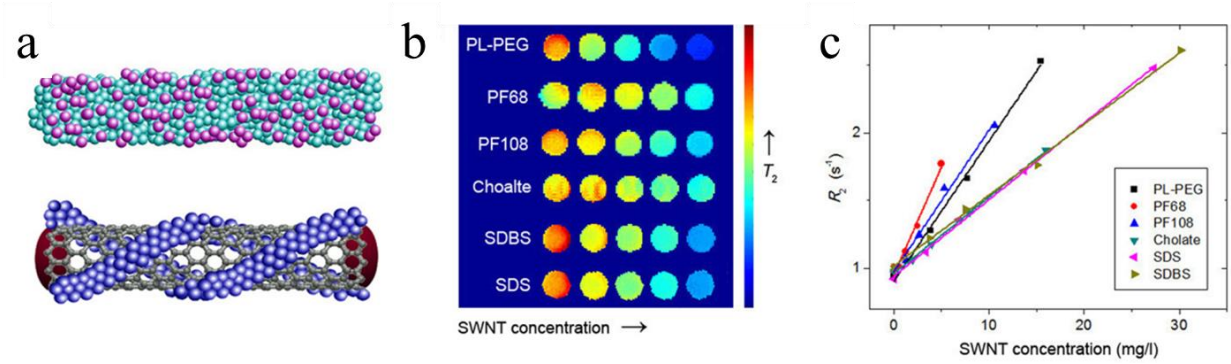

Figure 5.1 T_2-weighed MRI of CNTs. a. Schematic diagram of CNTs functionalized by ionic surfactants (top), which form a micelle structure, and by nonionic polymers (bottom), which wrap around nanotubes to form a suspension. b. MRI T_2 map and c. T_2 relaxivity fitting for CNTs functionalized by different surfactants or polymers with various CNT concentrations. Image reproduced from Ref. [124] with permission from American Chemical Society.

Surface functionalization can affect the efficiency of CNTs as imaging contrast agents. It is well known that CNTs functionalized by ionic surfactants display stronger NIRF than those functionalized by nonionic polymers.[123] However, the effect of CNT surface functionalization on their MRI efficiency has not been reported. Here, we investigate the influence of CNT surface functionalization on their performance in T_2-weighted MRI. In this experiment, each CNT

sample was prepared with series dilution and imaged in NMR tubes (Figure 5.1b). T_2 relaxivity is related to the spin−spin relaxation efficiency of an MRI contrast agents. Image contrast increases with increasing T_2 relaxivity due to better interactions between contrast agents and nearby water protons. T_2 relaxivity, and the slopes of their linear fitting versus CNT concentration, or r_2, were also calculated (Figure 5.1c). The r_2 for micelle-encased CNTs was around 0.05− 0.06 s^{-1} $(mg/L)^{-1}$; polymer-suspended nanotubes exhibited r_2 higher than 0.10 s^{-1} $(mg/L)^{-1}$ with PF68 yielding the highest r_2 at 0.16 s^{-1} $(mg/L)^{-1}$.

As reported in previous literature, T_2-shortening properties of CNTs are mainly attributed to iron catalysts attached to the ends of nanotubes. [114-116]. It is clear that the distinct r_2 of nanotubes functionalized by the two types of suspension agents are not caused by different iron concentrations. The r_2 difference is likely due to varying amounts of water protons with access to the iron nanoparticles attached to the nanotubes; this would thus impact proton spin dephasing. For micelle-encased CNTs, small ionic surfactants thoroughly cover the nanotubes, including the two ends where iron catalysts are attached; therefore, water molecules have limited access to the iron catalysts.[122] In contrast, polymers suspend CNTs by helical wrapping via π−π stacking and hydrophobic forces,[125] allowing more space for water to directly approach the nanotube and hence shorten the spin dephasing time. It is thus clear that r_2 of the CNT suspension is influenced by not only the amount of iron catalysts present but also the interactions between the iron catalysts and the water environment, which varies for different surface functionalization.

Ionic surfactants and nonionic polymers display very distinct effects on the optical and magnetic properties of CNTs in aqueous media. Ionic surfactants suspended CNTs have bright NIRF, whereas nonionic polymer functionalized CNTs exhibit higher r_2 for MRI. It is therefore critical to address how functional groups competitively interact with CNTs and affect their

performance in dual-modality imaging. Here, CNTs were initially functionalized by ionic surfactants to achieve high NIRF quantum yield and nonionic polymers were gradually introduced to enhance their T_2 relaxation efficiency. This process was performed by adding 1 mg/mL PL-PEG into a sodium cholate-functionalized CNT suspension, which was then dialyzed to remove sodium cholate in the suspension. In our experiment, the CNT suspension was removed after 8 h, 1 day, 2 days, and 4 days of dialysis and immediately centrifuged to remove extra bundles that formed during dialysis. Absorption spectra of the samples were obtained and investigated. Two of the sharp E_{11} absorption peaks at a wavelength of about 1000 nm were measured and plotted in Figure 5.2a. Remarkable differences were observed among different

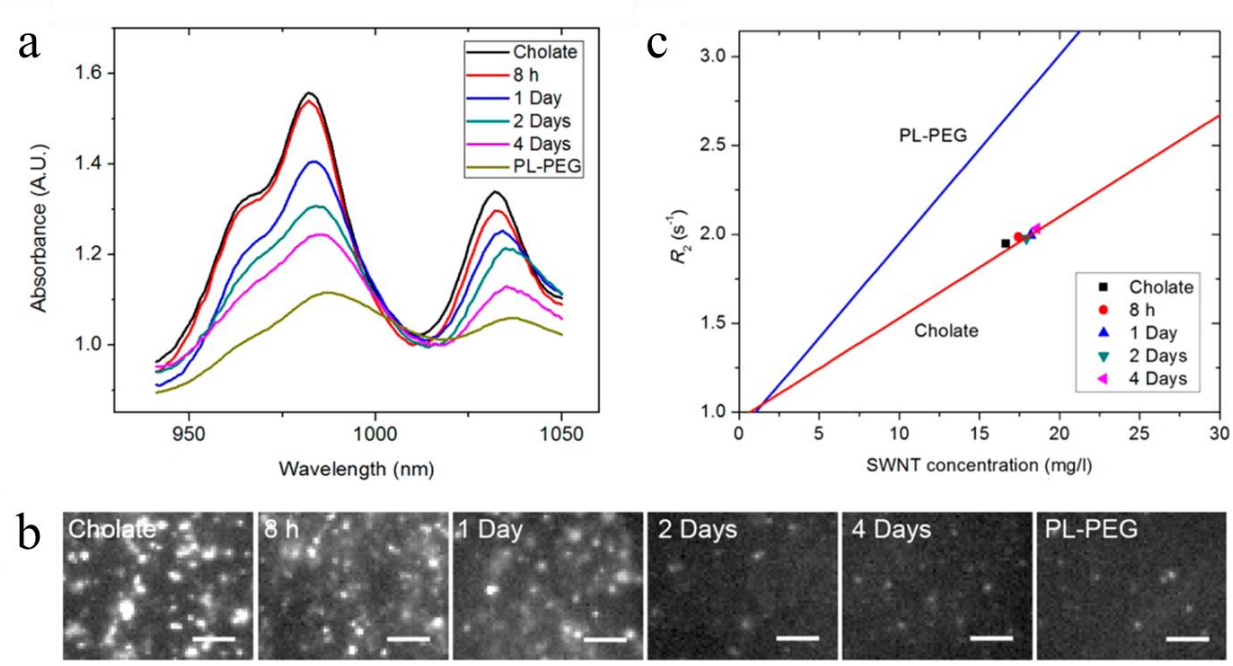

Figure 5.2 Competitive surface functionalization between surfactants and polymers. a. Absorption spectra of selected peaks showing intensity and position change during surfactant/polymer dialysis. b. NIRF intensity change in thin films. After 4 days of dialysis, the fluorescence intensity is close to PL-PEG-CNTs. c. T_2 relaxivity (R_2) of CNT samples. The red line and blue line are the linear fitting of sodium cholate and PL-PEG-CNTs, respectively. Image reproduced from Ref. [124] with permission from American Chemical Society.

samples. The original sharp absorption peaks seen in the cholate suspended CNTs became broadened and red-shifted toward the peak of PL-PEG functionalized CNTs (PL-PEG-CNTs). The broadened and red-shifted peaks indicate that PL-PEG polymer molecules gradually wrapped around the CNTs while small bundles were forming.

NIRF of CNTs after dialysis was measured in the 1150-1700 nm range on a liquid-nitrogen cooled InGaAs camera. A step-by-step change in emission was clearly observed during the dialysis process (Figure 5.2b). The emission became weaker with increased dialysis time, corresponding to a NIRF quantum yield drop for the nanotubes. Nevertheless, the CNT suspensions still had a reasonable fluorescence quantum yield.

After the 4 day dialysis, the NIRF signal of two-step functionalized CNTs became close to that of PL-PEG-CNTs. Despite the gradual change in NIRF during dialysis, the r_2 of each sample unexpectedly showed almost identical values (Figure 5.2c). Linear fitting revealed that after dialysis, the r_2 of CNTs was almost identical to that of micelle-encased nanotubes and was distinct from that of PL-PEG-CNTs. This may indicate that nanotube surfaces were still thoroughly covered by micelle structures of ionic molecules, shielding the iron catalysts from water protons. The binding force between ionic surfactants and nanotubes is stronger than that between nonionic polymers and nanotubes. Therefore, PL-PEGs may only wrap around the sodium cholate coating rather than replacing it. The reduction of NIRF quantum yield of two-step functionalized CNTs may largely result from the formation of nanotube bundles, which is typical for PL-PEG-CNTs.

5.2 Multi-modality imaging of CNTs

Proper surface functionalization of CNTs is critical for their biomedical applications. Therefore, PL-PEG was chosen to functionalize CNTs since it not only provides descent fluorescence and MRI imaging contrast, but also displays high biocompatibility. We further investigate the ability of CNTs for multi-modality image. After functionalization, the optical extinction spectrum of the CNT sample was acquired with a spectrophotometer (Cary 5000) from 400 to 1350 nm, as shown in Figure 5.3a. Spectrophotometry indicated broadband visible and NIR attenuation with sharp localized peaks, indicating CNTs were well dispersed and not aggregated in solution.[122]

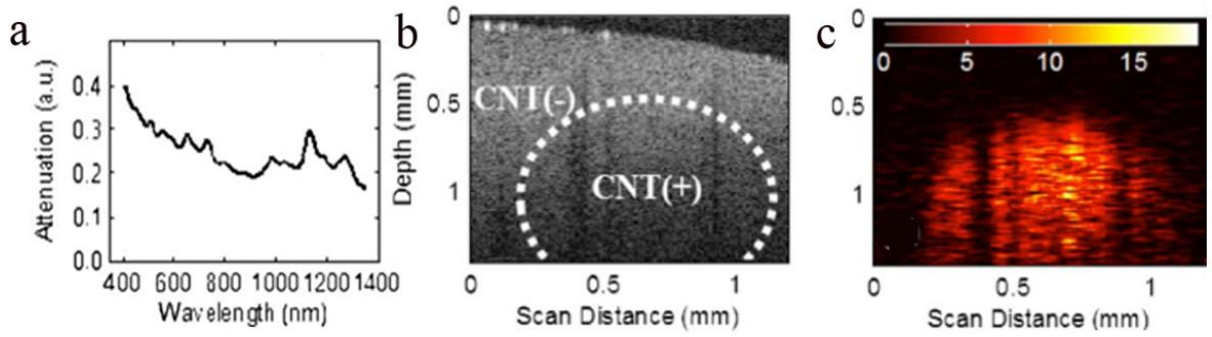

Figure 5.3 CNT characterization for OCT. a. Visible–NIR attenuation spectrum of CNTs. b. OCT magnitude image of three-dimensional agarose phantom; note a lack of contrast or any visual confirmation of the presence of CNTs. CNT (+) (~84 nM) and CNT (-) regions are highlighted. c. Photothermal OCT of the same field of view, revealing the cylindrical CNT gel inclusion. Photothermal signal is in arbitrary units. Image reproduced from Ref. [121].

For photothermal imaging, a commercial OCT system (Bioptigen, Inc.) was altered. The imaging system contained an 860 nm center wavelength, 51 nm bandwidth, superluminescent diode source (axial resolution ~6.4 μm in air), with 8.5 μm lateral resolution and 100 μs integration time. A titanium sapphire laser served as the photo- thermal beam, which was fiber

coupled and integrated with the OCT system via a 50/50 fiber coupler. The photothermal beam was tuned to 750 nm and amplitude modulated with a 50% duty cycle square wave at 100 Hz with a mechanical chopper, with 10 mW of power on the sample. OCT and photothermal spot sizes were roughly equal. One thousand consecutive temporal scans were acquired for each A-scan during photothermal beam amplitude modulation. 2D images of solid phantoms were acquired. Low gelling temperature agarose was mixed with either water as a negative control or CNTs to create 2% agarose gels with either 0 or 84 nM nanotube concentrations. The phantom was imaged with photothermal OCT using the system. Phantom images (Figure 5.3b and c) confirmed both the capabilities and limitations of each imaging modality. Photothermal imaging was able to discriminate the agarose/CNT cylinder from the scattering agarose background, while the OCT magnitude image could not.

NIRF and MRI of CNTs in live cells are also demonstrated in primary cultures from rodent brains. Mammalian brain cells, mainly neurons and glial cells, were prepared as described in previous literature.[126] For MRI, PL-PEG-CNTs were added into the culture medium at a concentration of 3.56 mg/L and incubated for 24 h. We did not observe any morphology change in the cells treated with PL-PEG-CNTs. Equivalent amount of solvent without CNTs was used as a sham control. The cells treated with or without the CNTs were then washed with phosphate buffered saline and mixed with agarose gel to form a semisolid cell solution. The cell-containing solution was transferred to a 96-well plate and imaged using a 4.7 T MRI scanner as described before. The final T_2 map is shown in Figure 5.4a, and a region of interest was manually drawn to calculate the relaxivity of each sample. The T_2 relaxivity of cells treated with CNTs was 5.06 s^{-1}, higher than that of the sham control (4.76 s^{-1}).

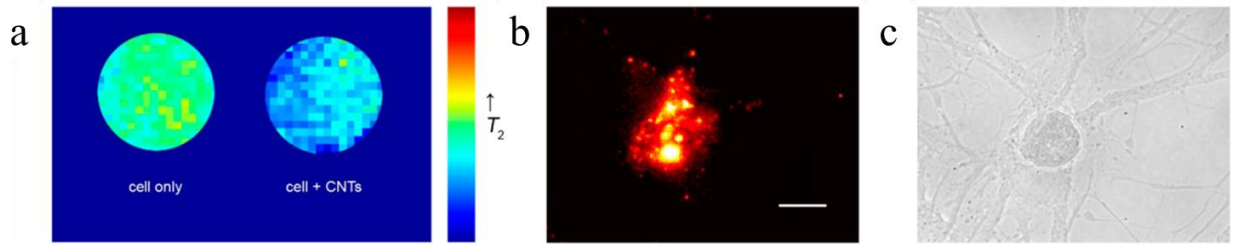

Figure 5.4 Live cell imaging of CNTs. a. MRI T_2 map of brain cells with or without the PL-PEG-CNT treatment. b. NIRF image and c. Optical image of brain cells incubated with a PL-PEG-CNT added culture medium for 72 h. The NIRF image of cells was coded with false color and the scale bar is 30 μm. Image reproduced from Ref. [124] with permission from American Chemical Society.

For NIRF imaging, cells were incubated with the PL-PEG-CNTs added culture medium for 72 h and fixed by 4% paraformaldehyde. The CNT fluorescence was measured on the InGaAs camera setup. Several images along the z-axis were overlapped to decrease noise levels and to reveal a more comprehensive CNT uptake profile (Figure 5.4b). Many fluorescent puncta residing in the brain cells can be observed. The sizes of those puncta are limited by the resolution of the detector (1 μm, much bigger than CNTs). Moreover, CNT fluorescence ranging from 1150 to 1700 nm is not absorbed by biomolecules and is easily distinguished from the autofluorescence of biological samples, making it ideal for deep tissue or even whole animal imaging.[127-129] The NIRF of CNTs may therefore be employed to investigate CNT uptake or labeling in intact brain.

5.3 CNTs for drug delivery

After demonstrating the ability of CNTs for OCT, MRI, and NIRF imaging, we further apply CNTs for medical applications both *in vitro* and *in vivo*. We demonstrate that CNT-mediated siRNA (CNT-siRNA) delivery system significantly silences our target of interest, gastrin-releasing peptide receptor (GRP-R), in neuroblastoma. CNT-siGRP-R resulted in a 50%

silencing efficiency and a sustained efficacy of 9 days for one-time siRNA treatment, whereas siRNA delivered by the commercial transfection reagent couldn't knockdown GRP-R expression.

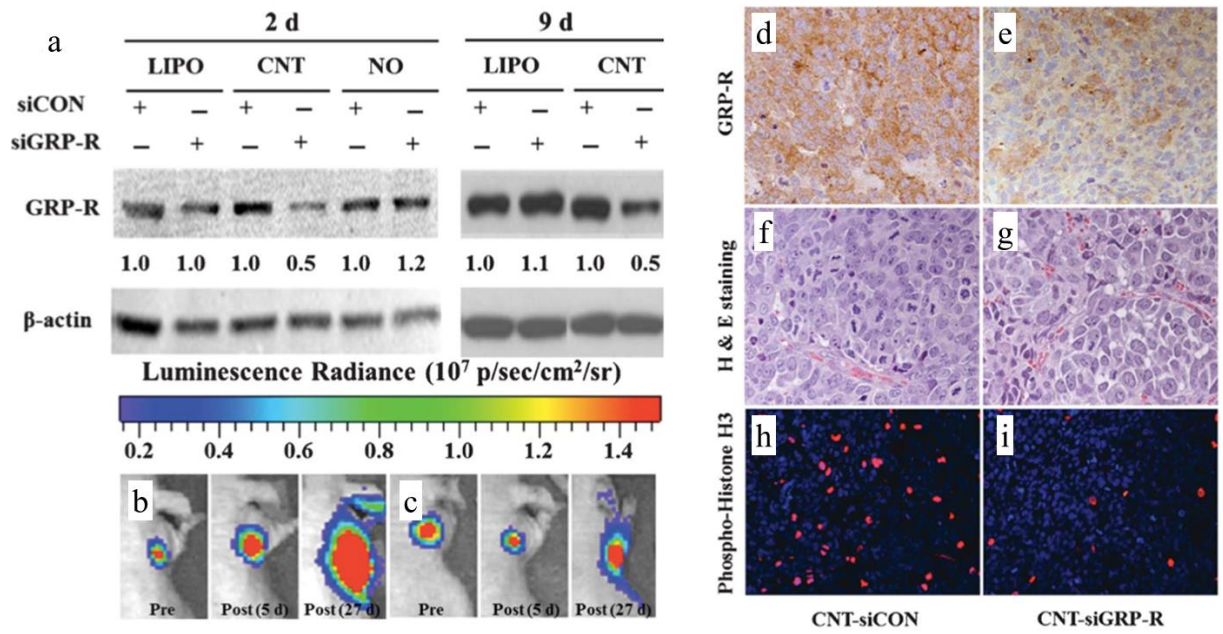

Figure 5.5 CNT-mediated GRP-R silencing in neuroblastoma *in vitro* and *in vivo*. a. BE(2)-C cells were treated with LIPO-siRNA, CNT-siRNA, and naked-siRNA for 2 and 9 days, respectively. Protein expression was detected by Western blotting. GRP-R expression was significantly silenced by CNT-siGRP-R, when compared to commercial transfection reagent LIPO and naked-siRNA. Relative levels of GRP-R were calculated by densitometry and listed below each band. b-Actin was used as a loading control. b. c. CNT-siRNA was injected locally into BE(2)-C subcutaneous xenografts. Bioluminescence images were taken for mice treated with CNT-siCON or CNT-siGRP-R; CNT-siGRP-R significantly reduced the tumor size and inhibited the tumor growth. d. e. Representative immunohistochemical staining of GRP-R in tumors treated with CNT-siCON or CNT-siGRP-R. The expression of target GRP-R (brown staining) was significantly decreased in CNT-siGRP-R treated tumor sections. f. g. Representative H&E-stained tumor sections from mice treated with CNT-siCON or CNT-siGRP-R. h. i. Paraffin embedded sections were stained with anti-human phospho-Histone H3 (Ser10) antibody followed by Alexa Fluor 568 Dye (Red). DAPI (49,6-diamidino-2-phenylindole, dihydrochloride, blue) was used for staining nuclei. Image reproduced from Ref. [130] with permission from American Chemical Society.

We also examined the drug delivery efficiency of CNT-siRNA in human neuroblastoma BE(2)-C cells. We transfected BE(2)-C cells with LIPO-mediated siCON (LIPO-siCON), LIPO-siGRP-R, CNT-siCON, CNT-siGRP- R, naked-siCON and naked-siGRP-R, respectively. As shown in Figure 5.5a, CNT-siGRP-R significantly down-regulated GRP-R expression 2 days after transfection, whereas both naked-siGRP-R and commercial transfection reagent LIPO-siGRP-R did not knock- down GRP-R expression. Moreover, the GRP-R silencing efficiency mediated by CNT-siRNA was persistently high at 9 days post-transfection, when most siRNA delivery systems cannot silence target genes for that duration due to the instability of siRNA.

To evaluate the efficacy of GRP-R silencing mediated by CNT-siRNA *in vivo*, we performed CNT-siRNA delivery locally into subcutaneous tumors. Mice were imaged before, 5 and 27 days after a single administration of CNT-siRNA. Injection of these two siRNA drugs produced significant effects on the tumor sizes in vivo (Figure 5.5b, c).

CNT-siGRP-R efficiently decreased the tumor size 5 days post-injection and significantly inhibited the tumor growth 27 days post-injection as compared to controls treated with CNT-siCON. To validate whether the GRP-R expression was affected in the tumors by CNT-siGRP-R treatment, immunohistochemistry (IHC) was performed. The expression of target GRP-R protein levels was significantly decreased in CNT-siGRP-R treated tumors (Figure 5.5e) compared to CNT-siCON controls (Figure 5.5d), which was consistent with our in vitro results. Moreover, we found that cells in CNT- siGRP-R treated tumors appeared to lose cell–cell adhesion, and were more differentiated on morphological observation (Figure 5.5g). As shown in Figure 5.5h and 5.5i, there was 70% less mitotic cells in the CNT- siGRP-R treated tumors than in the CNT-siCON treated one. It is obvious that CNT-siGRP-R treatments significantly reduced tumor cell proliferation and thus inhibited tumor growth.

Chapter 6 Carbon nanotube bioelectronics

Understanding the biological world at the single-molecule level is an essential part for us to understand our mother nature. However, the current single-molecule technologies are mostly complicated and time-consuming. For example, the sequencing of DNA requires polymerase chain reaction (PCR), a complicated process that involves purifying and amplifying the samples, labeling them with fluorescent dyes, and obtaining signals from large amount of samples. Moreover, the sizes of many biomolecules are very small. For example, the diameter of a DNA molecule is 2 nm, and proteins are typically 10 nm in size. Traditional methods (generally optical technique) are not able to process these small molecules with high precision and efficiency.

Carbon nanotubes, on the other hand, are promising candidates for bioelectronics. First, they are small in size. Single-walled carbon nanotubes (SWNT) have a typical diameter of 1-2 nm, comparable to that of the diameter of a DNA. Second, they have remarkable electronic and optoelectronic properties. They can be either metallic or semiconducting depending on chirality, and their bandgaps are dependent on their diameter. Also, the properties of CNTs are very sensitive to their environment [131-134], making them an ideal choice for biosensors.

In this chapter, we first introduce the basics of DNA. Then, optical tweezers, an optical setup that can manipulate single molecules, are discussed. Finally, we present our work on a CNT biosensor for single DNA manipulation and decode the interaction between a CNT and a DNA at the single-molecule level by mechanical, electrical, and optoelectronic methods.

6.1 Introduction to DNA

6.1.1 Structure

DNA, or deoxyribonucleic acid, is a molecule that carries genetic information. Most DNA molecules consist of two strands, and they are called double-stranded DNA (dsDNA). Each strand is composed of nucleotides, which are essentially nitrogen-containing nucleobase with deoxyribose and a phosphate group. The primary nucleobase are cytosine (C), guanine (G), adenine (A), and thymine (T). The width of dsDNA is 2 nm, and the pitch between two base pairs is 0.34 nm. At room temperature, DNA molecule in solution is a coiled ball due to their flexible structure.

The best model so far to characterize the elastic behavior of a dsDNA is to treat it as a worm-like chain. A DNA molecule with length L and persistence length l_p, which is the length over which a polymer is roughly straight, is shown in Figure 6.1. $N = 1/l_p$ is the steps of the piece, or steps of a Random walk. The end-to-end distance of DNA is R_{RMS},

$$R_{RMS} = l_p \sqrt{2N\left[1 - \frac{1}{N}((1 - e^{-N})\right]}$$

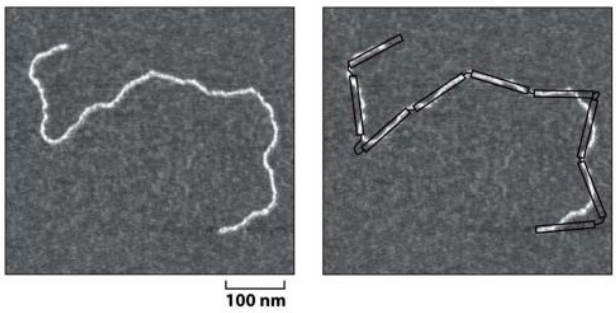

Figure 6.1 Worm-like chain model of DNA. Image reproduced from Ref. [135].

There are three common forms of dsDNA, B-Form, A-Form, and Z-Form. B-DNA is the dominant form, where two strands of DNA, each in a right-hand helix, wound around the same axis. A-DNA and Z-DNA also have helical structures, but they have significantly different geometry and dimensions. Figure 6.2 summarizes the different characteristics of these three DNA forms.

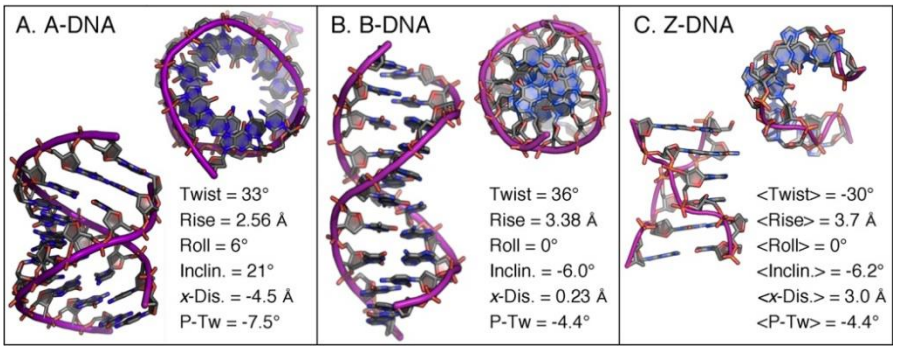

Figure 6.2 Different forms of DNA. Image reproduced from Ref. [136].

6.1.2 DNA overstretching

DNA response to mechanical force is the cornerstone to understanding DNA mechanics, which plays an important role in many genomic processes, such as DNA repair and replication.[137-139] Torsionally unconstrained dsDNA undergoes a structural transition under a tensile force of ~65 pN, where DNA can gain ~70% in contour length over a narrow force range.[140, 141] This process is called overstretching of DNA. Figure 6.3 shows the DNA overstretching process.

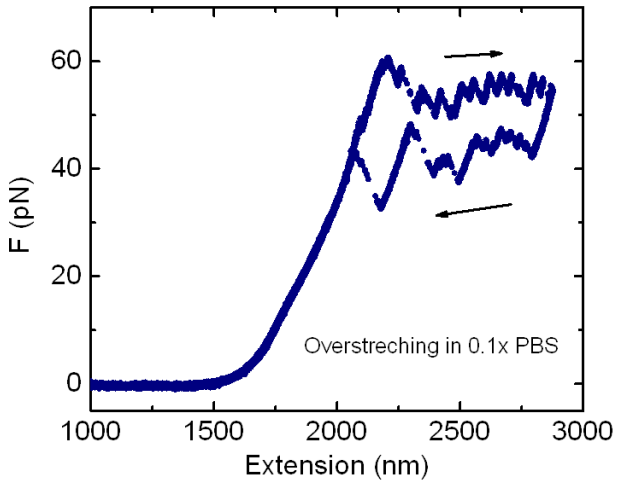

Figure 6.3 Overstretching a DNA molecule in 0.1x PBS.

Details of DNA overstretching are crucial to the understanding of DNA interaction with other molecules. Three mechanisms were proposed to explain the force change during overstretching: strand unpeeling, localized base-pair breaking, and formation of S-DNA.[142-145] It has been demonstrated that all these three structures can exist depending on DNA topology and local DNA stability.[146] As shown in Figure 6.4, when applying a force, a λ-DNA can either form melting bubbles (Figure 6.4a and its corresponding fluorescence image 6.4c) or peeled from a nick (Figure 7.4b and its corresponding fluorescence image 6.4d). Overstretching DNA can be a simple method to partially create single-stranded (ssDNA), which will be discussed later.

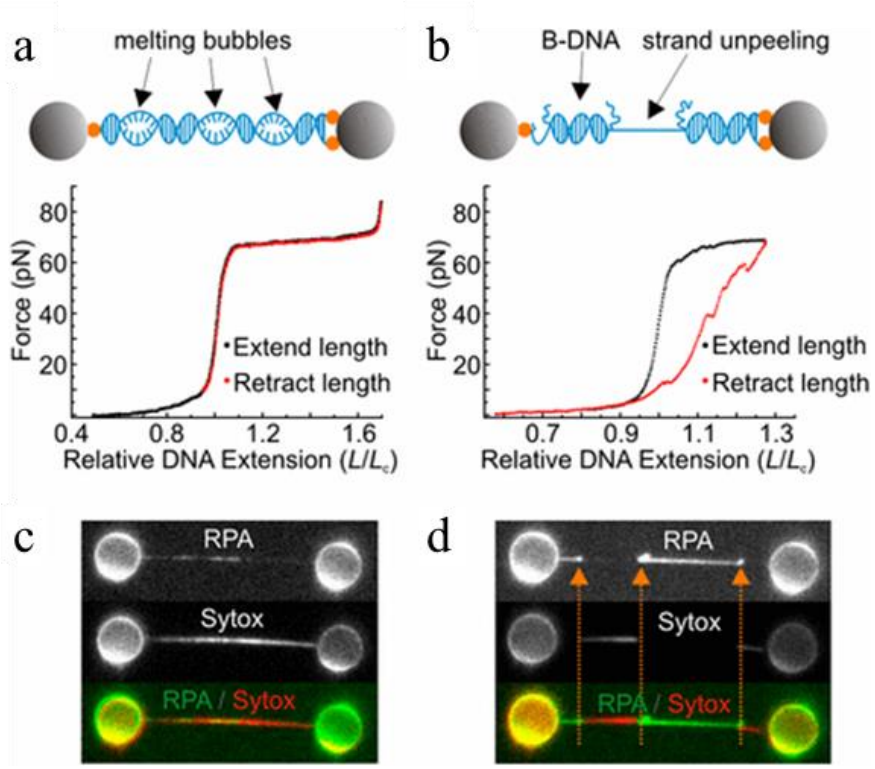

Figure 6.4 Different DNA overstretching mechanisms. a. Melting bubbles are formed due to overstretching, as confirmed by the fluorescence image in c. b. Nicks in DNA molecule backbone serve as nucleation site for strand unpeeling. Its corresponding fluorescence image is shown in d. Image reproduced from Ref. [146].

6.2 CNT transistors in electrolyte

6.2.1 Electrolyte solutions

Electrolyte is basically conductive solutions. In this dissertation, we are only concerned about aqueous electrolyte. When dissolved in water, salts such as NaCl crystals separates into Na^+ and Cl^- ions. These ions increase the conductivity of water, similar to the free electrons making metal conductive. The most important electrical property of electrolyte is its resistivity, ρ. For a variety of electrolytes, the equivalent conductivity, Λ, is established, where

$$\sigma = \Lambda \cdot c_0$$

where c_0 is the bulk salt concentration. For most salt, Λ has very similar values, $\Lambda \sim 100\times10^{-4}$ m^2 / $\Omega \cdot$ mol. [147] Therefore, we can estimate the resistivity using

$$\rho \sim \frac{100}{c_0\ [\mathrm{mM}]}\,\Omega \cdot m$$

Charged surface in solution will form an electrical field that attract oppositely charged ions in the solution to its surface, forming an electrical double layer. Several models have been proposed to characterize this double layer. In Helmholtz model, a single layer of counterions are absorbed to the charged surface and neutralize its charge, as shown in Figure 6.5a. The capacitance per area C_H for a typical cation radius of 2 Å is 3.5 F/m^2 in theory, although the experimental observation is an order of magnitude smaller.[148]

In Gouy-Chapman model, Poisson-Boltzmann equation is considered, and the potential near the charged surface is modeled as an exponentially fall rather than a sharp linear drop. In this model, the capacitance across the double layer at room temperature is[148]

$$C_{GC}\ [\mathrm{F/m^2}] = 2.3\sqrt{c_0[\mathrm{M}]}\ \cosh(19.5\ \Phi_0[\mathrm{V}])$$

However, this model ignores the finite size of ions. Other models of the electrical double layer include Stern model (Figure 6.5c) and Grahame model (Figure 6.5d), both of which combine Helmholtz model and Gouy-Chapman model and consider both the ion size and thermal energy. The understanding of electrical double layer is further improved by Bockris, who proposed a more detailed model taking the orientation of water molecule into consideration. This model returns the correct capacitance range of 0.1-0.4 F/m^2.[149]

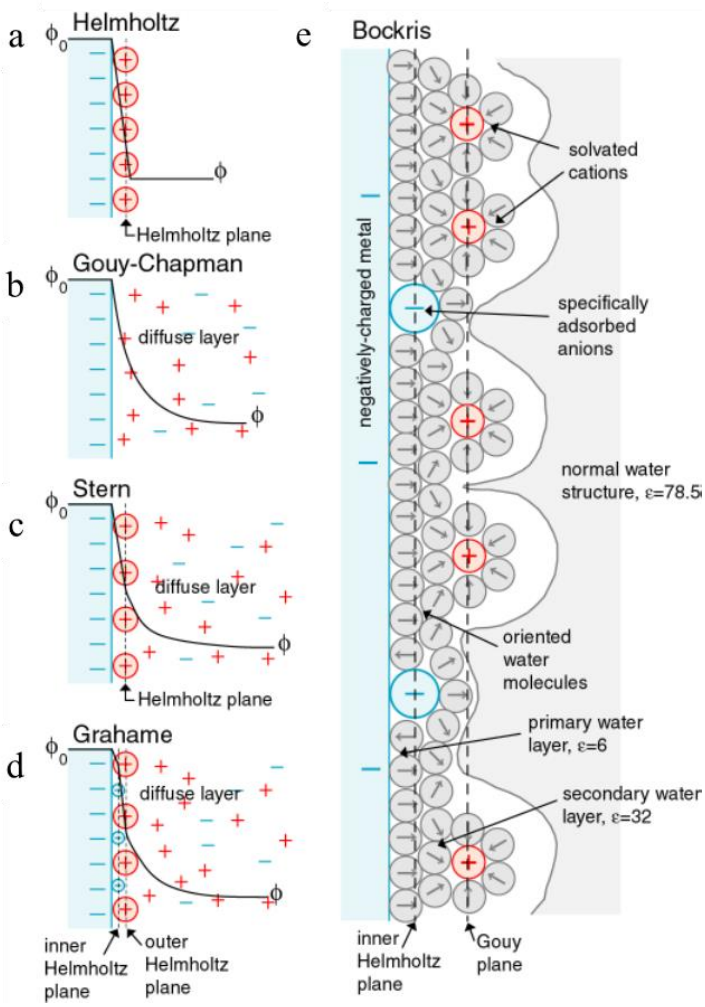

Figure 6.5 Models of electrical double layer. a. Helmholtz model. b. Gouy-Chapman model. c. Stern model. d. Grahame model. e. Bockris model. Image reproduced from Ref. [150].

The electrostatic potential near a small charged surface, such as a CNT, is an important parameter. From the Poisson-Boltzmann equation,

$$\nabla^2\phi(\vec{x}) = \frac{c_0 e}{\epsilon\epsilon_0}\left(e^{e\phi(\vec{x})/k_BT} - e^{-e\phi(\vec{x})/k_BT}\right) - \frac{\rho_{fixed}(\vec{x})}{\epsilon\epsilon_0}$$

we obtain

$$\nabla^2\phi(\vec{x}) = \frac{2c_0e^2}{\epsilon\epsilon_0 k_B T}\phi(\vec{x}) - \frac{\rho_{fixed(\vec{x})}}{\epsilon\epsilon_0}$$

We define Debye length λ_D as

$$\lambda_D = \sqrt{\frac{\epsilon\epsilon_0 k_B T}{2c_0e^2}}$$

In this Debye-Hückel model, potential will decay as e^{-r/λ_D}, and Debye length characterize the distance over which ions accumulate. At room temperature in water, the Debye length is approximated to

$$\lambda_D = \frac{0.3 \text{ nm}}{\sqrt{I \text{ [M]}}}$$

For example, in 0.1x PBS, the ion concentration is ~ 15 mM, and λ_D ~ 2.5 nm.

6.2.2 CNT transistors in electrolyte

When a CNT transistor is placed in electrolyte, an electrical double layer forms on its surface as discussed in the previous section. Due to the change of environment, the noise level of CNT transistor will also be different. Here, we focus on the charge noise of CNT transistors, which is a critical parameter to the bioelectronic interface characterization.

For an ultraclean suspended CNT transistors, Sharf *et. al.* performed electrical measurements at different gate voltages.[151] Figure 6.6a displays the device schematics and gate dependent electrical measurement. The CNT shows a p-type characteristic under gate bias. Figure 6.6b is the power spectral of the device. The charge noise is obviously larger in 5 mM phosphate buffer (PB, Figure 6.6c right) than in air (Figure 6.6c left).

The charge noise in the CNT transistor follows the Tersoff model, where environment noise is dominant in the subthreshold regime.[152] The liquid gate fluctuation δV results in the fluctuation in current $\delta I_{sd}(t)$

$$\delta I_{sd}(t) = \frac{dI_{sd}}{dV_{lg}} \delta V(t)$$

and the power spectrum is

$$S_I(f) = S_{input}(f) \left(\frac{dI_{sd}}{dV_{lg}} \right)^2$$

where $S_{input}(f)$ is the power spectral density of $\delta V(t)$. The power of the charge noise is inversely scaled with the CNT channel length, but barely influenced by the ionic concentration of the electrolyte solution.[153]

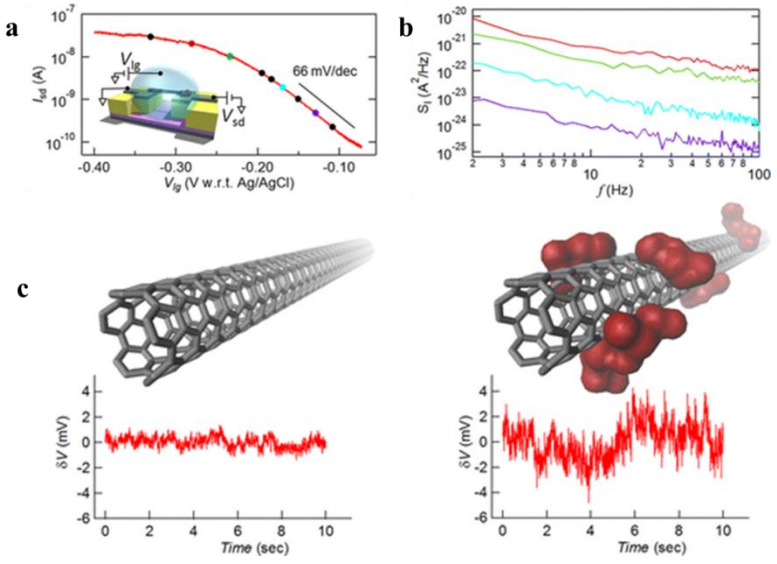

Figure 6.6 Charge noise of a CNT transistor. a. Schematic of a suspended CNT transistor and its gate-dependent electrical measurement. b. Power spectrum of the CNT transistor under different gate bias. c. Comparison of the current noise with (left) and without (right) the electrolyte environment. Image reproduced from Ref. [151] with permission from American Chemical Society.

Defects in CNTs significantly influence their electronic properties. By utilizing these defects, a CNT transistor can act as a single-molecule biosensor with ultrahigh sensitivity because a tethered molecule to these defects can directly affect the conducting channel of the device.[154] The defects in CNTs can be selectively created by point functionalization via electrochemical process.[155, 156] In this approach, atoms from carbon lattice are removed, resulting in reduced conductance. It is realized by etching the CNT in sulfuric acid with a reference voltage below the threshold voltage. When the conductance of CNT decreases with an abrupt jump, the applied voltage is removed. Then, a functional group is created at the defect site by exposing the CNT to potassium permanganate. Figure 6.7 shows the scanning gate microscopy image of CNT before and after functionalization.

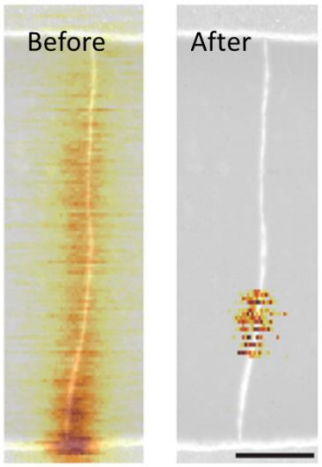

Figure 6.7 A CNT before and after functionalization. The scale bar is 500 nm. Image reproduced from Ref. [157] with permission from Nature Publishing Group.

Another way to functionalize CNT is to stack another molecule, such as pyrene, to the surface of CNT transistor through pi-pi stacking.[158, 159] The tight noncovalent bond formed by pyrene provides an electronic scattering site that can probe molecule activities.[154]

6.3 Optical tweezers

Optical Tweezers are devices that use light to manipulate microscopic objects. A focused laser creates radiation pressure from beam that can trap small particles. They can apply forces in the piconewton range and manipulate objects ranging in size from 10 nm to over 100 mm.

Figure 6.8 illustrates the basic operation principle of optical tweezers. When a laser beam is focused by a microscope objective to a diffraction-limited spot, this spot creates an optical trap which can hold a small object, such as a bead, in its center. The forces exerted on this bead consist of the light scattering and gradient forces. The gradient force pushes the bead to the center of the laser where the intensity is the highest due to the momentum imparted on the bead. Optical tweezers can measure displacements and forces with high precision and accuracy.

Typically, the size of the trapped bead is much smaller than the wavelength of the laser. The scattering force is[160]

$$F_{scatt} = \frac{I_0 \sigma n_m}{c}$$

$$\sigma = \frac{128\pi^2 a^6}{3\lambda^4}\left(\frac{m^2-1}{m^2+2}\right)^2$$

where I_0 is the laser intensity, σ is the scattering cross section of the bead, n_m is the index of refraction of the medium, and m is the ratio of the index of refraction of the particle to the medium. The gradient force is[160]

$$F_{grad} = \frac{2\pi\alpha}{cn_m^2}\nabla I_0$$

$$\alpha = n_m^2 a^3 \left(\frac{m^2 - 1}{m^2 + 2} \right)$$

For stable trapping, the axial gradient component must exceed the scattering component that pushing the bead away. Therefore, a steep light gradient is required.

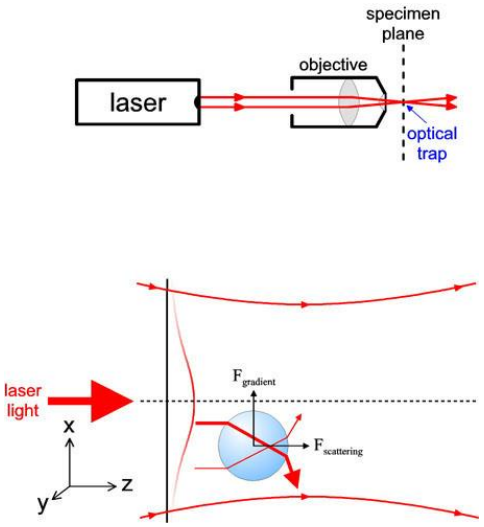

Figure 6.8 Operation principles of optical tweezers. Image reproduced from Ref. [161] with permission with from Springer Science+Business Media.

The position of the bead is detected by a position sensitive detector (PSD), which can record the position of the laser intensity in two dimensions.[162] Lateral displacements of a bead near the focus of a laser cause rotations in the laser propagation direction. These rotations occur in the image plane, which is the back aperture of the condenser and inaccessible in a microscope. Therefore, a lens is used to image a photodetector into a plane conjugate to the back-focal plane.[163] Axial position of the trapped bead can also be detected using an optical trap. Axial displacements will change the collimation of the laser, so the total amount of light collected by the photodetector changes.

The stiffness of the bead is determined by its Brownian motion. For a bead in harmonic potential with stiffness α,[160]

$$\frac{1}{2}k_BT = \frac{1}{2}\alpha\langle x^2\rangle$$

A straightforward way to obtain stiffness is to measure the frequency spectrum of the bead by PSD. The mass of the bead is very small, so its motion can be modeled by a massless, damped oscillator driven by Brownian motion,

$$\beta x(t) + \alpha\dot{x}(t) = F(t)$$

where β is the drag coefficient of the bead. We obtain the power spectrum,

$$|\tilde{x}(f)|^2 = \frac{k_BT}{\pi^2\beta\left[\left(\frac{\alpha}{2\pi\beta}\right)^2 + f^2\right]}$$

The corner frequency $f_c=\alpha/2\pi\beta$. Therefore the stiffness of the trap is given by $\alpha = 2\pi\beta f_c$. After the stiffness α is determined, we can obtain the force by Hooke's Law $F = -\alpha x$, where x is the displacement.

6.4 CNT and DNA interaction at single molecular level

The interface between carbon nanomaterials and DNA has been an intriguing complication with significant importance. Decoding their interactions helps to interpret the fundamental mechanisms in biomedical applications of carbon nanomaterials. For example, DNA is known to separate CNT bundles into individual CNTs due to the binding between DNA bases to the CNT sidewalls.[164-166] Quantifying the strength of their binding could assist the design of novel CNT sorting paradigm that leads to the precise production of chirality specific

CNTs. Another example is CNT-assisted drug delivery, which is demonstrated to be highly efficient and versatile.[167] One of the common media CNTs carrier for delivery is small interfering RNA, a RNA that can interfere with specific gene expression and thus treat disease.[130] By examining the binding strength of CNT surface and drug it carriers, we may be able to design new drug binding/releasing methods that further boost the efficiency of CNT-assisted drug delivery. Also, the binding between CNT and DNA exemplifies the binding between two individual π-electron interfaces, which is ubiquitous in nature. This binding interface can shed light on the development of other emerging materials that rely on the π stacking between layers, such as transition metal dichalcogenides (TMDCs). Investigating the CNT-DNA interface will potentially bridges the boundary between biological interfaces and nanotechnology. Here, we combine a suspended CNT transistor with dual-trap optical tweezers to investigate the π coupling interactions between an individual CNT and DNA.

6.4.1 The nature of CNT-DNA interactions

Numerous reports suggest DNA bind to the surface of CNT spontaneously.[165, 168-170] However, the behaviors of single-stranded DNA (ssDNA) and double-stranded DNA (dsDNA) are significantly different in terms of the binding strength. Heller et al. reported that poly-(dGdT) can wrap around individual CNTs,[171] but the hydrophilic backbone of dsDNA does not readily adsorb to the uncharged CNT surface in aqueous media.[170] For ssDNA, the hydrophobic part of ssDNA is attracted to the surface of CNT, both outside [165] and inside.[172, 173] Simulation results suggest that the free energy of ssDNA-CNT is minimized if additional DNA bases bind to CNT sidewalls.[168] Ming et al. also reported that this CNT-DNA binding force is strong enough to separate CNT bundles into individual CNTs.[165]

The binding strength between CNT and ssDNA also depend on other factors. For example, the interaction energy for different types of DNA bases, adenine (A), cytosine (C), guanine (G), and thymine (T), are different according to both molecular dynamics and ab initio simulations.[168, 169, 174, 175] In most of these studies, the binding strength is generally G>A>T>C, with binding energy values of around 10 kcal mol^{-1}. In addition, the chirality of CNT, or the relative angle that DNA bases bind to the CNT, may also influence the CNT-DNA binding strength.[176, 177]

6.4.2 Experimental configuration

We first fabricate transistors on a fused silica substrate. The detailed information is presented in Appendix I. Briefly, this is a three-layer device. In each device, there are thirty transistors with electrode pads of 44 μm in length. The drain electrodes of all the transistors are interconnected, whereas the source electrodes are individually separated. In each transistor, the distance between two electrodes are 7 μm, and a trench of 5 μm in width and 4 μm in depth lies between the electrodes so that the CNTs will be suspended after growth. We first define the electrodes of 5 nm Ti/40 n Pt, followed by deposition of 3 Å of Fe catalyst. Since this layer is extremely thin, the Fe atoms will not form a single uniform layer. Instead, islands of Fe atoms will scatter on the electrodes. Finally, the trench is etched by reactive ion etching (RIE). This dry-etching method maintains a good vertical trench profile. An optical image of the final device is shown in Figure 6.9a. After device fabrication, suspended CNTs were grown in the presence of 0.8 sccm CH_4, 0.2 sccm of H_2, and at 950 ^oC by chemical vapor depositon. Figure 6.9b displays an SEM image of a suspended CNT across the trench. We characterize the diameter of the CNTs. Figure 6.10a shows a typical atomic force microscopy image of the as-grown CNTs. Figure 6.10b shows the histogram of CNT diameters. The CNTs we grew have an average

diameter of 1.1 nm. However, the diameter of CNTs cannot be precisely controlled, neither can the chirality of the CNTs.

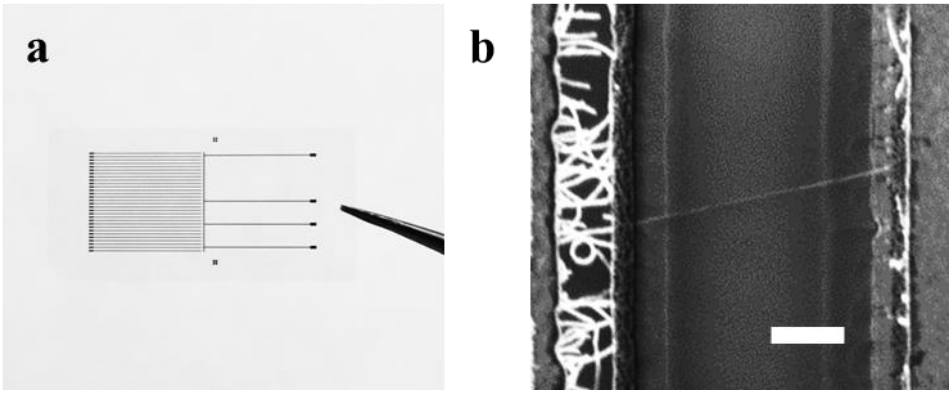

Figure 6.9 Suspended CNT transistor a. Optical image of the transistor. b. SEM image of a suspended CNT after synthesis. Scale bar: 2 μm.

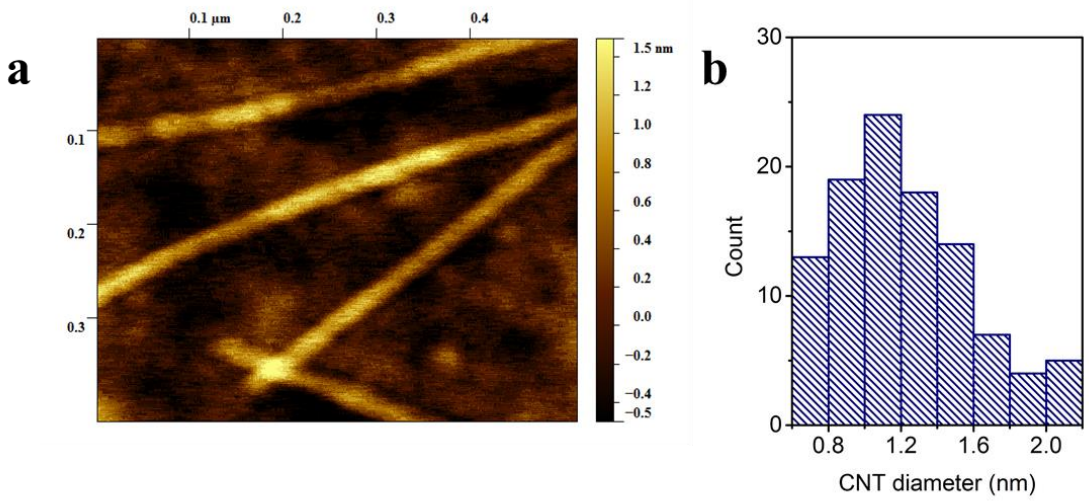

Figure 6.10 Diameter characterization of CNTs a. Atomic force microscopy image of CNTs. b. Histogram of CNT diameters.

The CNT transistor is sealed in a home-made microfluidic chamber after growth. The chamber has three channels, where the CNTs are in sealed in the middle channel while the top

and bottom channels contain beads linked with bio-active linkers. Scanning photocurrent microscopy was applied to identify the positions of the CNTs and confirm their electrical connection to the electrodes. Figure 6.11 presents the reflection image and corresponding photocurrent image of a typical suspended CNT in 1x PBS. Similar to its photocurrent response in air, a serial of positive and negative current dots scatter long the CNT, possibly due to defects.[46]

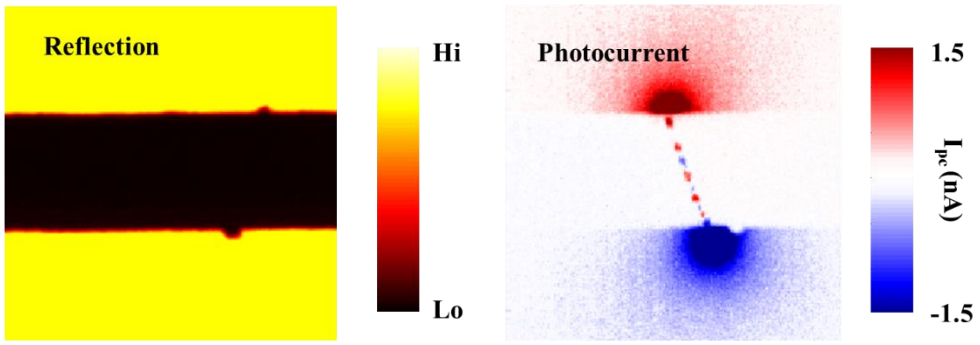

Figure 6.11 Scanning reflection and photocurrent image of a suspended CNT in PBS.

Figure 6.12 shows the experimental setup. The coordinate is defined as shown in the image. Here, we implement a dual-trap optical tweezers setup with 1064 nm laser. The displacement of the trapped beads can be detected by two PSDs. The dsDNA (pUC N9, ~7.5 k bps) is first end-labeled with biotin on one end and digoxigenin on the other end (see Appendix III for details). The bead in one optical trap is coated with streptavidin, and the other with anti-digoxigenin. Typical diameter of the beads is ~ 2 μm. Therefore, two beads and a single DNA molecule are linked by strong biotin- streptavidin or digoxigenin-anti-digoxigenin bonds.

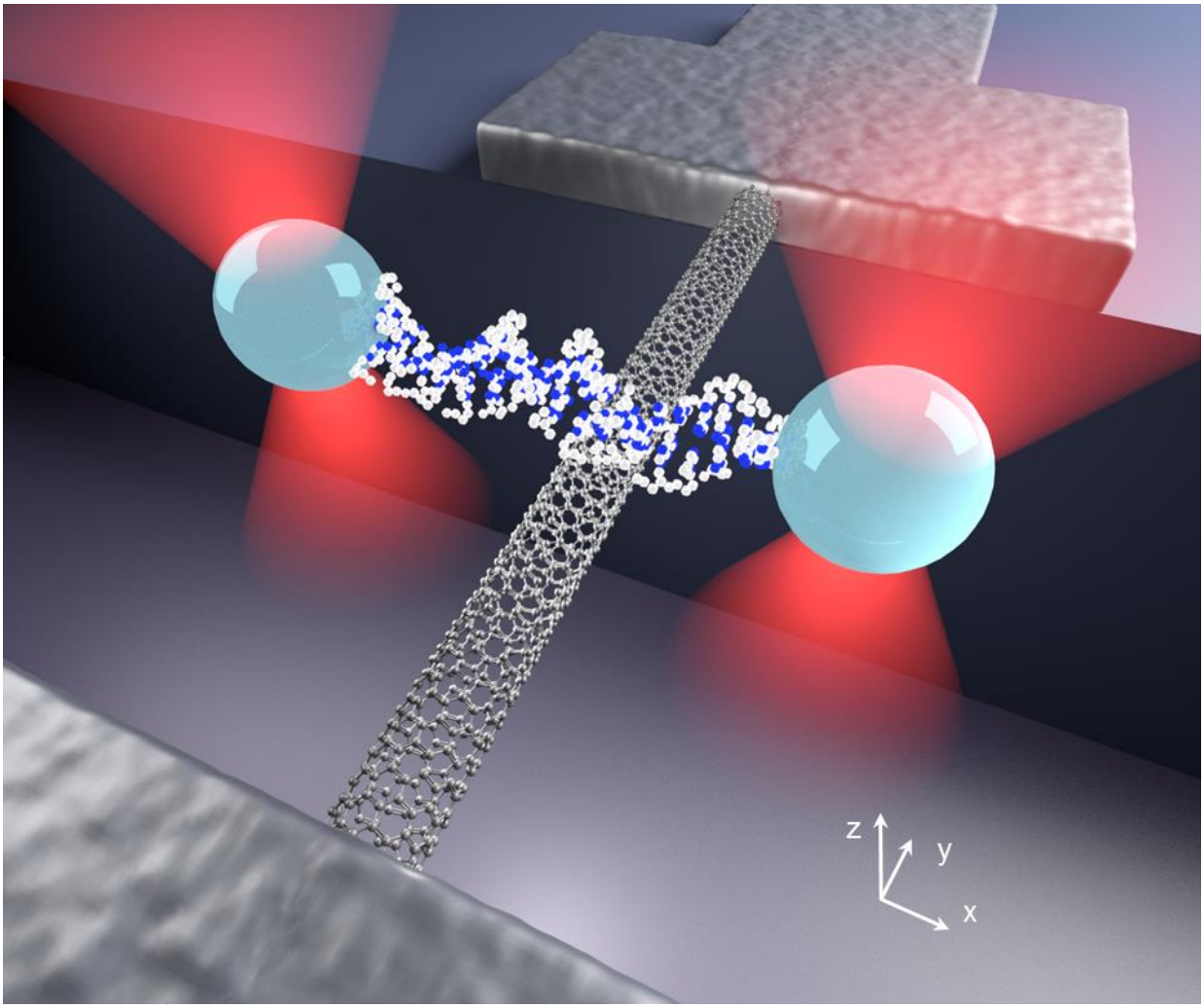

Figure 6.12 Experimental setup for CNT-DNA interaction. The coordinates are defined as marked in the bottom right corner.

6.4.3 CNT interaction with dsDNA

We first investigate the interaction between dsDNA and CNTs. A dsDNA molecule is linked to the two beads and we move the dsDNA on the top of the CNT. The DNA lies in the perpendicular direction of the CNT, and the CNT lies beneath the center part of the DNA. Therefore, the extra force generated on the beads are symmetric.

The elastic behavior of dsDNA requires us to put the dsDNA under tension during the whole experimental process. When pulling the dsDNA, the force remains relatively small until it increase as predicted by the worm-like chain model. This force goes up to around 65 pN and then remain relatively constant when even further stretching the dsDNA. At this point, the DNA goes through an overstretching phase.[140, 178, 179] In our experiment, we stretch the DNA to around 10 pN before push it down to bind to the CNT surface. At this force, the DNA shows elastic behavior.

We look into the force change in this process. We use two methods to obtain force. The first method is to use PSD as described in Section 6.3. However, the transmitted laser collected by PSD is not sensitive to the bead displacement in the axial direction, and thus cannot provide sufficient information on CNT-DNA binding force. Therefore, we used the second method, video image analysis (VIA), to subtract force information on CNT-DNA interaction in both lateral and axial directions. A well-established image processing algorithm was adapted to calculate the x, y, and z displacement of the beads, as shown in Figure 6.13.[180, 181] This method first use a band filter to reduce noise due to uneven illumination. Then, a convolution kernel was used to find the rough center position of the beads. Subsequently, the accurate positions of the beads are calculated, as well as the bead intensities. We also fixed a bead on the substrate and move it to a known distance by a piezo stage to obtain a bead image intensity-axial location calibration table. By comparing this table to the bead intensities obtained from the video images, the axial shift of the bead can be calculated. Compared with using PSD for bead location measurements, VIA not only provide more accurate information in the z direction, but also less influenced by the trench which can scatter transmitting laser beam. On the downside, VIA temporal resolution is limited to the video recording speed, which is typically much slower than

using PSDs. After bead displacement is determined, we can calculate the force in axial and lateral directions using stiffness values obtained from PSDs for each bead, respectively. The stiffness in the z direction was taken to be 1/5.9 of the stiffness in the lateral direction, as predicted by previous literature.[178, 182]

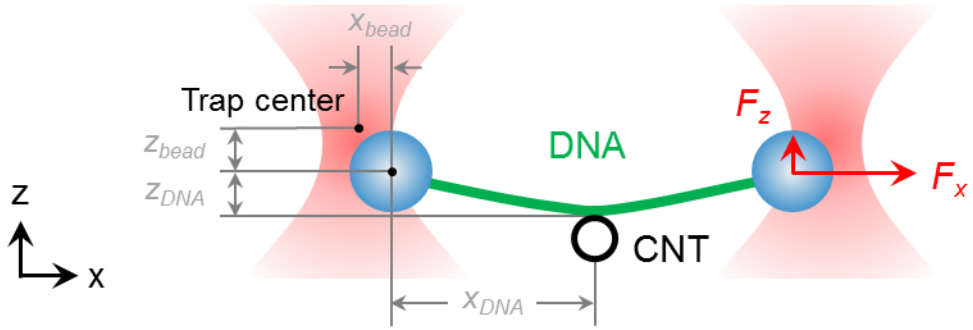

Figure 6.13 Illustration of bead displacement relative to the optical traps and definition of forces applied on the beads.

Using VIA, we explore the interactions between dsDNA and a CNT. Figure 6.14a is the stage z position, indicating the distance between optical trap centers and the electrodes (or the CNT since it is roughly on the same plane of electrodes). Figure 6.14b is a typical axial force change on the bead when push the dsDNA molecule down to attach the suspended CNT and then pull the DNA up. Initially, the dsDNA is pulled to around 10 pN. When moving the dsDNA down in the z direction, the force on the beads, or the two ends of dsDNA, remains generally a constant. At z ~ 0 μm, F started to increase, indicating the attachment of CNT and DNA. After DNA and CNT attached, if the beads were further pushed down, DNA would stretch in the lateral direction, and thus an increased force is detected.

After attachment, we start to pull the DNA up (at around 32 sec). The force recorded show a similar trend in the reverse direction. The axial force decrease to around zero, and remained constant. We did not observe any abrupt force change, which is consistent with previous literature that dsDNA and CNT binding force is very weak and is below our detection limit.

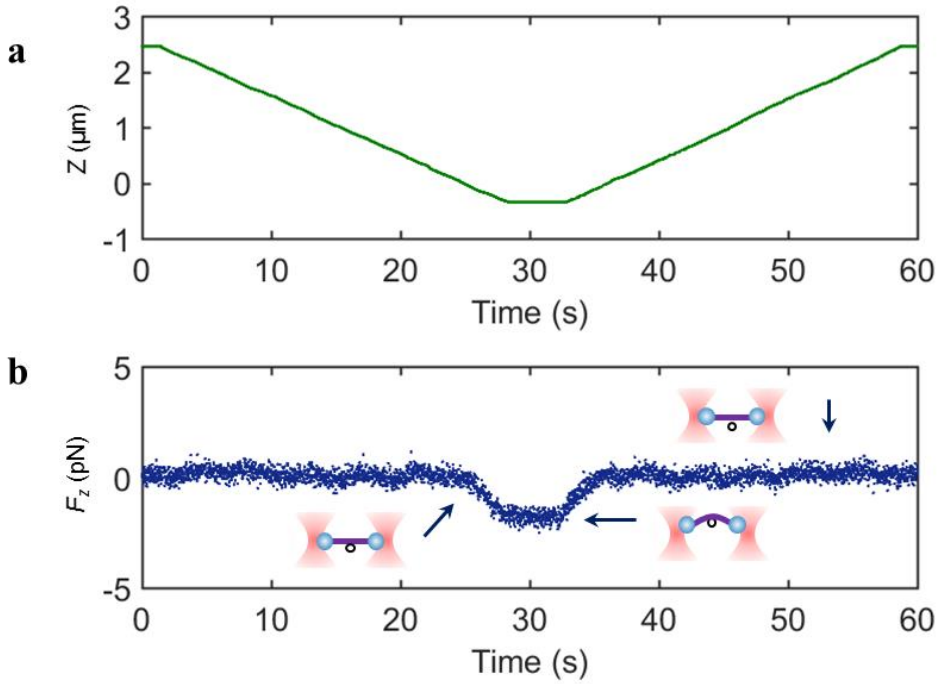

Figure 6.14 Interaction between dsDNA and CNT. a. Z position as a function of time, indicating the distance between optical trap centers and electrodes. b. Force in the z direction on the bead.

6.4.4 CNT interaction with ssDNA-dsDNA hybrid

We have experimentally confirmed that the binding strength between dsDNA and CNT is very weak. Next, we investigate the interactions between ssDNA and CNTs. Here, we used

ssDNA-dsDNA hybrid. This hybrid structure avoids the floppiness and secondary structure of ssDNA while maintains the rigidity of dsDNA.

We create ssDNA-dsDNA hybrid by overstretching a dsDNA molecule. As shown in Figure 6.15, a dsDNA molecule was first overstretched to around 65 pN (blue curve) and hold for several seconds. In some cases, when we relax this dsDNA, its elastic behavior changed (Figure 6.15 green curve). This change happened more frequently in low ion concentration solutions, and this change could be permanent. We attribute this elastic behavior change to the creation of ssDNA segments in the dsDNA. Presumably, if multiple nicks exist on the same strand of dsDNA, a segment of DNA may be peeled off starting from the nicks during overstretching. When the DNA was relaxed, the missing segment leads to partial ssDNA on the dsDNA, or the creation of an ssDNA-dsDNA hybrid.

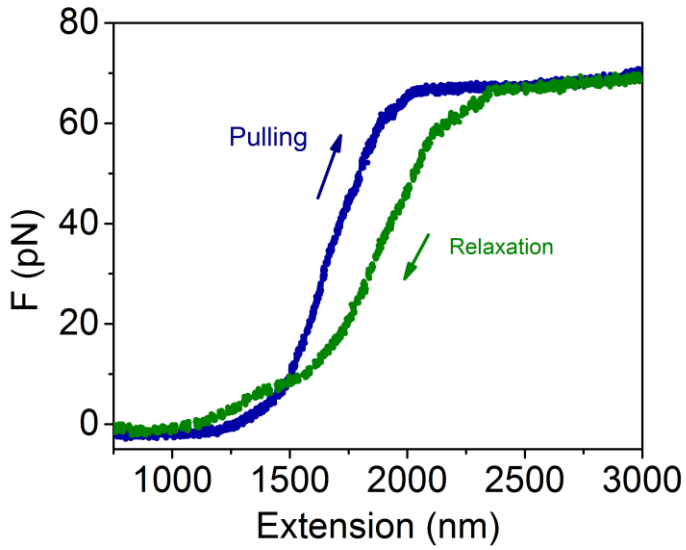

Figure 6.15 Overstretching dsDNA to obtain ssDNA-dsDNA hybrid. After overstretching, the DNA elastic behaviors changed.

After ssDNA-dsDNA hybrid was created, we repeat similar experiment as dsDNA-CNT interaction using this hybrid. As shown in Figure 6.16, the DNA was first pushed down toward the CNT. The green curve is the Z position obtain from the piezo stage, indicating the distance between the electrode plane (and the CNT) and the optical trap centers. The blue curve and red curve are the force change exerted on one bead calculated from VIA. Initially, both ΔF_X and ΔF_Z remained constant when we push the DNA down toward the CNT because CNT and DNA were not attached. At around 20 sec, both ΔF_X and ΔF_Z started to change, indicating the attachment of DNA and CNT. Subsequently, when we pulled up the DNA (indicated by the increase of ΔZ) both ΔF_X and ΔF_Z start to increase. Because of the binding between the ssDNA segment and the CNT, the DNA was still attached to the CNT after the optical trap centers were above the electrode. Therefore, we observed that ΔF_Z increased to above its initial value. Finally, the force underwent an abrupt drop, and both ΔF_X and ΔF_Z returned to their original values as before the DNA attached to the CNT. The force drop in the Z direction (both left and right beads combined) is the binding force between the CNT and ssDNA. When we create ssDNA-dsDNA hybrid by overstretching dsDNA, the location of this ssDNA segment on the dsDNA chain cannot be precisely controlled. Therefore, only in a small percentage of our experiments can we observe relative strong binding between ssDNA and CNTs.

We repeat this experiment of hybrid DNA-CNT interactions, and plot the histogram of their binding force. Figure 6.17 show the histogram of the binding force between ssDNA-dsDNA hybrids and CNTs. Interestingly, they were separated into three groups. The majority of the binding forces lies in the first group, or 1.3 ± 0.4 pN. The measured binding forces for the second

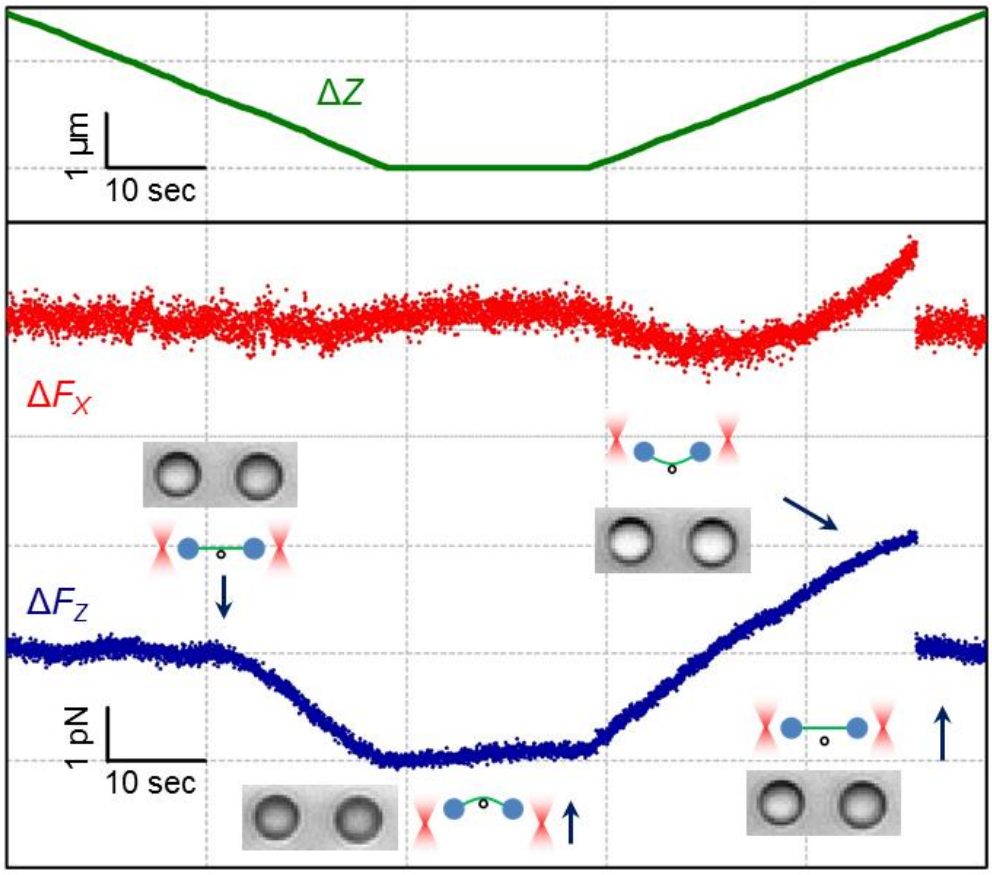

Figure 6.16 Interaction between ssDNA-dsDNA hybrid and CNT. The green curve in the top panel shows Z positions. The red curve in the bottom panel shows force in the x direction, and the blue curve shows force in the z direction. Both red and blue curves are forces changes on one bead. Optical images of the bead and illustrations are shown in the inset.

and third group are 3.2 ± 0.3 pN and 4.6 ± 0.1 pN, respectively. These three groups show a linear relationship in values. Considering the diameter of our CNTs (1.2 nm) and the distance between DNA bases (0.3-0.4 nm when stretched to 10 pN), we propose that the different force groups are the result of different number of DNA bases attached to CNT surfaces. Therefore, the binding force between a single DNA base and CNT sidewall is 1.3 ± 0.4 pN.

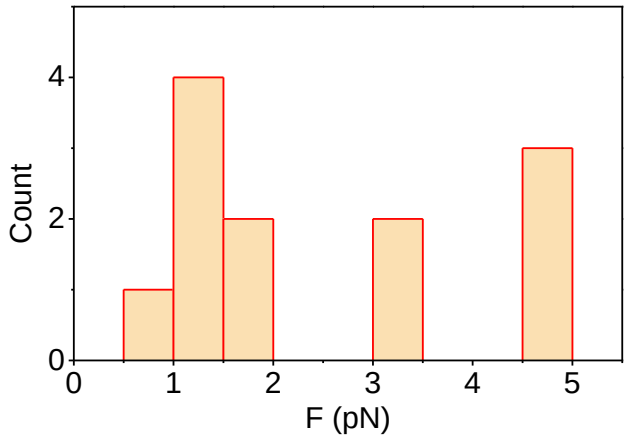

Figure 6.17 Histogram of the binding force between ssDNA-dsDNA hybrid and CNTs.

6.4.5 CNT morphology change

When DNA is attached to CNT, a force increase of a few piconewton is applied to not only the trapped beads, but the CNT as well. Therefore, the morphology of CNT will also change. We observe this change by 3D scanning photocurrent measurements. 3D scanning photocurrent measurement is realized by stacking a series of photocurrent images of different z positions together. The z position change is accomplished by controlled lens movement of the photocurrent setup. Here, we are more interested in the yz cut of the photocurrent images because they can show the CNT bending curves. Figure 6.18 displays the CNT photocurrent in yz plane with and without DNA attached. Initially, the CNT bends a little to the upward direction. After DNA attachment, the shape of the CNT shows a dramatic change, bending toward the inside of the trench. When we pull the DNA gradually upward, the shape of CNT alters in the other direction, indicating that DNA and CNT are still attached. Finally, the CNT shape no longer change with different DNA positions, suggesting they are detached during the movement.

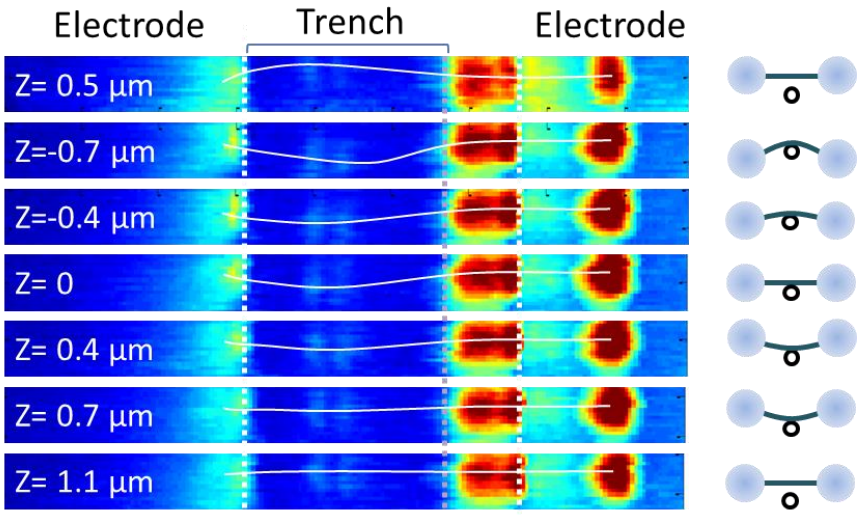

Figure 6.18 CNT photocurrent profile in yz plane. White solid line marks the shape of CNT.

The electrical signals I_{ds} of CNT transistors with DNA attached can be unstable. Figure 6.19 shows the current change ΔI_{ds} of a CNT transistor with a DNA molecule attached, where some scattered negative current spikes were observed. However, we only observe these current spikes in some CNT transistors with high "on" current. The underlying mechanisms of this process still requires further investigation.

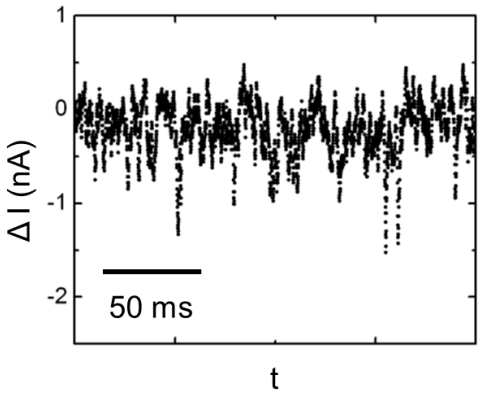

Figure 6.19 CNT current fluctuation with DNA attached. Some negative current spikes are observed.

Chapter 7 Summary and outlook

Compared to a few thousand years of development of traditional materials, low-dimensional materials only have a history of a few decades. Yet the basic physical and chemical properties of these materials have already been extensively investigated. The research focus has shifted from learning the fundamental properties of these low-dimensional materials to use them in real life. In this dissertation, we cover only a small portion of their fascinating properties, but these possessions of low-dimensional materials reflect some of their most exciting potential in future applications.

The optoelectronic properties of low-dimensional materials are quite unique. In the first chapter, we covered the physical and electronic band structure of low-dimensional materials, which are the cornerstone of their optoelectronic properties. Fluorescence and photocurrent microscopy are the key tools for their applications. Polarization-dependent photocurrent microscopy, for example, provides information on the relative contribution of different photocurrent generation mechanisms, an important factor to consider when designing photodetectors and photovoltaic devices. In addition, we discussed the applications of low-dimensional materials in the biological field, such as for image-guided drug delivery.

Low-dimensional materials are also potential candidates for bioelectronics. From graphene nanopores for DNA sequencing to MoS_2 label free biosensors,[183-185] they have proven to be efficient tools with high sensitivity. CNTs hold a special niche in biosensors. Because they are essentially a one-dimensional material, their small diameter (1-2 nm for single-walled CNTs) is comparable to many biomolecules, such as the diameter of DNA. This small size, along with their exceptional optical and electrical properties, allows for investigation of bio-

nano interface at single molecular level. Here, we explored the CNT-DNA interactions with the help of dual-trap optical tweezers. An increased DNA tension was observed when it is attached to the CNT, and the binding force between a single DNA base and CNT sidewall was measured. Meanwhile, the morphology of CNT significantly changes due to the DNA attachment.

Challenges still exist for CNT bioelectronics. Previous reports on dsDNA interaction with low-dimensional materials focus mostly on nanopores by electrical measurements. It is predicted that ssDNA will exhibit much stronger interactions with CNTs and graphene nanoribbons if no defect is introduced. The peeling force between CNT and ssDNA is reported to be 60-85 pN measured by atomic force microscopy.[186] Also, the electrical signals of a graphene nanoribbon can change significantly when ssDNA is attached.[187] However, we used ssDNA-dsDNA hybrid structures for our measurement, and it is difficult to control an ssDNA segment on the hybrid structure. One possible solution for future experiments is to synthesize ssDNA segments on a dsDNA chain instead of randomly creating ssDNA.

The future of low-dimensional materials is promising, yet they are still many steps away from real-life applications. With the development of synthesis techniques and improvement of their device structures, low-dimensional materials will hold on to be strong candidates for electronic and bioelectronic applications.

APPENDIX I Fabrication recipe for suspended CNT devices

This recipe is for use in Center for Nanophase Materials Sciences at Oak Ridge National Laboratory.

1. Layer 1 - Electrode

(1) Spin coat P20 (4k rpm, 45 sec). Wait for 20 sec before spinning (or until all the bubbles are gone).

(2) Spin coat LOR 1A (2k rpm, 45 sec).

(3) Bake the wafer at 180 ^{o}C for 20 min.

(4) Spin coat SPR955-0.7 (3k rpm, 45 sec).

(5) Soft-bake 90 ^{o}C for 90 sec.

(6) Expose the wafer in contact aligner. Exposure time 6 sec, and use Program 6.

(7) Post-bake 115 ^{o}C for 90 sec.

(8) Develop the wafer (MIF-CD-26 for 1 min and rinse with DI water). Check the patterns under microscope.

(9) Evaporate 5 nm Ti and 40 nm Pt. Evaporate speed between 0.5 and 2 Å/sec.

(10) Lift-off in acetone (sonicate for 1 min) followed by IPA (sonicate for 1 min).

(11) Lift-off in 1165 for 4 hours to remove the residue. Hot 1165 preferred.

(12) Check the patterns under microscope.

2. Layer 2 - Catalyst

(1) Spin coat P20 (4k rpm, 45 sec). Wait for 20 sec before spinning (or until all the bubbles are gone).

(2) Spin coat SPR955-0.7 (3k rpm, 45 sec).

(3) Soft-bake 90 ^{o}C for 90 sec.

(4) Expose the wafer in contact aligner. Exposure time 6 sec, and use Program 6.

(5) Post-bake 115 ^{o}C for 90 sec.

(6) Develop the wafer (MIF-CD-26 for 1 min and rinse with DI water). Check the patterns under microscope.

(7) Evaporate 10 nm Al_2O_3 and 3 Å Fe. Evaporate speed between 0.5 - 2 Å/sec for Al_2O_3 and 0.1 - 0.3 Å/sec for Fe. Use a higher power to heat up Fe for at least 5 min (Fe will show a red glow) before actual evaporation. A test run preferred.

(8) Lift-off in acetone (sonicate for 1 min) followed by IPA (sonicate for 1 min).

(9) Lift-off in 1165 for 4 hours to remove the residue. Hot 1165 preferred.

(10) Check the patterns under microscope.

3. Layer 3 - Trench

(1) Spin coat P20 (4k rpm, 45 sec). Wait for 20 sec before spinning (or until all the bubbles are gone).

(2) Spin coat SPR220-4.5 (2k rpm, 45 sec).

(3) Wipe out the photoresist on the edge of the wafer using acetone.

(4) Soft-bake 115 ^{o}C for 90 sec.

(5) Expose the wafer in contact aligner. Exposure time 14 sec, and use Program 6.

(6) Optional: wait for at least 30 min, and post-bake 115 ^{o}C for 90 sec.

(7) Develop the wafer (MIF-CD-26 for 1 min and DI water). Check the patterns under microscope.

(8) Check the photoresist thickness using P6 (should be ~5.5 um).

(9) Dice the wafer into small transistor pieces. Photoresist side up when dicing.

(10) Stick the small transistor pieces onto a carrier wafer using the thermal conductive oil provided.

(11) Clean the Oxford 100 metal etcher chamber using OPT chamber cleaning program for 10 min.

(12) Etch the wafer using program IVAN SiO_2 (50 sccm CHF_3, 2 sccm O_2, 2 sccm Ar) for 15 min.

(13) Clean the Oxford 100 chamber using ICP cleaning program for 30 min.

(14) Wipe the transistor backside with a wiper. Strip the photoresist using 1165 overnight.

(15) Check the patterns under microscope.

APPENDIX II Growth recipe of suspended CNT devices

1. Assemble the quartz tube. Slide the quartz boat to the middle of the furnace and mark the position of the boat.
2. Slide the quartz boat out. Put in a transistor and leave the boat in the quartz tube entirely outside the furnace.
3. Check the water bubbler is connected correctly and the bubbler valves are turned off.

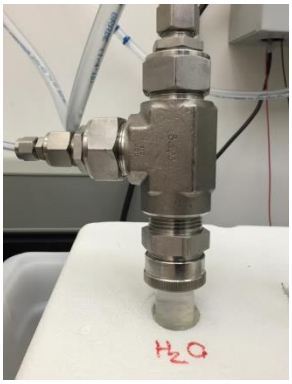

4. Turn Ar on. Ar = 0.8 SLM.
5. Connect the right end of the glass tube to the exhaust system.

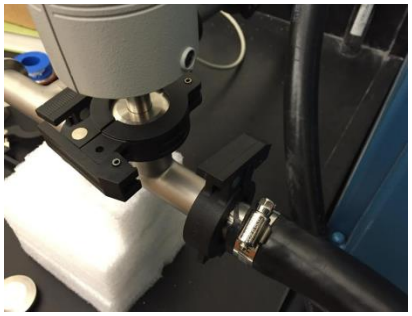

6. Turn on the furnace and set the temperature to 600 °C. Wait for ~10 min until the temperature is stable.

7. At 600 °C, turn on H_2O vapor (Ar through water bubbler) = 200 SCCM (catalyst oxidation). Leave Ar = 0.8 SLM on. Slide the boat to the marked position as quickly as possible (to avoid aggregation). Treat the sample for 10 min.
8. Turn off H_2O vapor and turn on H_2 = 200 SCCM (thermal annealing). Leave Ar = 0.8 SLM on. Treat the sample for 10 min.
9. Slide the boat outside the furnace.
10. Turn off H_2 and leave Ar = 0.8 SLM on.
11. Raise the furnace temperature, typically to 850-900 °C depending on catalyst condition. Wait for ~15 min until the temperature is stable.
12. Turn on CH_4 = 0.8 SLM, H_2 = 200 SCCM, and then turn off Ar = 0.8 SLM. Slide the boat to the marked position and leave it there for 20 min for CNT growth.
13. Slide the boat outside the furnace.
14. Turn on Ar = 0.8 SLM, turn off all other gases. Turn off the furnace and prop the lid open. Leave the sample in Ar for 5 min.
15. Disconnect the exhaust system. Turn off Ar. Take out the sample.

APPENDIX III Recipe for duplicating pUC-N9 DNA

1. Plasmid (pUC-N9) transformation to competent cell (DH5a).
2. Incubate Cell on LB plate (antibiotics: ampicillin), 37 °C, overnight.
3. Pick up a single colon from the LB-plate (antibiotics: ampicillin) an inoculate in liquid large scale LB media, 37 °C, overnight, shaking at 220 rmp.
4. Plasmid purification using QiaGen Maxi Plasmid purification kit.
5. Styl Digestion, overnight, 37 °C.
6. 1% Agarose Gel to test the cutting of DNA with controls.
7. Digoxigenin and Biotin labeling, 2 hr or overnight, 37 °C.
8. PCR purification using QiaGen Kit.

REFERENCES

1. Geim, A.K. and I.V. Grigorieva, *Van der Waals heterostructures.* Nature, 2013. **499**(7459): p. 419-425.
2. Novoselov, K.S., et al., *A roadmap for graphene.* Nature, 2012. **490**(7419): p. 192-200.
3. Meyer, J.C., et al., *The structure of suspended graphene sheets.* Nature, 2007. **446**(7131): p. 60-63.
4. Reich, S., C. Thomsen, and J. Maultzsch, *Carbon nanotubes: basic concepts and physical properties*2008: John Wiley & Sons.
5. Saito, R., G. Dresselhaus, and M.S. Dresselhaus, *Physical properties of carbon nanotubes*. Vol. 4. 1998: World Scientific.
6. Avouris, P., M. Freitag, and V. Perebeinos, *Carbon-nanotube photonics and optoelectronics.* Nature Photonics, 2008. **2**(6): p. 341-350.
7. Spataru, C.D., et al., *Theory and ab initio calculation of radiative lifetime of excitons in semiconducting carbon nanotubes.* Physical review letters, 2005. **95**(24): p. 247402.
8. Perebeinos, V., J. Tersoff, and P. Avouris, *Radiative lifetime of excitons in carbon nanotubes.* Nano Letters, 2005. **5**(12): p. 2495-2499.
9. Wallace, P.R., *The band theory of graphite.* Physical Review, 1947. **71**(9): p. 622.
10. Charlier, J.-C., et al., *Electron and phonon properties of graphene: their relationship with carbon nanotubes*, in *Carbon Nanotubes*2008, Springer. p. 673-709.
11. Zhang, Y., et al., *Experimental observation of the quantum Hall effect and Berry's phase in graphene.* Nature, 2005. **438**(7065): p. 201-204.
12. Du, X., et al., *Fractional quantum Hall effect and insulating phase of Dirac electrons in graphene.* Nature, 2009. **462**(7270): p. 192-195.
13. Novoselov, K., et al., *Two-dimensional atomic crystals.* Proceedings of the National Academy of Sciences of the United States of America, 2005. **102**(30): p. 10451-10453.
14. Bonaccorso, F., et al., *Graphene photonics and optoelectronics.* Nature Photonics, 2010. **4**(9): p. 611-622.
15. Reich, S., et al., *Tight-binding description of graphene.* Physical Review B, 2002. **66**(3): p. 035412.
16. Kim, K., et al., *A role for graphene in silicon-based semiconductor devices.* Nature, 2011. **479**(7373): p. 338-344.
17. Xu, M., et al., *Production of Extended Single-Layer Graphene.* Acs Nano, 2011. **5**(2): p. 1522-1528.
18. Li, X., et al., *Large-area synthesis of high-quality and uniform graphene films on copper foils.* Science, 2009. **324**(5932): p. 1312-1314.
19. Lee, J.-H., et al., *Wafer-scale growth of single-crystal monolayer graphene on reusable hydrogen-terminated germanium.* Science, 2014.
20. Fujita, D., *Nanoscale synthesis and characterization of graphene-based objects.* Science and Technology of Advanced Materials, 2011. **12**(4): p. 044611.
21. Hernandez, Y., et al., *High-yield production of graphene by liquid-phase exfoliation of graphite.* Nature Nanotechnology, 2008. **3**(9): p. 563-568.
22. Xu, M., et al., *Graphene-Like Two-Dimensional Materials.* Chemical Reviews, 2013. **113**(5): p. 3766-3798.

23. Wilson, J. and A. Yoffe, *The transition metal dichalcogenides discussion and interpretation of the observed optical, electrical and structural properties.* Advances in Physics, 1969. **18**(73): p. 193-335.
24. Hozoi, L., et al., *Ab Initio determination of Cu 3d orbital energies in layered copper oxides.* Scientific Reports, 2011. **1**.
25. Osada, M. and T. Sasaki, *Two-dimensional dielectric nanosheets: novel nanoelectronics from nanocrystal building blocks.* Advanced Materials, 2012. **24**(2): p. 210-228.
26. Golberg, D., et al., *Boron nitride nanotubes and nanosheets.* Acs Nano, 2010. **4**(6): p. 2979-2993.
27. Wang, Q.H., et al., *Electronics and optoelectronics of two-dimensional transition metal dichalcogenides.* Nature Nanotechnology, 2012. **7**(11): p. 699-712.
28. Benameur, M., et al., *Visibility of dichalcogenide nanolayers.* Nanotechnology, 2011. **22**(12): p. 125706.
29. Mak, K.F., et al., *Control of valley polarization in monolayer MoS2 by optical helicity.* Nature Nanotechnology, 2012. **7**(8): p. 494-498.
30. Zeng, H., et al., *Valley polarization in MoS2 monolayers by optical pumping.* Nature Nanotechnology, 2012. **7**(8): p. 490-493.
31. Cao, T., et al., *Valley-selective circular dichroism of monolayer molybdenum disulphide.* Nature communications, 2012. **3**: p. 887.
32. Li, L., et al., *Black phosphorus field-effect transistors.* Nature Nanotechnology, 2014. **9**: p. 372–377.
33. Liu, H., et al., *Phosphorene: An Unexplored 2D Semiconductor with a High Hole Mobility.* Acs Nano, 2014.
34. Reich, E.S., *Phosphorene excites materials scientists.* Nature, 2014. **506**(7486): p. 19-19.
35. Fiori, G., et al., *Electronics based on two-dimensional materials.* Nature Nanotechnology, 2014. **9**(10): p. 768-779.
36. Bolotin, K.I., et al., *Ultrahigh electron mobility in suspended graphene.* Solid State Communications, 2008. **146**(9-10): p. 351-355.
37. Liu, L.T., Y. Lu, and J. Guo, *On Monolayer MoS2 Field-Effect Transistors at the Scaling Limit.* Ieee Transactions on Electron Devices, 2013. **60**(12): p. 4133-4139.
38. Schwierz, F., *Graphene Transistors: Status, Prospects, and Problems.* Proceedings of the Ieee, 2013. **101**(7): p. 1567-1584.
39. Lai, R., et al. *Sub 50 nm InP HEMT device with fmax greater than 1 THz*. in *Electron Devices Meeting, 2007. IEDM 2007. IEEE International*. 2007. IEEE.
40. Wang, H., et al., *Integrated Circuits Based on Bilayer MoS2 Transistors.* Nano Letters, 2012. **12**(9): p. 4674-4680.
41. Freitag, M., et al., *Photoconductivity of single carbon nanotubes.* Nano Letters, 2003. **3**(8): p. 1067-1071.
42. Freitag, M., et al., *Imaging of the Schottky barriers and charge depletion in carbon nanotube transistors.* Nano Letters, 2007. **7**(7): p. 2037-2042.
43. Balasubramanian, K., et al., *Photoelectronic transport imaging of individual semiconducting carbon nanotubes.* Applied Physics Letters, 2004. **84**(13): p. 2400-2402.
44. Lee, J.U., *Photovoltaic effect in ideal carbon nanotube diodes.* Applied Physics Letters, 2005. **87**(7): p. 073101-073101-3.
45. Balasubramanian, K., et al., *Photocurrent imaging of charge transport barriers in carbon nanotube devices.* Nano Letters, 2005. **5**(3): p. 507-510.

46. Freitag, M., et al., *Scanning photovoltage microscopy of potential modulations in carbon nanotubes.* Applied Physics Letters, 2007. **91**(3): p. 031101.
47. Lee, E.J., et al., *Electronic Band Structure Mapping of Nanotube Transistors by Scanning Photocurrent Microscopy.* Small, 2007. **3**(12): p. 2038-2042.
48. Ahn, Y., et al., *Photocurrent imaging of pn junctions in ambipolar carbon nanotube transistors.* Nano Letters, 2007. **7**(11): p. 3320-3323.
49. Casiraghi, C., et al., *Rayleigh imaging of graphene and graphene layers.* Nano Letters, 2007. **7**(9): p. 2711-2717.
50. De Arco, L.G., et al., *Continuous, Highly Flexible, and Transparent Graphene Films by Chemical Vapor Deposition for Organic Photovoltaics.* Acs Nano, 2010. **4**(5): p. 2865-2873.
51. Yong, V. and J.M. Tour, *Theoretical Efficiency of Nanostructured Graphene-Based Photovoltaics.* Small, 2010. **6**(2): p. 313-318.
52. Xia, F.N., et al., *Photocurrent Imaging and Efficient Photon Detection in a Graphene Transistor.* Nano Letters, 2009. **9**(3): p. 1039-1044.
53. Park, J., Y.H. Ahn, and C. Ruiz-Vargas, *Imaging of Photocurrent Generation and Collection in Single-Layer Graphene.* Nano Letters, 2009. **9**(5): p. 1742-1746.
54. Wu, J.B., et al., *Organic Light-Emitting Diodes on Solution-Processed Graphene Transparent Electrodes.* Acs Nano, 2010. **4**(1): p. 43-48.
55. Matyba, P., et al., *Graphene and Mobile Ions: The Key to All-Plastic, Solution-Processed Light-Emitting Devices.* Acs Nano, 2010. **4**(2): p. 637-642.
56. Liu, M., X.B. Yin, and X. Zhang, *Double-Layer Graphene Optical Modulator.* Nano Letters, 2012. **12**(3): p. 1482-1485.
57. Lee, C.H., et al., *Atomically thin p-n junctions with van der Waals heterointerfaces.* Nature Nanotechnology, 2014. **9**(9): p. 676-681.
58. Mak, K.F. and J. Shan, *Photonics and optoelectronics of 2D semiconductor transition metal dichalcogenides.* Nature Photonics, 2016. **10**(4): p. 216-226.
59. Viculis, L.M., J.J. Mack, and R.B. Kaner, *A chemical route to carbon nanoscrolls.* Science, 2003. **299**(5611): p. 1361-1361.
60. Ortolani, L., et al., *Folded graphene membranes: mapping curvature at the nanoscale.* Nano Letters, 2012. **12**(10): p. 5207-5212.
61. Zang, J., et al., *Multifunctionality and control of the crumpling and unfolding of large-area graphene.* Nature Materials, 2013. **12**(4): p. 321-325.
62. Koskinen, P., *Electromechanics of twisted graphene nanoribbons.* Applied Physics Letters, 2011. **99**(1): p. 013105.
63. Sadrzadeh, A., M. Hua, and B.I. Yakobson, *Electronic properties of twisted armchair graphene nanoribbons.* Applied Physics Letters, 2011. **99**(1): p. 013102.
64. Bets, K.V. and B.I. Yakobson, *Spontaneous twist and intrinsic instabilities of pristine graphene nanoribbons.* Nano Research, 2009. **2**(2): p. 161-166.
65. Kit, O., et al., *Twisting graphene nanoribbons into carbon nanotubes.* Physical Review B, 2012. **85**(8): p. 085428.
66. Peterson, J.D., S. Vyazovkin, and C.A. Wight, *Kinetic Study of Stabilizing Effect of Oxygen on Thermal Degradation of Poly(methyl methacrylate).* The Journal of Physical Chemistry B, 1999. **103**(38): p. 8087-8092.
67. Jarrahi, Z., et al., *Enhanced Photoresponse in Curled Graphene Ribbons.* Nanoscale, 2013.

68. Freitag, M., et al., *Thermal infrared emission from biased graphene.* Nature Nanotechnology, 2010. **5**(7): p. 497-501.
69. Freitag, M., et al., *Energy Dissipation in Graphene Field-Effect Transistors.* Nano Letters, 2009. **9**(5): p. 1883-1888.
70. Connolly, M., et al., *Scanning gate microscopy of current-annealed single layer graphene.* Applied Physics Letters, 2010. **96**(11): p. 113501.
71. Berciaud, S., et al., *Electron and Optical Phonon Temperatures in Electrically Biased Graphene.* Physical review letters, 2010. **104**(22): p. 227401.
72. Engel, M., et al., *Light–matter interaction in a microcavity-controlled graphene transistor.* Nature communications, 2012. **3**: p. 906.
73. Nika, D.L., et al., *Phonon thermal conduction in graphene: Role of Umklapp and edge roughness scattering.* Physical Review B, 2009. **79**(15): p. 155413.
74. Chen, S., et al., *Raman Measurements of Thermal Transport in Suspended Monolayer Graphene of Variable Sizes in Vacuum and Gaseous Environments.* Acs Nano, 2010. **5**(1): p. 321-328.
75. Nguyen, K.T., et al., *Temperature and Gate Voltage Dependent Raman Spectra of Single-Layer Graphene.* Acs Nano, 2011. **5**(6): p. 5273-5279.
76. Hong, T., et al., *Thermal and optical properties of freestanding flat and stacked single-layer graphene in aqueous media.* Applied Physics Letters, 2014. **104**(22).
77. Van Zeghbroeck, B., *Principles of semiconductor devices*2004: Colorado University.
78. Beadle, W., *Quick reference manual for silicon integrated circuit technology*1985: John Wiley & Sons.
79. Liao, L., et al., *High-speed graphene transistors with a self-aligned nanowire gate.* Nature, 2010. **467**(7313): p. 305-308.
80. Wu, Y., et al., *High-frequency, scaled graphene transistors on diamond-like carbon.* Nature, 2011. **472**(7341): p. 74-78.
81. Liu, H., A.T. Neal, and P.D. Ye, *Channel length scaling of MoS2 MOSFETs.* Acs Nano, 2012. **6**(10): p. 8563-8569.
82. Fang, H., et al., *High-performance single layered WSe2 p-FETs with chemically doped contacts.* Nano Letters, 2012. **12**(7): p. 3788-3792.
83. Yoon, Y., K. Ganapathi, and S. Salahuddin, *How good can monolayer MoS2 transistors be?* Nano Letters, 2011. **11**(9): p. 3768-3773.
84. Koenig, S.P., et al., *Electric field effect in ultrathin black phosphorus.* Applied Physics Letters, 2014. **104**(10): p. 103106.
85. Hong, T., et al., *Polarized photocurrent response in black phosphorus field-effect transistors.* Nanoscale, 2014. **6**(15): p. 8978-8983.
86. Late, D.J., et al., *Hysteresis in single-layer MoS2 field effect transistors.* Acs Nano, 2012. **6**(6): p. 5635-5641.
87. Wang, H., et al., *Hysteresis of electronic transport in graphene transistors.* Acs Nano, 2010. **4**(12): p. 7221-7228.
88. Akahama, Y., S. Endo, and S. Narita, *Electrical-Properties of Black Phosphorus Single-Crystals.* Journal of the Physical Society of Japan, 1983. **52**(6): p. 2148-2155.
89. Cutler, M. and N. Mott, *Observation of Anderson localization in an electron gas.* Physical Review, 1969. **181**(3): p. 1336.
90. Zuev, Y.M., W. Chang, and P. Kim, *Thermoelectric and magnetothermoelectric transport measurements of graphene.* Physical review letters, 2009. **102**(9): p. 096807.

91. Buscema, M., et al., *Large and tunable photothermoelectric effect in single-layer MoS2.* Nano Letters, 2013. **13**(2): p. 358-363.
92. Das, S., et al., *High Performance Multilayer MoS2 Transistors with Scandium Contacts.* Nano Letters, 2013. **13**(1): p. 100-105.
93. Chamlagain, B., et al., *Mobility Improvement and Temperature Dependence in MoSe2 Field-Effect Transistors on Parylene-C Substrate.* Acs Nano, 2014. **8**(5): p. 5079-5088.
94. Cui, X., et al., *Multi-terminal transport measurements of MoS2 using a van der Waals heterostructure device platform.* Nature Nanotechnology, 2015. **10**(6): p. 534-540.
95. Hong, T., et al., *Plasmonic Hot Electron Induced Photocurrent Response at MoS2-Metal Junctions.* Acs Nano, 2015. **9**(5): p. 5357-5363.
96. Kim, M., et al., *Polarization dependence of photocurrent in a metal-graphene-metal device.* Applied Physics Letters, 2012. **101**(7).
97. Haigh, S.J., et al., *Cross-sectional imaging of individual layers and buried interfaces of graphene-based heterostructures and superlattices.* Nature Materials, 2012. **11**(9): p. 764-767.
98. Deng, Y.X., et al., *Black Phosphorus-Monolayer MoS2 van der Waals Heterojunction p-n Diode.* Acs Nano, 2014. **8**(8): p. 8292-8299.
99. Withers, F., et al., *Light-emitting diodes by band-structure engineering in van der Waals heterostructures.* Nature Materials, 2015. **14**(3): p. 301-306.
100. Buscema, M., et al., *Photocurrent generation with two-dimensional van der Waals semiconductors.* Chemical Society Reviews, 2015. **44**(11): p. 3691-3718.
101. Hong, T., et al., *Anisotropic photocurrent response at black phosphorus-MoS2 p-n heterojunctions.* Nanoscale, 2015. **7**(44): p. 18537-18541.
102. Takao, Y. and A. Morita, *Electronic-Structure of Black Phosphorus - Tight-Binding Approach.* Physica B & C, 1981. **105**(1-3): p. 93-98.
103. Engel, M., M. Steiner, and P. Avouris, *Black Phosphorus Photodetector for Multispectral, High-Resolution Imaging.* Nano Letters, 2014. **14**(11): p. 6414-6417.
104. Choi, W., et al., *High-Detectivity Multilayer MoS2 Phototransistors with Spectral Response from Ultraviolet to Infrared.* Advanced Materials, 2012. **24**(43): p. 5832-5836.
105. Wu, C.C., et al., *Elucidating the Photoresponse of Ultrathin MoS2 Field-Effect Transistors by Scanning Photocurrent Microscopy.* Journal of Physical Chemistry Letters, 2013. **4**(15): p. 2508-2513.
106. Buscema, M., et al., *Fast and Broadband Photoresponse of Few-Layer Black Phosphorus Field-Effect Transistors.* Nano Letters, 2014. **14**(6): p. 3347-3352.
107. Klee, V., et al., *Superlinear Composition-Dependent Photocurrent in CVD-Grown Monolayer MoS2(1-x)Se2x Alloy Devices.* Nano Letters, 2015. **15**(4): p. 2612-2619.
108. Jariwala, D., et al., *Emerging Device Applications for Semiconducting Two-Dimensional Transition Metal Dichalcogenides.* Acs Nano, 2014. **8**(2): p. 1102-1120.
109. Yuan, H.T., et al., *Polarization-sensitive broadband photodetector using a black phosphorus vertical p-n junction.* Nature Nanotechnology, 2015. **10**(8): p. 707-713.
110. Ferrari, M., *Cancer nanotechnology: opportunities and challenges.* Nature Review Cancer, 2005. **5**(3): p. 161-171.
111. Leuschner, C. and C.S.S.R. Kumar, *Nanoparticles for Cancer Drug Delivery*, in *Nanofabrication Towards Biomedical Applications*2005, Wiley-VCH Verlag GmbH & Co. KGaA. p. 289-326.

112. Pastorin, G., et al., *Functionalized carbon nanotubes: towards the delivery of therapeutic molecules.* Journal of Biomedical Nanotechnology, 2005. **1**(2): p. 133-142.
113. Chen, J., et al., *Functionalized single-walled carbon nanotubes as rationally designed vehicles for tumor-targeted drug delivery.* Journal of the American Chemical Society, 2008. **130**(49): p. 16778-16785.
114. Al Faraj, A., et al., *In vivo biodistribution and biological impact of injected carbon nanotubes using magnetic resonance techniques.* International journal of nanomedicine, 2011. **6**: p. 351.
115. Al Faraj, A., et al., *In vivo imaging of carbon nanotube biodistribution using magnetic resonance imaging.* Nano Letters, 2009. **9**(3): p. 1023-1027.
116. Miyawaki, J., et al., *In Vivo Magnetic Resonance Imaging of Single‐Walled Carbon Nanohorns by Labeling with Magnetite Nanoparticles.* Advanced Materials, 2006. **18**(8): p. 1010-1014.
117. Ju, S.-Y., W.P. Kopcha, and F. Papadimitrakopoulos, *Brightly fluorescent single-walled carbon nanotubes via an oxygen-excluding surfactant organization.* Science, 2009. **323**(5919): p. 1319-1323.
118. Reich, S., C. Thomsen, and P. Ordejon, *Electronic band structure of isolated and bundled carbon nanotubes.* Physical Review B, 2002. **65**(15): p. 155411.
119. Tan, P., et al., *Photoluminescence spectroscopy of carbon nanotube bundles: Evidence for exciton energy transfer.* Physical review letters, 2007. **99**(13): p. 137402.
120. Cognet, L., et al., *Stepwise quenching of exciton fluorescence in carbon nanotubes by single-molecule reactions.* Science, 2007. **316**(5830): p. 1465-1468.
121. Tucker-Schwartz, J.M., et al., *Dual-modality photothermal optical coherence tomography and magnetic-resonance imaging of carbon nanotubes.* Optics letters, 2012. **37**(5): p. 872-874.
122. O'connell, M.J., et al., *Band gap fluorescence from individual single-walled carbon nanotubes.* Science, 2002. **297**(5581): p. 593-596.
123. Moore, V.C., et al., *Individually suspended single-walled carbon nanotubes in various surfactants.* Nano Letters, 2003. **3**(10): p. 1379-1382.
124. Hong, T., et al., *Effect of Competitive Surface Functionalization on Dual-Modality Fluorescence and Magnetic Resonance Imaging of Single-Walled Carbon Nanotubes.* Journal of Physical Chemistry C, 2012. **116**(30): p. 16319-16324.
125. O'Connell, M.J., et al., *Reversible water-solubilization of single-walled carbon nanotubes by polymer wrapping.* Chemical Physics Letters, 2001. **342**(3): p. 265-271.
126. Liu, G. and R.W. Tsien, *Properties of synaptic transmission at single hippocampal synaptic boutons.* Nature, 1995. **375**(6530): p. 404-408.
127. Aubin, J., *Autofluorescence of viable cultured mammalian cells.* Journal of Histochemistry & Cytochemistry, 1979. **27**(1): p. 36-43.
128. Welsher, K., S.P. Sherlock, and H. Dai, *Deep-tissue anatomical imaging of mice using carbon nanotube fluorophores in the second near-infrared window.* Proceedings of the National Academy of Sciences, 2011. **108**(22): p. 8943-8948.
129. Cherukuri, P., et al., *Near-infrared fluorescence microscopy of single-walled carbon nanotubes in phagocytic cells.* Journal of the American Chemical Society, 2004. **126**(48): p. 15638-15639.

130. Qiao, J.B., et al., *Magneto-fluorescent carbon nanotube-mediated siRNA for gastrin-releasing peptide receptor silencing in neuroblastoma.* Rsc Advances, 2013. **3**(14): p. 4544-4551.
131. Modi, A., et al., *Miniaturized gas ionization sensors using carbon nanotubes.* Nature, 2003. **424**(6945): p. 171-174.
132. Kong, J., et al., *Nanotube molecular wires as chemical sensors.* Science, 2000. **287**(5453): p. 622-625.
133. Barone, P.W., et al., *Near-infrared optical sensors based on single-walled carbon nanotubes.* Nature Materials, 2005. **4**(1): p. 86-U16.
134. Zhao, Q., Z.H. Gan, and Q.K. Zhuang, *Electrochemical sensors based on carbon nanotubes.* Electroanalysis, 2002. **14**(23): p. 1609-1613.
135. Yildiz, A., *Principles of Molecular Biophysics Lecture Note*, in *PHYSICS 177, UC Berkeley*2013.
136. Ho, P.S. and M. Carter, *DNA Structure: Alphabet Soup for the Cellular Soul*, in *DNA Replication-Current Advances*, D.H. Seligmann, Editor 2011, InTech.
137. Dame, R.T., M.C. Noom, and G.J.L. Wuite, *Bacterial chromatin organization by H-NS protein unravelled using dual DNA manipulation.* Nature, 2006. **444**(7117): p. 387-390.
138. Abbondanzieri, E.A., et al., *Direct observation of base-pair stepping by RNA polymerase.* Nature, 2005. **438**(7067): p. 460-465.
139. Tanner, N.A., et al., *Single-molecule studies of fork dynamics in Escherichia coli DNA replication.* Nature Structural & Molecular Biology, 2008. **15**(2): p. 170-176.
140. Smith, S.B., Y.J. Cui, and C. Bustamante, *Overstretching B-DNA: The elastic response of individual double-stranded and single-stranded DNA molecules.* Science, 1996. **271**(5250): p. 795-799.
141. Cluzel, P., et al., *DNA: An extensible molecule.* Science, 1996. **271**(5250): p. 792-794.
142. Rouzina, I. and V.A. Bloomfield, *Force-induced melting of the DNA double helix - 1. Thermodynamic analysis.* Biophysical Journal, 2001. **80**(2): p. 882-893.
143. Shokri, L., et al., *DNA overstretching in the presence of glyoxal: Structural evidence of force-induced DNA melting.* Biophysical Journal, 2008. **95**(3): p. 1248-1255.
144. van Mameren, J., et al., *Unraveling the structure of DNA during overstretching by using multicolor, single-molecule fluorescence imaging*. Proceedings of the National Academy of Sciences of the United States of America, 2009. **106**(43): p. 18231-18236.
145. Paik, D.H. and T.T. Perkins, *Overstretching DNA at 65 pN Does Not Require Peeling from Free Ends or Nicks.* Journal of the American Chemical Society, 2011. **133**(10): p. 3219-3221.
146. King, G.A., et al., *Revealing the competition between peeled ssDNA, melting bubbles, and S-DNA during DNA overstretching using fluorescence microscopy.* Proceedings of the National Academy of Sciences of the United States of America, 2013. **110**(10): p. 3859-3864.
147. Haynes, W.M., *CRC handbook of chemistry and physics*2014: CRC press.
148. Bard, A.J., et al., *Electrochemical methods: fundamentals and applications*. Vol. 2. 1980: Wiley New York.
149. Bockris, J.M., M. Devanathan, and K. Muller. *On the structure of charged interfaces*. in *Proceedings of the Royal Society of London A: Mathematical, Physical and Engineering Sciences*. 1963. The Royal Society.

150. Ohshima, H. and K. Furusawa, *Electrical phenomena at interfaces: fundamentals: measurements, and applications*. Vol. 76. 1998: CRC Press.
151. Sharf, T., et al., *Origins of Charge Noise in Carbon Nanotube Field-Effect Transistor Biosensors.* Nano Letters, 2012. **12**(12): p. 6380-6384.
152. Tersoff, J., *Low-frequency noise in nanoscale ballistic transistors.* Nano Letters, 2007. **7**(1): p. 194-198.
153. Mannik, J., et al., *Charge noise in liquid-gated single-wall carbon nanotube transistors.* Nano Letters, 2008. **8**(2): p. 685-688.
154. Rosenstein, J.K., S.G. Lemay, and K.L. Shepard, *Single-molecule bioelectronics.* Wiley Interdisciplinary Reviews-Nanomedicine and Nanobiotechnology, 2015. **7**(4): p. 475-493.
155. Fan, Y.W., B.R. Goldsmith, and P.G. Collins, *Identifying and counting point defects in carbon nanotubes.* Nature Materials, 2005. **4**(12): p. 906-911.
156. Goldsmith, B.R., et al., *Conductance-controlled point functionalization of single-walled carbon nanotubes.* Science, 2007. **315**(5808): p. 77-81.
157. Sorgenfrei, S., et al., *Label-free single-molecule detection of DNA-hybridization kinetics with a carbon nanotube field-effect transistor.* Nature Nanotechnology, 2011. **6**(2): p. 125-131.
158. Choi, Y.K., et al., *Single-Molecule Lysozyme Dynamics Monitored by an Electronic Circuit.* Science, 2012. **335**(6066): p. 319-324.
159. Chen, R.J., et al., *Noncovalent sidewall functionalization of single-walled carbon nanotubes for protein immobilization.* Journal of the American Chemical Society, 2001. **123**(16): p. 3838-3839.
160. Neuman, K.C. and S.M. Block, *Optical trapping.* Review of Scientific Instruments, 2004. **75**(9): p. 2787-2809.
161. Ritort, F., *Single-molecule experiments in biophysics: Exploring the thermal behavior of nonequilibrium small systems.* Pramana-Journal of Physics, 2005. **64**(6): p. 1135-1147.
162. Shaevitz, J.W., et al., *Backtracking by single RNA polymerase molecules observed at near-base-pair resolution.* Nature, 2003. **426**(6967): p. 684-687.
163. Shaevitz, J.W., *A practical guide to optical trapping*, in *University of Washington*2006.
164. Tu, X.M., et al., *DNA sequence motifs for structure-specific recognition and separation of carbon nanotubes.* Nature, 2009. **460**(7252): p. 250-253.
165. Zheng, M., et al., *DNA-assisted dispersion and separation of carbon nanotubes.* Nature Materials, 2003. **2**(5): p. 338-342.
166. Zheng, M., et al., *Structure-based carbon nanotube sorting by sequence-dependent DNA assembly.* Science, 2003. **302**(5650): p. 1545-1548.
167. Bianco, A., K. Kostarelos, and M. Prato, *Applications of carbon nanotubes in drug delivery.* Current Opinion in Chemical Biology, 2005. **9**(6): p. 674-679.
168. Johnson, R.R., et al., *Free Energy Landscape of a DNA-Carbon Nanotube Hybrid Using Replica Exchange Molecular Dynamics.* Nano Letters, 2009. **9**(2): p. 537-541.
169. Johnson, R.R., A.T.C. Johnson, and M.L. Klein, *Probing the structure of DNA-carbon nanotube hybrids with molecular dynamics.* Nano Letters, 2008. **8**(1): p. 69-75.
170. Zhao, X. and J.K. Johnson, *Simulation of adsorption of DNA on carbon nanotubes.* Journal of the American Chemical Society, 2007. **129**(34): p. 10438-10445.
171. Heller, D.A., et al., *Optical detection of DNA conformational polymorphism on single-walled carbon nanotubes.* Science, 2006. **311**(5760): p. 508-511.

172. Gao, H.J., et al., *Spontaneous insertion of DNA oligonucleotides into carbon nanotubes.* Nano Letters, 2003. **3**(4): p. 471-473.
173. Okada, T., et al., *Electrically triggered insertion of single-stranded DNA into single-walled carbon nanotubes.* Chemical Physics Letters, 2006. **417**(4-6): p. 288-292.
174. Gowtham, S., et al., *Physisorption of nucleobases on graphene: Density-functional calculations.* Physical Review B, 2007. **76**(3).
175. Meng, S., et al., *DNA nucleoside interaction and identification with carbon nanotubes.* Nano Letters, 2007. **7**(1): p. 45-50.
176. Shankar, A., J. Mittal, and A. Jagota, *Binding between DNA and Carbon Nanotubes Strongly Depends upon Sequence and Chirality.* Langmuir, 2014. **30**(11): p. 3176-3183.
177. Ao, G.Y., C.Y. Khripin, and M. Zheng, *DNA-Controlled Partition of Carbon Nanotubes in Polymer Aqueous Two-Phase Systems.* Journal of the American Chemical Society, 2014. **136**(29): p. 10383-10392.
178. Wang, M.D., et al., *Stretching DNA with optical tweezers.* Biophysical Journal, 1997. **72**(3): p. 1335-1346.
179. Marko, J.F. and E.D. Siggia, *Stretching DNA.* Macromolecules, 1995. **28**(26): p. 8759-8770.
180. Xu, Y.Q., A. Barnard, and P.L. McEuen, *Bending and Twisting of Suspended Single-Walled Carbon Nanotubes in Solution.* Nano Letters, 2009. **9**(4): p. 1609-1614.
181. Crocker, J.C. and D.G. Grier, *Methods of digital video microscopy for colloidal studies.* Journal of Colloid and Interface Science, 1996. **179**(1): p. 298-310.
182. Visser, T.D. and S.H. Wiersma, *Diffraction of Converging Electromagnetic-Waves.* Journal of the Optical Society of America a-Optics Image Science and Vision, 1992. **9**(11): p. 2034-2047.
183. Sarkar, D., et al., *MoS2 Field-Effect Transistor for Next-Generation Label-Free Biosensors.* Acs Nano, 2014. **8**(4): p. 3992-4003.
184. Garaj, S., et al., *Graphene as a subnanometre trans-electrode membrane.* Nature, 2010. **467**(7312): p. 190-193.
185. Traversi, F., et al., *Detecting the translocation of DNA through a nanopore using graphene nanoribbons.* Nature Nanotechnology, 2013. **8**(12): p. 939-945.
186. Manohar, S., et al., *Peeling Single-Stranded DNA from Graphite Surface to Determine Oligonucleotide Binding Energy by Force Spectroscopy.* Nano Letters, 2008. **8**(12): p. 4365-4372.
187. Min, S.K., et al., *Fast DNA sequencing with a graphene-based nanochannel device.* Nature Nanotechnology, 2011. **6**(3): p. 162-165.